



Cite this: *Nanoscale*, 2017, **9**, 19337

Fortune teller fermions in two-dimensional materials†

Vladimir Damljanović,^{id}*^a Igor Popov^{id}^{a,b} and Radoš Gajić^c

Dirac-like electronic states are the main engines powering tremendous advancements in the research of graphene, topological insulators and other materials with these states. Zero effective mass, high carrier mobility and numerous applications are some consequences of linear dispersion that distinguishes Dirac states. Here we report a new class of linear electronic bands in two-dimensional materials with zero electron effective mass and sharp band edges, and predict stable materials with such electronic structures utilizing symmetry group analysis and an *ab initio* approach. We make a full classification of completely linear bands in two-dimensional materials and find that only two classes exist: Dirac fermions on the one hand and fortune teller-like states on the other hand. The new class supports zero effective mass similar to that of graphene and anisotropic electronic properties like that of phosphorene.

Received 18th October 2017,
Accepted 15th November 2017

DOI: 10.1039/c7nr07763g

rsc.li/nanoscale

1. Introduction

Electrons can move in certain materials as if they have no mass. Massless fermions in solid state materials have played an increasingly important role since the discovery of graphene,¹ a material where zero electron effective mass is caused by linear Dirac-like dispersion. While the first mapping of the electronic structure of graphene to the Dirac equation was an interesting theoretical curiosity,² the true significance of the Dirac-like states in solid state systems became apparent upon identification of many physical, measurable consequences of the linear dispersion.³ For instance, the existence of massless fermions in graphene yields extraordinarily high electron and hole mobilities⁴ with revolutionary implications in electronics. Other implications include, and are not limited to, Klein tunneling in single- and bi-layer graphene,⁵ and the quantum Hall⁶ and fractional quantum Hall⁷ effects at room temperature. The two-dimensional (2D) nature of graphene and related materials brings numerous additional advantages including mechanical flexibility, optical transparency,⁸ and possibilities for engineering heterostructures with the desired properties by stacking of two or more 2D materials.⁹

There is a whole plethora of various 2D materials beyond graphene with a linear dispersion in their band structure,¹⁰ including topological insulators¹¹ and semimetals.¹²

Although the behavior of electrons in the vicinity of *K* and *K'* points of graphene's 2D Brillouin zone (BZ) is actually described by the Weyl equation, such points are, for historical reasons, called 2D Dirac points (occasionally, 2D Weyl points).¹³ Their generalizations to 3D bulk single crystals are called (spin-1/2) Weyl points. According to the fermion doubling theorem, Weyl points (fermions) must appear in pairs of opposite chirality in the BZ. Two such Weyl fermions appearing at the same point in the BZ are called a 3D Dirac point,¹⁴ while a pair of 3D Dirac points at the same *k*-vector forms a double Dirac point.¹⁵ Note that at a band crossing, a Weyl point (3D Dirac point, double Dirac point) is two-fold (four-fold, eight-fold) degenerate. Generalizations for higher pseudo-spins are possible. Recent *ab initio* calculations show spin-1 Weyl and spin-3/2 Rarita-Schwinger-Weyl fermions in transition metal silicides,¹⁶ such as RhSi.¹⁷ An additional type of Dirac point appears in antiferromagnetic (AFM) 2D layers.^{18,19} Here the crossing point is four-fold degenerate, the corresponding Chern number of each band is zero and such crossings can appear as a single point in the BZ. Quasiparticles in solids can even go beyond their Weyl and Dirac counterparts as shown by the classification of linear and quadratic three-, six- and eight-band crossings in 3D crystals with a strong spin-orbit coupling (SOC).²⁰ Other studies also discuss three-,¹⁶ six-,^{16,17} and eight-fold¹⁵ degenerate fermions. Different types of electronic dispersions are intricately linked to symmetry, as also exemplified with cone engineering by symmetry manipulation,²¹ whereas new 2D Dirac cones have been generated in graphene under an external periodic potential.²² Mañes has used space group representations to find sufficient

^aInstitute of Physics Belgrade, University of Belgrade, Pregrevice 118, 11080 Belgrade, Serbia. E-mail: damlja@ipb.ac.rs; Fax: +381 11 3162 190; Tel: +381 11 3713 060

^bInstitute for Multidisciplinary Research, University of Belgrade, Kneza Višeslava 1, 11030 Belgrade, Serbia

^cGraphene Laboratory (GLAB) of Center for Solid State Physics and New Materials, Institute of Physics Belgrade, University of Belgrade, Pregrevice 118, 11080 Belgrade, Serbia

† Electronic supplementary information (ESI) available: Group-theoretical derivations, the effective mass and density of states calculation as well as the outline of the algorithm used in *ab initio* calculations. See DOI: 10.1039/C7NR07763G

conditions for the existence of spin-1/2 Weyl points in the BZ of 3D single crystals, and enumerated the possible T -symmetric corepresentations of such points for spinless systems (single groups).²³ Recently, a set of symmetry conditions that guarantees 2D Dirac-like dispersion in the vicinity of high symmetry points in the BZ of any non-magnetic 2D material with negligible SOC has been reported.^{24,25} Also, the existence of 2D Dirac fermions in bilayer non-honeycomb crystals using symmetry analysis has been indicated.²⁶ It has recently been shown that certain non-symmorphic symmetries induce new band hour-glass-like dispersion at the surface of some 3D single crystals.²⁷ Non-symmorphic symmetries also cause a similar dispersion in 2D (layer) systems with SOC.^{28,29} Topologically protected band touchings (TPBT) were found on the BZ surface of a SnTe 3D material class³⁰ and the A_2B_3 family of materials.³¹ Note that such band touchings^{27,30,31} are located away from the high-symmetry points of the BZ, and that they *can be moved but cannot be removed* by the change of model parameters used to calculate the band structure. Surprisingly, the existence of classes of massless fermions other than 2D Dirac-like, in 2D non-magnetic, time-reversal symmetric (TRS), materials with negligible SOC has not been addressed yet.

Here we report that combined TRS and certain crystal non-symmorphic symmetries of 2D materials lead to the emergence of peculiar massless linearly dispersive bands which we call fortune teller (FT) states. The geometries of these FT states in reciprocal space are pyramidal and paper fortune teller-like, unnoticed in solid state matter before. Our analysis indicates that these states and the Dirac cones are the unique possibilities for essential linear dispersive bands in all diperiodic directions of non-magnetic 2D materials without SOC. Our results are based on the analysis of all eighty layer single groups, which are all possible symmetries of non-magnetic 2D materials with negligible SOC. Inclusion of SOC would require an analysis of eighty layer double groups. These are distinct mathematical entities, and the results for the SOC-case do not apply to the non-SOC-case or *vice versa*. For this reason we treat here the non-SOC-case and leave analogous analysis for the SOC-case for future research. Similar search for Dirac-like and other (unconventional) quasiparticles has already been performed in the SOC-case.^{15,20,28,29} Finally, we predict stable 2D materials with our new massless fermions using DFT and our own-developed software. The *ab initio* calculations have confirmed the existence of the predicted electronic dispersion and quantitatively determined structural and electronic properties, which can be utilized in further experimental realizations of the new class of 2D materials.

2. Classification of linear states in 2D materials

We consider all possible symmetry groups of non-magnetic crystals with negligible SOC, which are periodic in two spatial directions and finite in the perpendicular direction. These are the so-called layer single groups (or diperiodic groups). This

implies that spinful degeneracy of a band is twice the spinless (orbital) degeneracy. Representation-protected band spinless degeneracy at the wave vector \mathbf{k}_0 in the 2D BZ, for bands belonging to the allowed³² (relevant,³³ small³⁴) irreducible representation (irrep) R of the group of the wave vector (little group) $G(\mathbf{k}_0)$, is given by the dimension of R . For all eighty layer single groups irreps R are either one- or two-dimensional.^{32,35} TRS either doubles spinless band-degeneracy at given \mathbf{k}_0 or leaves it unchanged.³⁶ Therefore, possible essential spinless band-degeneracies are one, two or four.

Since the orbitally (spinless) non-degenerate band is smooth, its second derivative is finite and the effective mass, being inversely proportional to the second derivative,³⁷ is nonzero. Therefore, the bands carrying zero effective mass are possible only in the vicinity of points in the BZ where the electron energy is orbitally (spinless) degenerate. We show in the ESI† that in the vicinity of a spinless double degenerate point, 2D Dirac bands are the only possible massless bands.

The behavior of the bands near four-fold orbitally (spinless) degenerate points in non-magnetic 2D materials with no SOC has not been examined thus far and we perform this task as described in the next section. Before that, we comment on why we think that four-fold spinless degeneracies can only be caused by combined TRS and crystal symmetry. It is well-known that some crystal non-symmorphic symmetries combined with certain topological properties can lead to touching of two bands somewhere on high symmetry lines in the BZ. We call this topologically protected band touchings (TPBT). In such TPBT, band degeneracy is larger than required by dimensionality of irreps of the corresponding little group. Such an approach started with Zak's introduction of elementary band representations³⁸ (EBR) and culminated with the recent classification of all possible 10 403 band structures in double space groups.³⁹ Essentially, the presence of TPBT can be established by investigation of compatibility relationships of irreps along certain closed loops in the BZ.⁴⁰ Alternative formulation is in terms of non-symmorphic symmetry eigenvalues.^{28,29} It sometimes happens that a band belongs to different irreps at two end points in the symmetry line and consequently must have touched another band an odd number of times (most probably once). The method cannot determine where exactly in the symmetry line two bands touch. Such a position depends on the model used to calculate the band structure. In layer single groups irreps of little groups for symmetry lines are one-dimensional inside BZ. BZ edges have either several one-dimensional irreps or only one two-dimensional irrep or two one-dimensional irreps related by TRS.³² Corresponding three-fold (four-fold *etc.*) spinless degeneracy would require TPBT of three (four *etc.*) bands *at the same point in the BZ* which we assume is unlikely. In addition, all these three (four *etc.*) bands would have to belong to different irreps of the little group, which at some point becomes impossible. On the other hand, two double-degenerate bands at the edge of the BZ belong to the same irrep and therefore cannot touch.⁴¹ For these reasons, we assume that TPBT can lead at most to double spinless degeneracy and to Dirac-like dispersion. The

same assumption holds even for band touchings that are not protected by topology but are model-dependent (accidental band touchings). Note that above arguments do not apply to the SOC case. For example, TPBT of two two-fold spinful degenerate bands exist in some layer double groups.²⁸

3. Fortune teller states

In the following, the functional form of the new linear dispersion relation that corresponds to the vicinity of four-fold spinless degeneracy will be presented and compared to 2D Dirac-like dispersion. As before, we assume that \mathbf{q} is a wave vector of small modulus, \mathbf{t} a real 2D vector, u_1, u_2 positive quantities and q_1, q_2 projections of \mathbf{q} along certain, mutually orthogonal directions. If \mathbf{k}_0 is a point that hosts a pair of 2D Dirac cones, then the Taylor expansion of the electron energy around this point reads:

$$E_{1,2}(\mathbf{k}_0 + \mathbf{q}) \approx E_0 + \mathbf{t} \cdot \mathbf{q} \pm \sqrt{u_1 q_1^2 + u_2 q_2^2}. \quad (1)$$

For $u_1 = u_2$, 2D Dirac cones are isotropic and for $\mathbf{t} \neq 0$, the cones are tilted.^{42,43} The new electronic dispersion presented in this paper is:

$$E_{1,2,3,4}(\mathbf{k}_0 + \mathbf{q}) \approx E_0 \pm |u_1 q_1| \pm |u_2 q_2|. \quad (2)$$

While the 2D Dirac band has the geometric form of a simple cone with a circular or elliptical cross section, the geometry of dispersion (2) consists of two different geometric forms. The plus sign under the absolute value yields the geometry of a four-sided pyramid, whereas the minus sign corresponds to a more complex geometry, which looks like the paper origami called paper fortune tellers [Fig. 2(b)]. Since both forms always appear together, we label dispersion (2) using one name – the fortune teller (FT) dispersion.

Next, we state the conditions that lead to four-fold essential spinless degeneracy. According to Herring,³⁶ there are, in principle, two possibilities for achieving this. The first one is:

- O₁: \mathbf{k}_0 is equivalent to its inverse $-\mathbf{k}_0$,
- O₂: R is two-dimensional,
- O₃: R is pseudo-real or complex.

The second one is: \mathbf{k}_0 is not equivalent to $-\mathbf{k}_0$, $-\mathbf{k}_0$ is in the star of \mathbf{k}_0 , R is two-dimensional, $R_{\text{in}} = R \uparrow G$ is pseudo-real or complex (R_{in} is the representation of the whole layer single

conditions O₁–O₃ are the only essential four-fold spinless degeneracies in such systems.

Now we show how the linear dispersion (2) is connected to TRS and crystal symmetry. A general matrix form of the Taylor expansion of a four-component Hamiltonian around a given \mathbf{k}_0 point of BZ is:

$$\hat{H}(\mathbf{k}_0 + \mathbf{q}) \approx E_0 \hat{I}_4 + \hat{H}', \quad (3)$$

where

$$\hat{H}' = \hat{W}(\hat{I}_4 \otimes |\vec{q}\rangle), \quad (4)$$

and

$$\hat{W} = \left[\left\langle \frac{\partial}{\partial \mathbf{q}} \right| \hat{H}(\mathbf{k}_0 + \mathbf{q}) \right]_{\mathbf{q}=0}. \quad (5)$$

\hat{I}_4 is a four-dimensional unit matrix, \otimes denotes the Kronecker product, $\langle \partial / \partial \mathbf{q} |$ is the transposed gradient at $\mathbf{q} = 0$, hence \hat{W} is a four-by-eight matrix. We can combine the representation R and its complex conjugate R^* to obtain one four-dimensional, physically irreducible, real representation D in the following way: $D = R \oplus R^*$. It follows that we can choose the basis functions $\{\varphi_1, \dots, \varphi_4\}$ for D to be real at \mathbf{k}_0 so that TRS imposes the following ($*$ denotes complex conjugation):²³

$$\hat{H}'^*(\mathbf{k}_0 + \mathbf{q}) = \hat{H}'(\mathbf{k}_0 - \mathbf{q}). \quad (6)$$

Taking the first order derivative of this equation with respect to \mathbf{q} , at $\mathbf{q} = 0$ gives the following condition for \hat{W} :

$$\hat{W}^* = -\hat{W}. \quad (7)$$

Taking into account in addition the hermicity of the Hamiltonian, we obtain for \hat{H}' the following:

$$\hat{H}' = i \begin{pmatrix} 0 & \mathbf{v}_1 \cdot \mathbf{q} & \mathbf{v}_2 \cdot \mathbf{q} & \mathbf{v}_3 \cdot \mathbf{q} \\ -\mathbf{v}_1 \cdot \mathbf{q} & 0 & \mathbf{v}_4 \cdot \mathbf{q} & \mathbf{v}_5 \cdot \mathbf{q} \\ -\mathbf{v}_2 \cdot \mathbf{q} & -\mathbf{v}_4 \cdot \mathbf{q} & 0 & \mathbf{v}_6 \cdot \mathbf{q} \\ -\mathbf{v}_3 \cdot \mathbf{q} & -\mathbf{v}_5 \cdot \mathbf{q} & -\mathbf{v}_6 \cdot \mathbf{q} & 0 \end{pmatrix}, \quad (8)$$

where \mathbf{v}_j are real 2D vectors. Since \hat{H}' is purely imaginary, for every eigenstate ψ_n corresponding to energy E_j , there exists an eigenstate ψ_n^* that corresponds to the energy $-E_j$. Therefore, eigenvalues of \hat{H}' come in pairs $(E_j, -E_j)$ and the Hamiltonian \hat{H}' obeys the particle-hole symmetry. The eigenvalues of $\hat{H}'(\mathbf{k}_0) + \hat{H}'$ given by eqn (9) confirm our statement:

$$E_{1,2,3,4} = E_0 \pm \frac{1}{\sqrt{2}} \sqrt{\sum_{j=1}^6 (\mathbf{v}_j \cdot \mathbf{q})^2} \pm \sqrt{\left[\sum_{j=1}^6 (\mathbf{v}_j \cdot \mathbf{q})^2 \right]^2 - 4[(\mathbf{v}_1 \cdot \mathbf{q})(\mathbf{v}_6 \cdot \mathbf{q}) - (\mathbf{v}_2 \cdot \mathbf{q})(\mathbf{v}_5 \cdot \mathbf{q}) + (\mathbf{v}_3 \cdot \mathbf{q})(\mathbf{v}_4 \cdot \mathbf{q})]^2}. \quad (9)$$

group G , obtained by induction from R). Detailed case-by-case study of representations of layer single groups³² shows, by exhaustion, that the second possibility never occurs in 2D non-magnetic materials with negligible SOC. A more detailed discussion on the conditions for four-fold spinless degeneracy and the classification of all massless bands in non-magnetic 2D materials with weak SOC is given in the ESI.† Therefore

Note that particle-hole symmetry is not accidental, but it is a consequence of the fact that complex conjugation is a symmetry operation. More precisely, in our case the combination of TRS, reality of representation D and the fact that \mathbf{k}_0 is time-reversal invariant momentum leads to purely imaginary \hat{H}' , and to particle-hole symmetry with respect to E_0 .

To further simplify eqn (9) we use the following identity²³ valid for every element (in Seitz notation) $(\hat{h}|\tau_{\hat{h}} + \mathbf{R})$ of the little group $G(\mathbf{k}_0)$:

$$\hat{H}(\mathbf{k}_0 + \mathbf{q}) = \hat{D}^+((\hat{h}|\tau_{\hat{h}} + \mathbf{R}))\hat{H}(\mathbf{k}_0 + \hat{h}'\mathbf{q})\hat{D}((\hat{h}|\tau_{\hat{h}} + \mathbf{R})), \quad (10)$$

where $\hat{D}((\hat{h}|\tau_{\hat{h}} + \mathbf{R}))$ is the matrix of the representation D that corresponds to the element $(\hat{h}|\tau_{\hat{h}} + \mathbf{R})$ and \hat{h}' is the reduction (as an operator) of \hat{h} to two-dimensional \mathbf{k} -space. After differentiating (10) with respect to \mathbf{q} , at $\mathbf{q} = 0$ we obtain (T denotes transposition):

$$\hat{W} = \hat{D}((\hat{h}|\tau_{\hat{h}} + \mathbf{R}))\hat{W}[\hat{D}((\hat{h}|\tau_{\hat{h}} + \mathbf{R})) \otimes \hat{h}'^T]. \quad (11)$$

Eqn (11) is a consequence of crystal symmetry. If we write the matrix \hat{W} as a column-vector $|\hat{W}\rangle$, eqn (11) becomes:

$$[\hat{D}((\hat{h}|\tau_{\hat{h}} + \mathbf{R})) \otimes \hat{D}((\hat{h}|\tau_{\hat{h}} + \mathbf{R})) \otimes \hat{h}']|\hat{W}\rangle = |\hat{W}\rangle. \quad (12)$$

It follows that the matrix \hat{W} belongs to the totally symmetric part of the representation $D \otimes D \otimes \Gamma_{2\text{DPV}}$, where $\Gamma_{2\text{DPV}}$ is a two-dimensional polar-vector representation. For all groups that satisfy conditions O₁–O₃ we have, using Wigner's method of group projectors, found the form that symmetry imposes on the matrix \hat{W} and consequently on vectors \mathbf{v}_j , and inserted the result in eqn (9). In all cases, the equation for eigenvalues (9) reduces to the dispersion (2). More details on the application of group projectors are given in the ESI†

It turns out that only three out of eighty layer single groups have allowed representations satisfying the conditions O₁–O₃. Groups allowing the dispersion (2) are listed in Table 1. All three groups are non-symmorphic and belong to the rectangular system. The component q_1 can be chosen as projection of \mathbf{q} along a direction that is parallel to any screw axis 2_1 , q_2 is a projection along the perpendicular direction. The points \mathbf{k}_0 hosting the dispersion (2) are located at the corners $(\pm\pi/a, \pm\pi/b)$ of the rectangle that presents the BZ border. The corresponding space group from Table 1 denotes the space group that is obtained by periodic repetition of layer groups' elements along the axis perpendicular to the diperiodic plane. The diperiodic plane in Table 1 denotes the position of the layer single group plane within the corresponding 3D space group. The effective mass of both dispersions (1) and (2) is zero, as shown in the ESI† using the usual formula for \hat{m}_{eff} .³⁷

Analogous four-fold degeneracies are present in bulk 3D systems,^{16,17} on the surface of 3D systems³¹ or in 2D AFM crystals.^{18,19} These are all spinful degeneracies in the presence of

SOC. Dispersion of Rarita–Schwinger–Weyl fermions¹⁶ is proportional to $S_z \sqrt{q_x^2 + q_y^2 + q_z^2}$, where S_z is a projection of pseudo-spin $S = 3/2$ along the z -axis, while the unconventional fermion at the BZ center of RhSi is a combination of two $S = 1/2$ and two $S = 3/2$ states with a similar dispersion.¹⁷ In 2D AFM systems the dispersion $\pm \sqrt{q_x^2 + q_y^2}$ is double degenerate,^{18,19} and the same holds for surface Dirac fermions.³¹ The dispersion (2) differs from these Dirac-like dispersions, it is a property specific to 2D materials and consequently falls into the range of nanophysics.

Orbital wave functions must belong to an allowed irrep at a given point in the BZ. This statement is valid irrespective of strength of electronic correlations, since the Coulomb repulsion between electrons has the same transformation properties as the rest of the Hamiltonian. The allowed irreps of the groups listed in Table 1 are the only ones at these points of the BZ, hence the electronic correlations cannot change the form of the dispersion (2) as long as TRS and crystal symmetries are preserved. Even if the band picture fails the energy of all electrons in the crystal has dispersion (2). If one acts simultaneously by a space group element to radius vector of every electron in the crystal the many-body wave function has the same symmetry as the single-particle wave function of the corresponding non-interacting model. On the other hand, a combination of SOC and Hubbard interaction can result in an AFM order, which then breaks TRS.^{46,47} The same effect might occur even without SOC.⁴⁸ Our analysis does not refer to such cases so a detailed *ab initio* investigation of particular material should show whether transition to the AFM order occurs.

Symmetry of the crystal lattice is responsible for (an)isotropy of single crystals.⁴⁹ For example, isotropy of the electric susceptibility tensor in silicon is caused by the cubic symmetry, while the in-plane isotropy of graphene is caused by the hexagonal symmetry. In our cases, crystal axes are maximally of the second order, the irreps of the corresponding point groups are all one-dimensional and the materials belonging to layer groups listed in Table 1 are expected to be *anisotropic*.

From the analysis of irreps of layer double groups⁵⁰ we conclude that in the presence of SOC, originally eight-fold, spinful degeneracy splits into four doubly spinful degenerate levels for Dg33 and two four-fold spinful degenerate levels for Dg43 and Dg45. Since Dg43 and Dg45 contain inversion, bands are at least spinful double-degenerate, so the four-fold spinful degenerate level cannot split into four non-degenerate ones along *e.g.* the BZ-diagonal. On the other hand, layer double group

Table 1 Layer single groups hosting the dispersion (2) in the vicinity of the BZ corners: $\mathbf{k}_0 = (\pm\pi/a, \pm\pi/b)$. The notation for layer- and space-groups are according to Kopsky and Litvin⁴⁴ and Hahn,⁴⁵ respectively. The x -, y - and z -axes are along a -, b - and c -directions of the orthorhombic 3D unit cell, respectively. The notation for allowed representation in the last column is according to the Bilbao Crystallographic Server.³² Symbol \Leftrightarrow denotes equivalence between representations. In all three cases the little group $G(\mathbf{k}_0)$ is the whole layer single group

Layer single group	Corresponding space group	Diperiodic plane	irreps R at \mathbf{k}_0			
Dg33	$pb2_1a$	29	$Pca2_1$	C_{2v}^5	$y = 0$	$U_1 \Leftrightarrow U_1^*$
Dg43	$p2/b2_1/a2/a$	54	$P2_1/c2/c2/a$	D_{2h}^8	$y = 0$	$U_1, U_2 \Leftrightarrow U_1^*$
Dg45	$p2_1/b2_1/m2/a$	57	$P2/b2_1/c2_1/m$	D_{2h}^{11}	$x = 0$	$T_1, T_2 \Leftrightarrow T_1^*$

Dg33 does not support four-fold degeneracy at the BZ corners, which is necessary for FT dispersion. We conclude that SOC destroys FT dispersion at BZ corners of layer groups from Table 1. This result is valid irrespective of the strength of SOC. The four-fold orbital, and therefore eight-fold spinful degeneracy in layer single groups from Table 1 leads to electron band filling of $8n$ ($n = 1, 2, 3, \dots$), as a necessary condition for bands to be either completely filled or completely empty.^{51,52} This requirement remains even in the SOC case.²⁸ In fact Dg33, Dg43 and Dg45 are the only layer double groups with band filling $8n$ necessary for insulating systems.²⁸ In contrast to layer single groups from Table 1, essential eight-fold spinful degeneracy does not exist in their double group counterparts.⁵⁰ Instead, four spinful double-degenerate bands are tangled together in an hourglass manner in double-Dg43 and Dg45, while in non-centrosymmetric double-Dg33, eight non-degenerate bands form a “cat’s cradle” structure.²⁸ Analysis of band connectivity²⁸ for double-Dg33, Dg43 and Dg45 confirms our prediction of SOC splitting for bands at the corners of the BZ for groups from Table 1.

Since there is only one FT dispersion in the first BZ of each group from Table 1, it is interesting to investigate if band topology requires appearance of additional dispersions somewhere else in the first BZ. According to Chern, the following integral must be an integer C_n :

$$C_n = \frac{i}{2\pi} \int \int_{1^{\text{st}} \text{ BZ}} \nabla_{\mathbf{q}} \times \langle \psi_n(\mathbf{q}) | \nabla_{\mathbf{q}} \psi_n(\mathbf{q}) \rangle \cdot d^2\mathbf{S}, \quad (13)$$

where ψ_n is the eigenstate of n^{th} level, C_n is the Chern number, while $i\nabla_{\mathbf{q}} \times \langle \psi_n(\mathbf{q}) | \nabla_{\mathbf{q}} \psi_n(\mathbf{q}) \rangle$ is the Berry curvature.^{11,53} In the case of graphene, each Dirac point gives contribution of $1/2$ to the C_n and consequently, the number of Dirac points in the first BZ must be even. This is a 2D version of the Fermion doubling theorem. In contrast to graphene, our dispersion leads to zero Berry curvature for each of four states in each of the three groups. Consequently, the Berry phase is zero along any closed contour in the BZ, which gives $C_n = 0$ for all $n = 1, 2, 3, 4$. It follows that topology does not forbid FT to be the only dispersion at the Fermi level. Similar conclusion holds for *e.g.* AFM Dirac cone, where the contact point is also four-fold degenerate.¹⁸

Next we discuss the behavior of FT dispersion under strain. Application of strain that deforms the rectangular primitive cell into an oblique one, lowers the symmetry from a Dg33 to a Dg5 layer group, *i.e.* from Dg43 and Dg45 to Dg7. Since both Dg5 and Dg7 necessarily host the semi-Dirac dispersion,⁵⁴ FT dispersion splits into two pairs of semi-Dirac cones. The Chern number of semi-Dirac dispersion is zero, so such bands are topologically trivial. It follows that any linear combination of single band Chern numbers, such as mirror Chern number or spin Chern number, is also zero in this case. For strain that does not deform the rectangular primitive cell, the behavior of FT dispersion is determined by *translationengleiche* subgroups of Dg33, Dg43 and Dg45. As detailed analysis of band degeneracies in all layer single groups shows, breaking of horizontal

glide plane symmetry of Dg33, splits an FT point into two spinless double-degenerate points, both belonging to double spinless degenerate lines. Such splitting occurs also in Dg43 and Dg45, when one breaks any symmetry element of their subgroup Dg33. On the other hand, breaking of any element belonging to Dg43 or Dg45 but not to Dg33 gives the final group Dg33 and FT states are robust against such deformations.

Density of states (DOS) per unit area/volume for the n^{th} energy band is given by the following formula: $\rho_n(\epsilon) = (1/2\pi)^{D_{\text{im}}} \int \int_{1^{\text{st}} \text{ BZ}} \delta(\epsilon - \epsilon_n(\mathbf{q})) d^{D_{\text{im}}}\mathbf{q}$. Here, the dimensionality D_{im} is equal to three (two) for 3D (2D) systems. For Dirac dispersion $\pm v|\mathbf{q}|$ in 3D (in 2D), it is convenient to change to spherical (polar) coordinates. DOS is proportional to $\int_0^{\text{bzb}} q^{D_{\text{im}}-1} \delta(\epsilon - vq) dq$, where the BZ border bzb depends on the azimuthal and polar angles. For a sufficiently small energy ϵ measured from the bands contact point, we obtain, after including the particle-hole symmetry, $\rho_n(\epsilon) \sim |\epsilon|$ for 2D, *i.e.* $\rho_n(\epsilon) \sim \epsilon^2$ for 3D Dirac dispersion. In both cases, DOS becomes vanishingly small in the vicinity of contact points of the cones. This result refers, among other cases, also to four-fold spinful degenerate fermions in 3D.^{16,17} On the other hand, change to polar coordinates does not help in calculating DOS for dispersion (2). It is more convenient to introduce linear transformations of q_1 and q_2 such that expression under the Dirac delta function contains only one variable of integration. Details of calculations are given in the ESI,[†] while the final result is:

$$\rho(\epsilon) \approx \frac{3}{\pi\hbar} \left[\frac{1}{av_b} + \frac{1}{bv_a} \right], \quad (14)$$

with degeneracy due to the spin included. Here a and b are lattice constants while v_a and v_b are Fermi velocities along a and b . It is worth noting that DOS of FT is constant around E_F in contrast to DOS of Dirac states in graphene. This unique coexistence of zero electron effective mass and non-zero DOS at E_0 might have consequences on *e.g.* charge transport properties. For example, a smaller sensitivity of conductance is expected when charged impurities are introduced in materials with FT states.

4. *Ab initio* search for realistic materials

Next we report examples of (meta)stable 2D materials with the desired layer groups predicted using *ab initio* calculations. We have developed and utilized software that automatically searches for materials with a given group, analyzes their stability and band structure. The outline of the algorithm is listed in the ESI.[†] Since the atomic SOC strength increases as the fourth power of the atomic number,¹³ we limited our search only to light elements of the periodic table. For the sake of demonstration of the new electronic dispersion in real materials, we have searched for stable crystals with the above

stated symmetry groups among a few light elements, including B, C, Si and P. These are known to build stable 2D materials of various crystal symmetries and have negligible SOC. Note that the materials presented here are for demonstration purposes only, without intent to be a complete list. More elemental crystals with given symmetries are possible, while the list exponentially grows when compounds of two or more elements per unit cell are considered. Our symmetry arguments do not determine the position of FT states on the energy scale, so it is not guaranteed that the Fermi level will cross the energy near E_0 . We have applied band filling theory^{28,51,52} to our groups and found that the number of valence electrons per primitive cell must be an odd multiple of four, for FT states to touch exactly at E_F and that no other bands cross the Fermi level. The simplest structures satisfying these necessary (but non-sufficient) conditions have four identical nuclei in the primitive cell and belong to Dg45. The structures are listed in Table 2.

Note that we mean the *structural stability* here when we write about stability. Our DFT calculations have been conducted for the materials in an absolute vacuum. This has been a common approach in related papers.^{15–18,20,27,30,31} Here we propose a new class of materials which may include dozens of materials. Their chemical stability, *i.e.* stability in the atmosphere and reactivity with oxygen and other chemicals depend on the particular material's chemical composition, hence the chemical stability varies among materials in the class. For instance, phosphorene (double layer) has a Dg45 symmetry group (hence it belongs to the new class), while its reactivity with hydrogen, oxygen and fluorine has been analyzed in detail.⁵⁵ Questions of chemical stability of other found and yet to be found materials in the new class are to be answered in future research.

A stable structure with FT contact points positioned exactly at the Fermi level [P(Dg45), marked with bold letters in Table 2] is shown in Fig. 1(a). It consists of zig-zag chains of P atoms placed alternately at two parallel planes. The potential energy surface (PES) of elemental phosphorus has multiple local minima, *i.e.* many allotropes have been recently predicted,⁵⁶ hence there are numerous (meta)stable phases of phosphorus with different symmetries. P(Dg45) is a new one, placed at the distinct local minimum of PES in the configuration subspace with the Dg45 group and 4-fold multiplicity of Wyckoff positions [Fig. 1(b)]. Its stability is further confirmed by molecular dynamics simulations at 100 K.

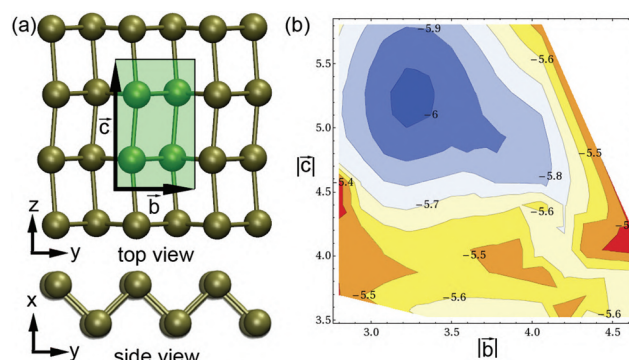


Fig. 1 Example of a stable structure with FT states at E_F . Top and side views of the optimized geometry of P(Dg45) is shown in panel (a). An elementary unit cell is marked with a green rectangle together with lattice vectors. Potential energy surface (atomization energy is given in eV per atom) in the configuration space constrained by the Dg45 group and 4-fold multiplicity of Wyckoff positions is shown in (b). The lattice parameters are given in Angstroms. Calculations are not done in the white region of panel (b) since the search algorithm predetermined instability of the crystal in this region.

The band structure of P(Dg45) along lines between high symmetry points is shown in Fig. 2(a). At $Y-R-Z$ section of the BZ, four states touch at E_F (both upper and lower states are doubly spinless degenerate), yielding 4-fold spinless degeneracy at the point of contact (E_F). Constant and non-zero DOS in the vicinity of E_F confirms our prediction given by eqn (14). The bands around R point obey the electron-hole symmetry, in agreement with our discussion related to eqn (9). The Fermi velocities of these states in the $Y-R$ and $R-Z$ directions are $1.08 \times 10^6 \text{ m s}^{-1}$ and $0.46 \times 10^6 \text{ m s}^{-1}$, which are in the range of the Fermi velocity of graphene.

The Fermi velocity of P(Dg45) is highly anisotropic. Therefore anisotropic electronic properties are expected to be similar to those of doped phosphorene.⁵⁷ The 2-fold spinless degeneracy of both lower and upper bands at R is lifted along the diagonal direction ($\Gamma-R$). Note another set of bands between Z and Γ , with 2-fold spinless degeneracy below E_F . More geometry details of the states around R are visible in Fig. 2(b). These states look exactly the same as the symmetry analysis predicted above: the FT states consisting of two pyramid-like and two paper fortune teller-like bands that touch at their tips and two lines, respectively. Sharp edges of the dispersion are unique among the electronic structure of

Table 2 Examples of stable 2D crystals with the Dg45 group. Mult. is multiplicity of Wyckoff position. E_{at} is atomization energy, b and c are lattice parameters. Coordinates of only one atom are given for each element. Other coordinates can be obtained from Wyckoff positions. $\Delta E_F = E_{\text{FT}} - E_F -$ energy difference between the Fermi level and nearest FT states. Group velocities v_b and v_c are calculated using $v_j = \frac{1}{\hbar} \frac{\partial E(k_1, k_2)}{\partial k_j}$ where index j corresponds to b or c lattice directions. A corresponding stable structure for carbon was not found

Element	E_{at} [eV per atom]	b [Å]	c [Å]	Coordinates [Å]	ΔE_F [eV]	v_b [10^6 m s^{-1}]	v_c [10^6 m s^{-1}]
B	-6.51	3.12	2.97	(0.390 0.387 0.743)	-0.65	1.22	1.52
Si	-5.56	3.74	4.64	(0.765 0.583 1.160)	-2.30	0.91	0.79
P	-6.03	3.22	5.24	(0.780 0.708 1.310)	0.00	1.08	0.40

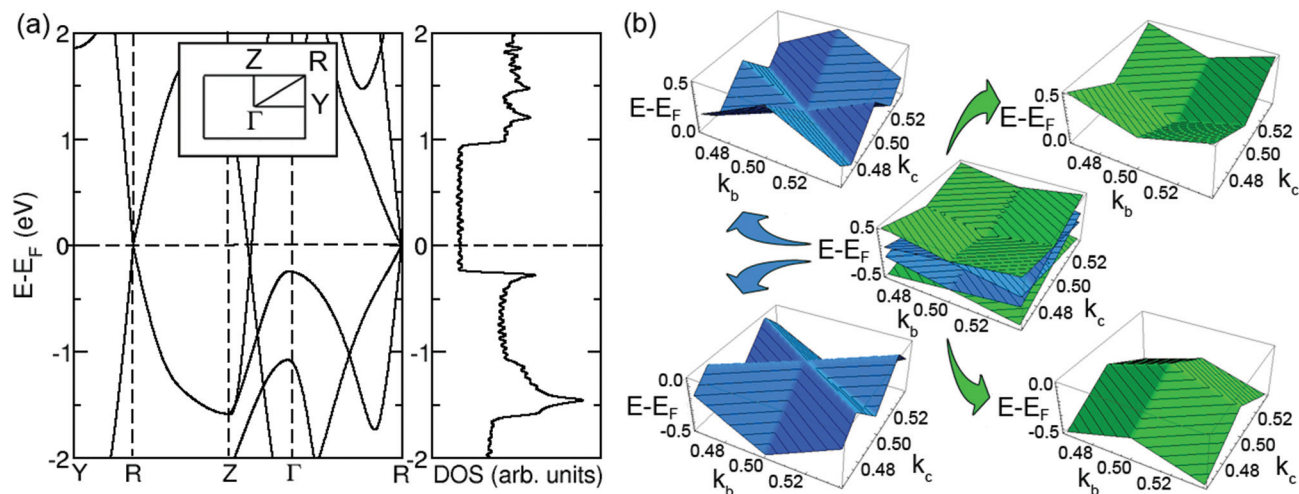


Fig. 2 The band structure of P(Dg45). (a) Electronic band structure along the lines between high-symmetry k -points (left panel) and the corresponding density of states (right panel). (b) FT states consisting of pyramidal (green) and paper fortune teller-like (blue) bands at point R . Energies are in units of eV relative to E_F , k -points are in units of $2\pi/|b|$ and $2\pi/|c|$. Coordinates of the R -point are (0.5, 0.5), while the R - Z direction (R - Y direction) is parallel to the k_b (k_c) axis.

any known crystal, and particularly in contrast to the smooth features of Dirac cones.

In order to image experimentally the sharp edges as the unique signature of the FT state, angle-resolved photoemission spectroscopy (ARPES)⁵⁸ can be utilized. ARPES can probe the momentum-dependent electronic band structure of 2D materials providing detailed information on the band dispersion and Fermi surface. Importantly for the fine structural feature of edges, recent progress of this technique allows ARPES measurements with a precision of roughly 1 meV energy resolution and 0.1 degree angular resolution. Prior to application of ARPES the material should be doped to move the Fermi level from the contact point and reach a doped Fermi surface with edges. Doping can be achieved by electron transfer between the target material and a substrate which acts as a donor or an acceptor of electrons. In order to preserve the symmetry, the donor/acceptor should be sputtered to both surfaces of the target material. The contact between the substrate and only one face of the sample would reduce the symmetry of the system and open a gap. The same holds for gating, when an electric field is applied perpendicularly to the sample. These symmetry arguments explain *e.g.* the gap opening in bilayer graphene under gating.⁵⁹ On the other hand, adding dopant elements to the target material in a way that preserves the original symmetry does not affect the FT dispersion. Even though preserving symmetry in highly doped systems is a formidable task, a light doping, in percent or even ppm ranges, would be sufficient for shifting of the Fermi level from the contact points, depending on a particular material. Light doping is still negligible for breaking of crystal symmetry. Other than ARPES, inverse photoemission spectroscopy can be used to probe the unoccupied states in the electronic band structure. In addition to the edges as a very unique feature of

the novel FT state, transport measurements would address the anisotropic electronic nature of the states.

5. Conclusions

In conclusion, we have established a full classification of states with linear dispersions in non-magnetic, time-reversal symmetric 2D materials with a negligible spin-orbit coupling, based on group theory analysis, and found that only one additional massless state to the Dirac one is possible. These states have not only unique and interesting geometric forms, but they also can open new horizons for both fundamental research and applications. For instance, these fermions in 2D materials do not have a counterpart in elementary particle physics, in analogy to some new fermions predicted for the 3D space groups.^{15–17,20} The sharp edges in the electronic bands have been neither predicted nor measured before, so their existence in the FT states may spawn new phenomena in solid state materials. Materials with FT bands can be competitive to the popular phosphorene due to the importance of anisotropy of its electronic structure.⁵⁷ Our unified classification of linearly dispersive bands paves the way to engineer new materials with Dirac and FT states. We hope that findings presented here will be of great motivation for experimental groups to bring these materials into existence.

Author contributions

VD performed the symmetry group analysis, discovered FT dispersion, analytically calculated the effective mass, density of states and the Berry curvature, and wrote the corresponding

parts of the manuscript. IP developed and used the software for *ab initio* search, conceptualized and wrote the larger part of the manuscript. RG initiated the research with the idea that Dirac dispersion can be a consequence of symmetry.

Conflicts of interest

There are no conflicts to declare.

Acknowledgements

We are thankful to Jelena Pešić, Marko Spasenović and Andrea Damascelli for discussions and suggestions related to this work. DFT calculations were performed using computational resources at the Center of Surface and Nanoanalytics, Johannes Kepler University, Linz, Austria. We are grateful to Prof. Kurt Hingerl for providing the necessary computational resources at JKU. This work was supported by the Serbian Ministry of Education, Science and Technological Development under project numbers OI 171005 and III 45016.

References

- 1 K. S. Novoselov, A. K. Geim, S. V. Morozov, D. Jiang, Y. Zhang, S. V. Dubonos, I. V. Grigorieva and A. A. Firsov, *Science*, 2004, **306**, 666–669.
- 2 G. W. Semenoff, *Phys. Rev. Lett.*, 1984, **53**, 2449–2452.
- 3 A. H. Castro Neto, F. Guinea, N. M. R. Peres, K. S. Novoselov and A. K. Geim, *Rev. Mod. Phys.*, 2009, **81**, 109–162.
- 4 K. Bolotin, K. Sikes, Z. Jiang, M. Klima, G. Fudenberg, J. Hone, P. Kim and H. Stormer, *Solid State Commun.*, 2008, **146**, 351–355.
- 5 M. I. Katsnelson, K. S. Novoselov and A. K. Geim, *Nat. Phys.*, 2006, **2**, 620–625.
- 6 Y. Zhang, Y.-W. Tan, H. L. Stormer and P. Kim, *Nature*, 2005, **438**, 201–204.
- 7 X. Du, I. Skachko, F. Duerr, A. Luican and E. Y. Andrei, *Nature*, 2009, **462**, 192–195.
- 8 D. Akinwande, N. Petrone and J. Hone, *Nat. Commun.*, 2014, **5**, 5678.
- 9 A. K. Geim and I. V. Grigorieva, *Nature*, 2013, **499**, 419–425.
- 10 J. Wang, S. Deng, Z. Liu and Z. Liu, *Natl. Sci. Rev.*, 2015, **2**, 22–39.
- 11 M. Z. Hasan and C. L. Kane, *Rev. Mod. Phys.*, 2010, **82**, 3045–3067.
- 12 Z. K. Liu, B. Zhou, Y. Zhang, Z. J. Wang, H. M. Weng, D. Prabhakaran, S.-K. Mo, Z. X. Shen, Z. Fang, X. Dai, Z. Hussain and Y. L. Chen, *Science*, 2014, **343**, 864–867.
- 13 S. A. Yang, *SPIN*, 2016, **06**, 1640003.
- 14 S. M. Young, S. Zaheer, J. C. Y. Teo, C. L. Kane, E. J. Mele and A. M. Rappe, *Phys. Rev. Lett.*, 2012, **108**, 140405.
- 15 B. J. Wieder, Y. Kim, A. M. Rappe and C. L. Kane, *Phys. Rev. Lett.*, 2016, **116**, 186402.
- 16 P. Tang, Q. Zhou and S.-C. Zhang, *Phys. Rev. Lett.*, 2017, **119**, 206402.
- 17 G. Chang, S.-Y. Xu, B. J. Wieder, D. S. Sanchez, S.-M. Huang, I. Belopolski, T.-R. Chang, S. Zhang, A. Bansil, H. Lin and Z. M. Hasan, *Phys. Rev. Lett.*, 2017, **119**, 206401.
- 18 S. M. Young and B. J. Wieder, *Phys. Rev. Lett.*, 2017, **118**, 186401.
- 19 J. Wang, *Phys. Rev. B: Condens. Matter Mater. Phys.*, 2017, **95**, 115138.
- 20 B. Bradlyn, J. Cano, Z. Wang, M. G. Vergniory, C. Felser, R. J. Cava and B. A. Bernevig, *Science*, 2016, **353**, aaf5037.
- 21 L. A. Ponomarenko, R. V. Gorbachev, G. L. Yu, D. C. Elias, R. Jalil, A. A. Patel, A. Mishchenko, A. S. Mayorov, C. R. Woods, J. R. Wallbank, M. Mucha-Kruczynski, B. A. Piot, M. Potemski, I. V. Grigorieva, K. S. Novoselov, F. Guinea, V. I. Fal'ko and A. K. Geim, *Nature*, 2013, **497**, 594–597.
- 22 C.-H. Park, L. Yang, Y.-W. Son, M. L. Cohen and S. G. Louie, *Phys. Rev. Lett.*, 2008, **101**, 126804.
- 23 J. L. Mañes, *Phys. Rev. B: Condens. Matter Mater. Phys.*, 2012, **85**, 155118.
- 24 V. Damjanović and R. Gajić, *J. Phys.: Condens. Matter*, 2016, **28**, 085502.
- 25 V. Damjanović and R. Gajić, *J. Phys.: Condens. Matter*, 2016, **28**, 439401.
- 26 G. van Miert and C. M. Smith, *Phys. Rev. B: Condens. Matter Mater. Phys.*, 2016, **93**, 035401.
- 27 Z. Wang, A. Alexandradinata, R. J. Cava and B. A. Bernevig, *Nature*, 2016, **532**, 189–194.
- 28 B. J. Wieder and C. L. Kane, *Phys. Rev. B: Condens. Matter Mater. Phys.*, 2016, **94**, 155108.
- 29 S. M. Young and C. L. Kane, *Phys. Rev. Lett.*, 2015, **115**, 126803.
- 30 T. H. Hsieh, H. Lin, J. Liu, W. Duan, A. Bansil and L. Fu, *Nat. Commun.*, 2012, **3**, 982.
- 31 B. J. Wieder, B. Bradlyn, Z. Wang, J. Cano, Y. Kim, H.-S. Kim, A. M. Rappe, C. L. Kane and A. B. Bernevig, arXiv:1705.01617, 2017.
- 32 M. I. Aroyo, A. Kirov, C. Capillas, J. M. Perez-Mato and H. Wondratschek, *Acta Crystallogr., Sect. A: Found. Crystallogr.*, 2006, **62**, 115–128.
- 33 J. F. Cornwell, *Group Theory in Physics, Volume I*, Academic Press, 1984.
- 34 C. J. Bradley and A. P. Cracknell, *The Mathematical Theory of Symmetry in Solids*, Clarendon, 2010.
- 35 I. Milošević, B. Nikolić, M. Damnjanović and M. Krčmar, *J. Phys. A: Math. Gen.*, 1998, **31**, 3625.
- 36 C. Herring, *Phys. Rev.*, 1937, **52**, 361–365.
- 37 N. W. Ashcroft and N. D. Mermin, *Solid State Physics*, Saunders College Publishing, 1972.
- 38 J. Zak, *Phys. Rev. B: Condens. Matter Mater. Phys.*, 1982, **26**, 3010–3023.
- 39 B. Bradlyn, L. Elcoro, J. Cano, M. G. Vergniory, Z. Wang, C. Felser, M. I. Aroyo and A. B. Bernevig, *Nature*, 2017, **547**, 298–305.

- 40 L. Michel and J. Zak, *Phys. Rep.*, 2001, **341**, 377–395.
- 41 L. D. Landau and L. M. Lifshitz, *Quantum Mechanics: Non-Relativistic Theory*, Butterworth-Heinemann, 1981.
- 42 S. Katayama, A. Kobayashi and Y. Suzumura, *J. Phys. Soc. Jpn.*, 2006, **75**, 054705.
- 43 M. O. Goerbig, J.-N. Fuchs, G. Montambaux and F. Piéchon, *Phys. Rev. B: Condens. Matter Mater. Phys.*, 2008, **78**, 045415.
- 44 V. Kopsky and D. B. Litvin, *International Tables of Crystallography Volume E: Subperiodic Groups*, Kluwer Academic Publishers, 2002.
- 45 T. Hahn, *International Tables of Crystallography Volume A: Space-Group Symmetry*, Springer, 2005.
- 46 J.-M. Carter, V. V. Shankar, M. A. Zeb and H.-Y. Kee, *Phys. Rev. B: Condens. Matter Mater. Phys.*, 2012, **85**, 115105.
- 47 G. Sharma, Z. Zhao, P. Sarker, B. A. Nail, J. Wang, M. N. Huda and F. E. Osterloh, *J. Mater. Chem. A*, 2016, **4**, 2936–2942.
- 48 D. Di Sante, A. Hausoel, P. Barone, J. M. Tomczak, G. Sangiovanni and R. Thomale, *Phys. Rev. B: Condens. Matter Mater. Phys.*, 2017, **96**, 121106.
- 49 A. S. Nowick, *Crystal Properties Via Group Theory*, Cambridge University Press, 2005.
- 50 L. Elcoro, B. Bradlyn, Z. Wang, M. G. Vergniory, J. Cano, C. Felser, B. A. Bernevig, D. Orobengoa, G. de la Flor and M. I. Aroyo, *J. Appl. Crystallogr.*, 2017, **50**, 1457–1477.
- 51 H. Watanabe, H. C. Po, M. P. Zaletel and A. Vishwanath, *Phys. Rev. Lett.*, 2016, **117**, 096404.
- 52 H. Watanabe, H. C. Po, A. Vishwanath and M. Zaletel, *Proc. Natl. Acad. Sci. U. S. A.*, 2015, **112**, 14551–14556.
- 53 M. V. Berry, *Proc. R. Soc. London, Ser. A*, 1984, **392**, 45–57.
- 54 V. Damjanović and R. Gajić, *J. Phys.: Condens. Matter*, 2017, **29**, 185503.
- 55 D. W. Boukhvalov, A. N. Rudenko, D. A. Prishchenko, V. G. Mazurenko and M. I. Katsnelson, *Phys. Chem. Chem. Phys.*, 2015, **17**, 15209–15217.
- 56 J. Guan, Z. Zhu and D. Tománek, *Phys. Rev. Lett.*, 2014, **113**, 046804.
- 57 J. Kim, S. S. Baik, S. H. Ryu, Y. Sohn, S. Park, B.-G. Park, J. Denlinger, Y. Yi, H. J. Choi and K. S. Kim, *Science*, 2015, **349**, 723–726.
- 58 A. Damascelli, *Phys. Scr.*, 2004, **T109**, 61–74.
- 59 K. F. Mak, C. H. Lui, J. Shan and T. F. Heinz, *Phys. Rev. Lett.*, 2009, **102**, 256405.

Electronic Supplementary Information for the paper “Fortune teller fermions in two-dimensional materials” by V. Damjanović, I. Popov and R. Gajić

Classification of linear states in 2D

We first show that in the vicinity of spinless double degenerate point, 2D Dirac bands are the only possible massless bands. Eigenvalues of any two-component, \mathbf{k} -dependent Hamiltonian $\hat{H}(\mathbf{k})$ are:

$$E_{1,2}(\mathbf{k}) = f_0(\mathbf{k}) \pm \sqrt{\sum_{j=1}^3 [f_j(\mathbf{k})]^2}, \quad (\text{S1})$$

where

$$(\forall j = \overline{0,3}) f_j(k) = \frac{1}{2} \text{Tr}[\hat{H}(\mathbf{k}) \hat{\sigma}_j] \quad (\text{S2})$$

are real functions and $\hat{\sigma}_{1,2,3}$ ($\hat{\sigma}_0$) are the Pauli matrices (is the unit matrix). If \mathbf{k}_0 is crossing point of two bands and \mathbf{q} is a wave vector of small modulus then $f_1(\mathbf{k}_0) = f_2(\mathbf{k}_0) = f_3(\mathbf{k}_0) = 0$ and:

$$E_{1,2}(\mathbf{k}_0 + \mathbf{q}) \approx f_0(\mathbf{k}_0 + \mathbf{q}) \pm \sqrt{uq_1^{2n_1} + vq_2^{2n_2}} \quad (\text{S3})$$

In Eq. (S3), u and v are positive quantities, n_1 and n_2 are natural numbers and q_1 and q_2 are projections of \mathbf{q} along certain, mutually orthogonal directions. Since the expression under the square root in Eq. (S3) cannot be negative, the powers on q_1 , q_2 must be even. Eq. (S3) is obtained by the Taylor expansion of f_j , ($j=1, 2, 3$) around the point \mathbf{k}_0 . In order to obtain the effective mass we need second order derivatives with respect to q_1 , q_2 at

$q=0$. If x denotes q_1 or q_2 , the second derivative of $|x|^n$ ($n=2,3,4,\dots$) depends on whether n is even ($n=2s, s=1,2,3,\dots$):

$$\frac{d^2}{dx^2} |x|^{2s} = 2s(2s - 1)x^{2s-2},$$

or odd ($n=2s+1$):

$$\frac{d^2}{dx^2} |x|^{2s+1} = 2s(2s - 1)|x|^{2s-1} + 4sx^{2s-1}\theta(x) + 2x^{2s}\delta(x).$$

Here $\theta(x)=1$ ($\theta(x)=-1$) for $x>0$ ($x<0$) and $\delta(x)$ is Dirac delta-function. For $n=2$ second derivative at $x=0$ is a positive constant, which gives rise to finite effective mass. For $n>2$ second derivative is zero at $x=0$ and the contribution to the effective mass comes from second derivatives of f_0 in Eq. (S3). Again, the effective mass is finite. The only remaining case $n_1=n_2=1$ gives zero effective mass and corresponds to 2D Dirac-like dispersion (see Eq. (1) of the main text and this text below).

Next, we classify all possibilities for linear dispersions in the band structure of 2D materials. In order to achieve this aim we define a set of parameters, which values determine possible existence of linear dispersions in 2D crystals. If $G(\mathbf{k}_0)$ is the group of the wave vector \mathbf{k}_0 and R is allowed [32] (relevant [33], small [34]) irreducible representation (irrep) of $G(\mathbf{k}_0)$, then the set of parameters consists of

-equivalence of \mathbf{k}_0 and its inverse $-\mathbf{k}_0$,

-dimensionality of representation R ,

-reality of representation R .

We consider all possible symmetry groups of crystals which are periodic in 2 spatial directions and finite in the perpendicular direction. These are the so called layer groups (or diperiodic groups). Layer groups have only 1D or 2D allowed irreps [32, 35], while they can be real on one hand or pseudo-real or complex on the other hand. When complex conjugation is a symmetry operation, reality of irreps determines if it causes additional degeneracy. For single crystals the corresponding theory was developed in 1937 [36]. Therefore, each of these parameters can obtain one of two options; hence there are 8 possible combinations, as illustrated in figure S1.

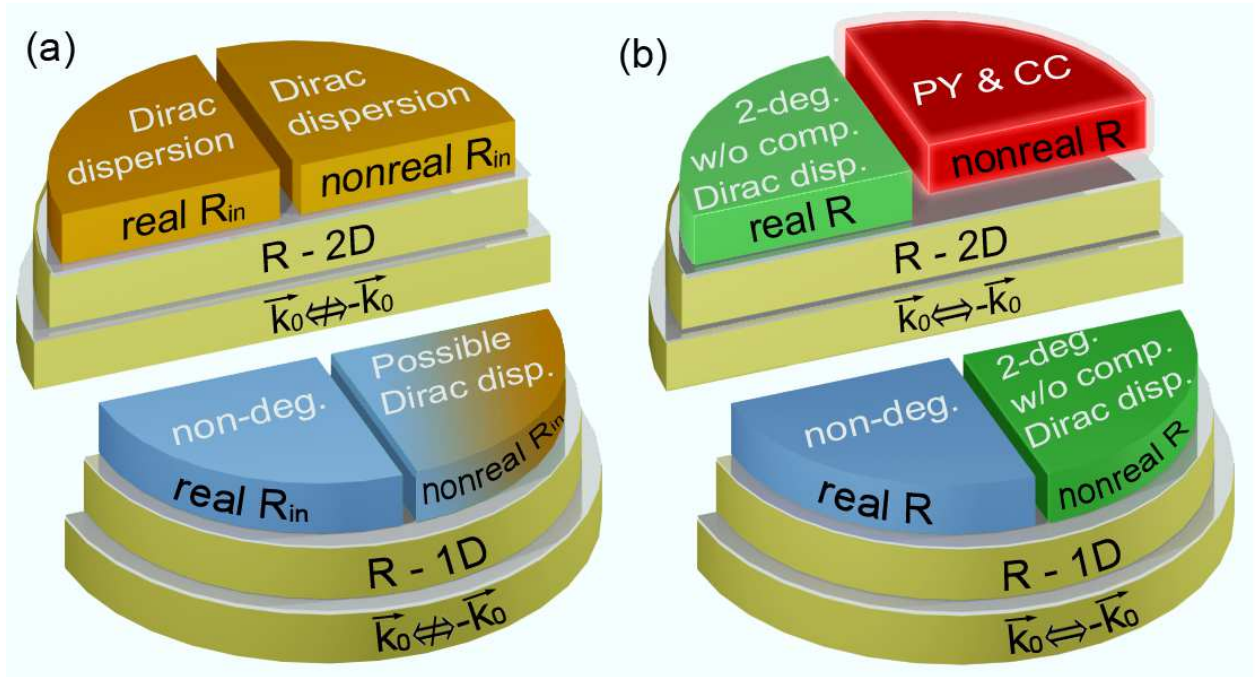


Figure S1. Full classification of linearly dispersive electronic bands in non-magnetic 2D materials based on symmetry conditions. Panel (a) corresponds to the case $\mathbf{k}_0 \not\leftrightarrow -\mathbf{k}_0$ and panel (b) to the case $\mathbf{k}_0 \leftrightarrow -\mathbf{k}_0$. 2-deg. w/o comp. Dirac. disp. means doubly-degeneracy without complete Dirac dispersion, non-deg. means a non-degenerate state.

Firstly, we consider the case $\mathbf{k}_0 \not\leftrightarrow -\mathbf{k}_0$ (figure S1a). The wave vector \mathbf{k}_0 must have a locally maximal symmetry, otherwise linear dispersion cannot appear, due to either too many band contacts [S1] or none at all. If R is two-dimensional, and the irrep R_{in} of the whole layer group G , which is obtained by induction from R ($R_{in} = R \uparrow G$) is real, Dirac-like dispersion appears [24] (orange upper left section). If R_{in} is not real, $-\mathbf{k}_0$ is not in the star of \mathbf{k}_0 [32] than the additional degeneracy due to TRS does not appear. This case also leads to Dirac dispersion [24] (orange upper right section). In the last two cases double degeneracy at Dirac point is caused by the crystal symmetry. For R one-dimensional and R_{in} real (left panel blue section), the energy level E_0 at \mathbf{k}_0 is non-degenerate preventing Dirac dispersion in the vicinity of \mathbf{k}_0 . For R one-dimensional and R_{in} pseudoreal or complex (blue-orange section) there are two possibilities. If $-\mathbf{k}_0$ is not in the star of \mathbf{k}_0 , E_0 is non-degenerate while in the opposite case TRS causes E_0 to be double degenerate with a complete Dirac-like dispersion around \mathbf{k}_0 [25]. Next we consider the case $\mathbf{k}_0 \leftrightarrow -\mathbf{k}_0$ (figure S1b). If R is one-dimensional and real, the energy level E_0 at \mathbf{k}_0 is non-degenerate and linear dispersion cannot appear (right panel blue section). If R is one-dimensional and not real (right panel green section down), TRS causes E_0 to be double degenerate, but complete linear Dirac-like dispersion is not possible since the TRS causes $u_2=0$ (u_2 is a coefficient in the expression for Dirac dispersion [24], see the expression (1) in the main text). The same statement holds for two-dimensional, real R (right panel green section up). The remaining case in which R is two-dimensional and pseudoreal or complex will be treated in more detail in the main text (right panel red section).

Group-theoretical derivations

We show more details in obtaining the dispersion relation (2) of the manuscript. For obtaining irreps R of layer single groups we used Bilbao Crystallographic Server [32] for space groups that correspond to the layer single groups of interest. Obtained matrices are given in Tables S1-S3.

Table S1 Matrices of representation U_1 and 2DPV corresponding to $Dg33$. Dipericodic plane is xz .

$Dg33$	$(\hat{E} \vec{0})$	$(\hat{C}_2^z \frac{1}{2}\vec{a}_3)$	$(\hat{\sigma}_{xz} \frac{1}{2}\vec{a}_1)$	$(\hat{\sigma}_{yz} \frac{1}{2}\vec{a}_1 + \frac{1}{2}\vec{a}_3)$
U_1	$\begin{pmatrix} 1 & 0 \\ 0 & 1 \end{pmatrix}$	$\begin{pmatrix} i & 0 \\ 0 & -i \end{pmatrix}$	$\begin{pmatrix} 0 & -1 \\ 1 & 0 \end{pmatrix}$	$\begin{pmatrix} 0 & i \\ i & 0 \end{pmatrix}$
\hat{h}'	$\begin{pmatrix} 1 & 0 \\ 0 & 1 \end{pmatrix}$	$\begin{pmatrix} -1 & 0 \\ 0 & 1 \end{pmatrix}$	$\begin{pmatrix} 1 & 0 \\ 0 & 1 \end{pmatrix}$	$\begin{pmatrix} -1 & 0 \\ 0 & 1 \end{pmatrix}$

Table S2 Matrices of representation U_1 and 2DPV corresponding to $Dg43$. Dipericodic plane is xz .

$Dg43$	$(\hat{E} \vec{0})$	$(\hat{C}_2^z \frac{1}{2}\vec{a}_1)$	$(\hat{C}_2^y \frac{1}{2}\vec{a}_3)$	$(\hat{C}_2^x \frac{1}{2}\vec{a}_3 - \frac{1}{2}\vec{a}_1)$
U_1	$\begin{pmatrix} 1 & 0 \\ 0 & 1 \end{pmatrix}$	$\begin{pmatrix} 1 & 0 \\ 0 & -1 \end{pmatrix}$	$\begin{pmatrix} 0 & 1 \\ 1 & 0 \end{pmatrix}$	$\begin{pmatrix} 0 & -1 \\ 1 & 0 \end{pmatrix}$
\hat{h}'	$\begin{pmatrix} 1 & 0 \\ 0 & 1 \end{pmatrix}$	$\begin{pmatrix} -1 & 0 \\ 0 & 1 \end{pmatrix}$	$\begin{pmatrix} -1 & 0 \\ 0 & -1 \end{pmatrix}$	$\begin{pmatrix} 1 & 0 \\ 0 & -1 \end{pmatrix}$
$Dg43$	$(\hat{i} \vec{0})$	$(\hat{\sigma}_{xy} \frac{1}{2}\vec{a}_1)$	$(\hat{\sigma}_{xz} \frac{1}{2}\vec{a}_3)$	$(\hat{\sigma}_{yz} \frac{1}{2}\vec{a}_1 - \frac{1}{2}\vec{a}_3)$
U_1	$\begin{pmatrix} 0 & -i \\ i & 0 \end{pmatrix}$	$\begin{pmatrix} 0 & i \\ i & 0 \end{pmatrix}$	$\begin{pmatrix} -i & 0 \\ 0 & i \end{pmatrix}$	$\begin{pmatrix} -i & 0 \\ 0 & -i \end{pmatrix}$
\hat{h}'	$\begin{pmatrix} -1 & 0 \\ 0 & -1 \end{pmatrix}$	$\begin{pmatrix} 1 & 0 \\ 0 & -1 \end{pmatrix}$	$\begin{pmatrix} 1 & 0 \\ 0 & 1 \end{pmatrix}$	$\begin{pmatrix} -1 & 0 \\ 0 & 1 \end{pmatrix}$

Table S3 Matrices of representation T_1 and 2DPV corresponding to $Dg45$. Dipericodic plane is yz .

$Dg45$	$(\hat{E} \vec{0})$	$(\hat{C}_2^z \frac{1}{2}\vec{a}_3)$	$(\hat{C}_2^y \frac{1}{2}\vec{a}_2 + \frac{1}{2}\vec{a}_3)$	$(\hat{C}_2^x \frac{1}{2}\vec{a}_2)$
T_1	$\begin{pmatrix} 1 & 0 \\ 0 & 1 \end{pmatrix}$	$\begin{pmatrix} i & 0 \\ 0 & -i \end{pmatrix}$	$\begin{pmatrix} -i & 0 \\ 0 & -i \end{pmatrix}$	$\begin{pmatrix} 1 & 0 \\ 0 & -1 \end{pmatrix}$
\hat{h}'	$\begin{pmatrix} 1 & 0 \\ 0 & 1 \end{pmatrix}$	$\begin{pmatrix} -1 & 0 \\ 0 & 1 \end{pmatrix}$	$\begin{pmatrix} 1 & 0 \\ 0 & -1 \end{pmatrix}$	$\begin{pmatrix} -1 & 0 \\ 0 & -1 \end{pmatrix}$
$Dg45$	$(\hat{i} \vec{0})$	$(\hat{\sigma}_{xy} \frac{1}{2}\vec{a}_3)$	$(\hat{\sigma}_{xz} \frac{1}{2}\vec{a}_2 - \frac{1}{2}\vec{a}_3)$	$(\hat{\sigma}_{yz} \frac{1}{2}\vec{a}_2)$
T_1	$\begin{pmatrix} 0 & 1 \\ 1 & 0 \end{pmatrix}$	$\begin{pmatrix} 0 & -i \\ i & 0 \end{pmatrix}$	$\begin{pmatrix} 0 & -i \\ -i & 0 \end{pmatrix}$	$\begin{pmatrix} 0 & -1 \\ 1 & 0 \end{pmatrix}$
\hat{h}'	$\begin{pmatrix} -1 & 0 \\ 0 & -1 \end{pmatrix}$	$\begin{pmatrix} 1 & 0 \\ 0 & -1 \end{pmatrix}$	$\begin{pmatrix} -1 & 0 \\ 0 & 1 \end{pmatrix}$	$\begin{pmatrix} 1 & 0 \\ 0 & 1 \end{pmatrix}$

We obtain the matrices of representation $D = R \oplus R^*$ from matrices in Tables S1-S3 in the following way. If functions ψ_1 and ψ_2 belong to irreps R from Tables S1-S3, then ψ_1^* and ψ_2^* belong to irrep R^* so functions $\varphi_1 = (\psi_1 + \psi_1^*)/2$, $\varphi_2 = (\psi_1 - \psi_1^*)/(2i)$, $\varphi_3 = (\psi_2 + \psi_2^*)/2$ and $\varphi_4 = (\psi_2 - \psi_2^*)/(2i)$ transform according to the representation D . The final result is given in Tables S4-S6.

Table S4 Matrices of representation D corresponding to $Dg33$. Dipericodic plane is xz , while $\bar{1} = -1$.

$Dg33$	$(\hat{E} \vec{0})$	$(\hat{C}_2^z \frac{1}{2}\vec{a}_3)$	$(\hat{\sigma}_{xz} \frac{1}{2}\vec{a}_1)$	$(\hat{\sigma}_{yz} \frac{1}{2}\vec{a}_1 + \frac{1}{2}\vec{a}_3)$
D	$\begin{pmatrix} 1 & 0 & 0 & 0 \\ 0 & 1 & 0 & 0 \\ 0 & 0 & 1 & 0 \\ 0 & 0 & 0 & 1 \end{pmatrix}$	$\begin{pmatrix} 0 & \bar{1} & 0 & 0 \\ 1 & 0 & 0 & 0 \\ 0 & 0 & 0 & 1 \\ 0 & 0 & \bar{1} & 0 \end{pmatrix}$	$\begin{pmatrix} 0 & 0 & \bar{1} & 0 \\ 0 & 0 & 0 & \bar{1} \\ 1 & 0 & 0 & 0 \\ 0 & 1 & 0 & 0 \end{pmatrix}$	$\begin{pmatrix} 0 & 0 & 0 & \bar{1} \\ 0 & 0 & 1 & 0 \\ 0 & \bar{1} & 0 & 0 \\ 1 & 0 & 0 & 0 \end{pmatrix}$

Table S5 Matrices of representation D corresponding to $Dg43$. Dipericodic plane is xz , while $\bar{1} = -1$.

$Dg43$	$(\hat{E} \vec{0})$	$(\hat{C}_2^z \frac{1}{2}\vec{a}_1)$	$(\hat{C}_2^y \frac{1}{2}\vec{a}_3)$	$(\hat{C}_2^x \frac{1}{2}\vec{a}_3 - \frac{1}{2}\vec{a}_1)$
D	$\begin{pmatrix} 1 & 0 & 0 & 0 \\ 0 & 1 & 0 & 0 \\ 0 & 0 & 1 & 0 \\ 0 & 0 & 0 & 1 \end{pmatrix}$	$\begin{pmatrix} 1 & 0 & 0 & 0 \\ 0 & 1 & 0 & 0 \\ 0 & 0 & \bar{1} & 0 \\ 0 & 0 & 0 & \bar{1} \end{pmatrix}$	$\begin{pmatrix} 0 & 0 & 1 & 0 \\ 0 & 0 & 0 & 1 \\ 1 & 0 & 0 & 0 \\ 0 & 1 & 0 & 0 \end{pmatrix}$	$\begin{pmatrix} 0 & 0 & \bar{1} & 0 \\ 0 & 0 & 0 & \bar{1} \\ 1 & 0 & 0 & 0 \\ 0 & 1 & 0 & 0 \end{pmatrix}$
$Dg43$	$(\hat{i} \vec{0})$	$(\hat{\sigma}_{xy} \frac{1}{2}\vec{a}_1)$	$(\hat{\sigma}_{xz} \frac{1}{2}\vec{a}_3)$	$(\hat{\sigma}_{yz} \frac{1}{2}\vec{a}_1 - \frac{1}{2}\vec{a}_3)$
D	$\begin{pmatrix} 0 & 0 & 0 & \bar{1} \\ 0 & 0 & 1 & 0 \\ 0 & 1 & 0 & 0 \\ \bar{1} & 0 & 0 & 0 \end{pmatrix}$	$\begin{pmatrix} 0 & 0 & 0 & 1 \\ 0 & 0 & \bar{1} & 0 \\ 0 & 1 & 0 & 0 \\ \bar{1} & 0 & 0 & 0 \end{pmatrix}$	$\begin{pmatrix} 0 & \bar{1} & 0 & 0 \\ 1 & 0 & 0 & 0 \\ 0 & 0 & 0 & 1 \\ 0 & 0 & \bar{1} & 0 \end{pmatrix}$	$\begin{pmatrix} 0 & \bar{1} & 0 & 0 \\ 1 & 0 & 0 & 0 \\ 0 & 0 & 0 & \bar{1} \\ 0 & 0 & 1 & 0 \end{pmatrix}$

Table S6 Matrices of representation D corresponding to $Dg45$. Dipericodic plane is yz , while $\bar{1} = -1$.

$Dg45$	$(\hat{E} \vec{0})$	$(\hat{C}_2^z \frac{1}{2}\vec{a}_3)$	$(\hat{C}_2^y \frac{1}{2}\vec{a}_2 + \frac{1}{2}\vec{a}_3)$	$(\hat{C}_2^x \frac{1}{2}\vec{a}_2)$
D	$\begin{pmatrix} 1 & 0 & 0 & 0 \\ 0 & 1 & 0 & 0 \\ 0 & 0 & 1 & 0 \\ 0 & 0 & 0 & 1 \end{pmatrix}$	$\begin{pmatrix} 0 & 1 & 0 & 0 \\ \bar{1} & 0 & 0 & 0 \\ 0 & 0 & 0 & \bar{1} \\ 0 & 0 & 1 & 0 \end{pmatrix}$	$\begin{pmatrix} 0 & \bar{1} & 0 & 0 \\ 1 & 0 & 0 & 0 \\ 0 & 0 & 0 & \bar{1} \\ 0 & 0 & 1 & 0 \end{pmatrix}$	$\begin{pmatrix} 1 & 0 & 0 & 0 \\ 0 & 1 & 0 & 0 \\ 0 & 0 & \bar{1} & 0 \\ 0 & 0 & 0 & \bar{1} \end{pmatrix}$
$Dg45$	$(\hat{i} \vec{0})$	$(\hat{\sigma}_{xy} \frac{1}{2}\vec{a}_3)$	$(\hat{\sigma}_{xz} \frac{1}{2}\vec{a}_2 - \frac{1}{2}\vec{a}_3)$	$(\hat{\sigma}_{yz} \frac{1}{2}\vec{a}_2)$
D	$\begin{pmatrix} 0 & 0 & 1 & 0 \\ 0 & 0 & 0 & 1 \\ 1 & 0 & 0 & 0 \\ 0 & 1 & 0 & 0 \end{pmatrix}$	$\begin{pmatrix} 0 & 0 & 0 & \bar{1} \\ 0 & 0 & 1 & 0 \\ 0 & 1 & 0 & 0 \\ \bar{1} & 0 & 0 & 0 \end{pmatrix}$	$\begin{pmatrix} 0 & 0 & 0 & \bar{1} \\ 0 & 0 & 1 & 0 \\ 0 & \bar{1} & 0 & 0 \\ 1 & 0 & 0 & 0 \end{pmatrix}$	$\begin{pmatrix} 0 & 0 & \bar{1} & 0 \\ 0 & 0 & 0 & \bar{1} \\ 1 & 0 & 0 & 0 \\ 0 & 1 & 0 & 0 \end{pmatrix}$

Group projector to the totally symmetric irreducible representation is given by:

$$\hat{P} = \frac{1}{|G(\mathbf{k}_0)|} \sum \hat{D} \otimes \hat{D} \otimes \hat{h}'$$

where the sum is over little group elements $G(\mathbf{k}_0)$. In our three cases this included the whole layer single group. Obtained projection operator is 32-dimensional. By applying \hat{P} to general 32-component vector consistent with TRS-constrained matrix \hat{W} :

$$\hat{W} = i \begin{pmatrix} 0 & \langle \mathbf{v}_1 | & \langle \mathbf{v}_2 | & \langle \mathbf{v}_3 | \\ -\langle \mathbf{v}_1 | & 0 & \langle \mathbf{v}_4 | & \langle \mathbf{v}_5 | \\ -\langle \mathbf{v}_2 | & -\langle \mathbf{v}_4 | & 0 & \langle \mathbf{v}_6 | \\ -\langle \mathbf{v}_3 | & -\langle \mathbf{v}_5 | & -\langle \mathbf{v}_6 | & 0 \end{pmatrix},$$

we get symmetry constrained vectors \mathbf{v}_j . Final result is given in the Table S7.

Table S7 Form of vectors \mathbf{v}_j ($j = 1, 2, \dots, 6$) required by symmetry, for the layer single groups $Dg33$, $Dg43$ and $Dg45$. Components of vectors are along \mathbf{a} - and \mathbf{c} -axes for groups $Dg33$ and $Dg43$, and \mathbf{b} - and \mathbf{c} -axes for group $Dg45$ respectively. The \mathbf{a} -, \mathbf{b} - and \mathbf{c} -axes are orthorhombic axes for corresponding space groups 29, 54 and 57 respectively.

	$Dg33$	$Dg43$	$Dg45$
\mathbf{v}_1	$\begin{pmatrix} 0 \\ v_{1c} \end{pmatrix}$	$\begin{pmatrix} 0 \\ v'_{1c} \end{pmatrix}$	$\begin{pmatrix} 0 \\ 0 \end{pmatrix}$
\mathbf{v}_2	$\begin{pmatrix} v_{2a} \\ v_{2c} \end{pmatrix}$	$\begin{pmatrix} v'_{2a} \\ 0 \end{pmatrix}$	$\begin{pmatrix} v''_{2b} \\ v_{2c} \end{pmatrix}$
\mathbf{v}_3	$\begin{pmatrix} 0 \\ v_{3c} \end{pmatrix}$	$\begin{pmatrix} v'_{3a} \\ 0 \end{pmatrix}$	$\begin{pmatrix} 0 \\ v_{3c} \end{pmatrix}$
\mathbf{v}_4	$\begin{pmatrix} 0 \\ v_{3c} \end{pmatrix}$	$\begin{pmatrix} v'_{3a} \\ 0 \end{pmatrix}$	$\begin{pmatrix} 0 \\ v_{3c} \end{pmatrix}$
\mathbf{v}_5	$\begin{pmatrix} v_{2a} \\ -v_{2c} \end{pmatrix}$	$\begin{pmatrix} -v'_{2a} \\ 0 \end{pmatrix}$	$\begin{pmatrix} v''_{2b} \\ -v_{2c} \end{pmatrix}$
\mathbf{v}_6	$\begin{pmatrix} 0 \\ v_{1c} \end{pmatrix}$	$\begin{pmatrix} 0 \\ -v'_{1c} \end{pmatrix}$	$\begin{pmatrix} 0 \\ 0 \end{pmatrix}$

If we insert values for \mathbf{v}_j into the Eq. (9) of the main text, we get the dispersion (2). Note that the form of Hamiltonian \hat{H}' required by the Table S7 is valid only in the basis that belongs to the representation D given in Tables S4-S6. On the other hand, eigenvalues of \hat{H}' are invariant, and are therefore the same in every basis.

The effective mass calculation

Next we show that the dispersion (2) leads to zero effective mass. We take the dispersion for $E_1(\mathbf{q})$, obtained from Eq. (2) of the main manuscript by taking plus signs, as an example. The proof for other bands, including Dirac-like (1) is analogous. Let us define the matrix:

$$\hat{S}(q_1, q_2) = \begin{pmatrix} \frac{\partial^2}{(\partial q_1)^2} E_1(q_1, 0) & \left[\frac{\partial^2}{\partial q_1 \partial q_2} E_1(q_1, q_2) \right]_{q_2=0} \\ \left[\frac{\partial^2}{\partial q_2 \partial q_1} E_1(q_1, q_2) \right]_{q_1=0} & \frac{\partial^2}{(\partial q_2)^2} E_1(0, q_2) \end{pmatrix}.$$

The matrix element $\left[\frac{\partial^2}{\partial q_1 \partial q_2} E_1(q_1, q_2) \right]_{q_2=0}$ means that firstly we take the derivative with respect to q_2 , than take $q_2=0$, and then take derivative with respect to q_1 (and analogously for the other off-diagonal element). The matrix \hat{S} in terms of Dirac delta function reads:

$$\hat{S}(q_1, q_2) = \begin{pmatrix} 2u_1 \delta(q_1) & 0 \\ 0 & 2u_2 \delta(q_2) \end{pmatrix}.$$

Function $E_1(q_1, q_2)$ has minimum for $q_1 = q_2 = 0$, so the effective mass tensor is:

$$\hat{m}_{\text{eff}} = \hbar^2 [\hat{S}(q_1, q_2)]^{-1} |_{q_1=q_2=0}.$$

Using the interpretation of delta-function as being infinite at zero, we get $\hat{m}_{\text{eff}} = \hat{0}$.

The density of states calculation

Here we show how one obtains the density of states (DOS) for FT dispersion, starting from the general definition of DOS. First we define:

$$\varepsilon_+ = |u_1|q_1| + u_2|q_2||,$$

$$\varepsilon_- = |u_1|q_1| - u_2|q_2||.$$

The definition for DOS reads:

$$\begin{aligned}\rho_{\pm}(\varepsilon) &= \frac{1}{4\pi^2} \int_{-\frac{\pi}{a}}^{\frac{\pi}{a}} dq_1 \int_{-\frac{\pi}{b}}^{\frac{\pi}{b}} dq_2 \delta(\varepsilon - \varepsilon_{\pm}(q_1, q_2)) = \\ &= \frac{1}{\pi^2} \int_0^{\frac{\pi}{a}} dq_1 \int_0^{\frac{\pi}{b}} dq_2 \delta(\varepsilon - \varepsilon_{\pm}(q_1, q_2)),\end{aligned}$$

where we have reduced integration to the first quadrant. We introduce the substitution:

$$q_1 = \frac{1}{2u_1}x + \frac{1}{2u_1}y,$$

$$q_2 = \frac{1}{2u_2}x - \frac{1}{2u_2}y,$$

with the corresponding modulus of Jacobian determinant $|J| = \frac{1}{2u_1u_2}$. The range of

integration in new variables becomes:

$$0 \leq x \leq u_1 \frac{\pi}{a} + u_2 \frac{\pi}{b},$$

$$-\frac{\pi u_2}{b} \leq y \leq \frac{\pi u_1}{a}.$$

It follows:

$$\begin{aligned}\rho_+(\varepsilon) &= \frac{1}{2u_1u_2\pi^2} \int_0^{u_1\frac{\pi}{a}+u_2\frac{\pi}{b}} dx \int_{-\frac{a}{\pi u_2}}^{\frac{\pi u_1}{b}} dy \delta(\varepsilon - x) = \\ &= \begin{cases} \frac{1}{2u_1u_2\pi} \left(\frac{u_1}{a} + \frac{u_2}{b} \right); & 0 < \varepsilon < \frac{\pi u_1}{a} + \frac{u_2\pi}{b} \\ \frac{1}{4u_1u_2\pi} \left(\frac{u_1}{a} + \frac{u_2}{b} \right); & \varepsilon = 0 \\ 0; & \varepsilon < 0 \end{cases}\end{aligned}$$

which, after taking in account the particle-hole symmetry for bands $\pm\varepsilon_+$, gives:

$$\rho_1(\varepsilon) = \frac{1}{2u_1u_2\pi} \left(\frac{u_1}{a} + \frac{u_2}{b} \right),$$

for sufficiently small $|\varepsilon|$. Similarly, we get for ε_- :

$$\begin{aligned}\rho_-(\varepsilon) &= \frac{1}{2u_1u_2\pi^2} \int_0^{u_1\frac{\pi}{a}+u_2\frac{\pi}{b}} dx \int_{-\frac{a}{\pi u_2}}^{\frac{\pi u_1}{b}} dy \delta(\varepsilon - |y|) = \\ &= \begin{cases} \frac{1}{u_1u_2\pi} \left(\frac{u_1}{a} + \frac{u_2}{b} \right); & 0 < \varepsilon < \min \left\{ \frac{\pi u_1}{a}, \frac{u_2\pi}{b} \right\} \\ \frac{1}{2u_1u_2\pi} \left(\frac{u_1}{a} + \frac{u_2}{b} \right); & \varepsilon = 0 \\ 0; & \varepsilon < 0 \end{cases}.\end{aligned}$$

Particle-hole symmetry for bands $\pm\varepsilon_-$ implies, for sufficiently small $|\varepsilon|$:

$$\rho_2(\varepsilon) = \frac{1}{u_1u_2\pi} \left(\frac{u_1}{a} + \frac{u_2}{b} \right).$$

After the inclusion of spin degeneracy, and using $u_1 = \hbar v_a$, $u_2 = \hbar v_b$, the total DOS for small $|\varepsilon|$ reads, in terms of Fermi velocities:

$$\rho(\varepsilon) \approx \frac{3}{\pi\hbar} \left(\frac{1}{av_b} + \frac{1}{bv_a} \right).$$

Algorithm used in ab initio search

1. **One chemical element is chosen** from the main groups of the periodic table (IIIA, IVA and VA). Particularly we considered B, C, Si or P.
2. **Setup of initial parameters.** Initial fractional coordinates of a single atom, lattice vectors and one of diperiodic groups, Dg33, Dg43 or Dg45, are chosen. The initial lattice vectors and coordinates are chosen such that bond lengths in the system are as close as possible to typical bond lengths between atoms of a given element. This is done manually. Set up the initial value of variable *current minimal energy* to a large value, i.e. DBL_MAX (predefined value in the C++ language standard). Set up the initial *scaling factors* for lattice vectors. Value of 0.8 was a usual choice.
3. Scale lattice vectors by the current *scaling factors*.
4. Atomic positions of remaining atoms in a unit cell are generated based on Wyckoff equivalent positions for the chosen group.
5. **Screening of possibly stable geometries.** The generated crystal structure (from combination of fractional coordinates and scaled lattice vectors) is checked if it is *likely* stable by analyzing eventual clustering of its atomic positions to disjointed set of clusters. The structure is assumed as unstable and disregarded for further calculations if it has more than 2 disjointed clusters. Two clusters are considered disjointed, if distance between two atoms closest to each other, but belonging to different clusters, is larger or smaller by more than $n \text{ \AA}$ than the sum of their covalent radii. $n = 0.3 \text{ \AA}$ was usually used for most of elements. Larger values of

n up to 0.5 Å are used for carbon, for which it is known to make a larger range of possible bond lengths. This step is done in order to speed up the search of stable structures.

6. **Symmetry-constrained geometry optimization.** If the given structure is not disregarded at the step 5 as an unsuitable initial geometry, a geometry optimization is conducted with constrained diperiodic group, i.e. its corresponding space group. Otherwise, go to the step 9. Density functional theory (DFT)-based software Siesta [S2] is used for calculations of energies and atomic forces during the group-constrained geometry optimization.
7. **Can the symmetry be preserved?** Full unconstrained structural optimization is conducted using the Siesta code. Initial geometry for the optimization is the geometry obtained at the step 6. The optimized geometry is checked for eventual breaking of the symmetry (the diperiodic group, i.e. its corresponding space group) after the full structural optimization. Also check the structural stability of the crystal using the same method described at the step 5.
8. If the symmetry is preserved and the structural stability is confirmed at the step 7, compare total energy with the *current minimal energy*. If it is a smaller one then promote it to the *current minimal energy*, and save atomic coordinates of this structure.
9. Increase scaling factors by 0.02. If they are smaller than 1.2 return to the step 3. Otherwise continue to the step 10.
10. Calculate electronic band structure for the most stable system (*current minimal*) using the Siesta code and analyze the band structure.

All *ab initio* calculations were done using DFT as implemented in the Siesta code [S2]. Space groups from Table 1 were used, which correspond to diperiodic groups, when unit cells were constructed. Lattice vector perpendicular to diperiodic plane was always 15 Å. We utilized the Perdew-Burke-Ernzerhof form of the exchange-correlation functional [S3]. The behavior of valence electrons was described by norm-conserving Troullier-Martins pseudopotential [S4]. We used a double-zeta polarized basis. The mesh cutoff energy of 250 Ry was used, which was sufficient to achieve a total energy convergence of better than 0.1 meV per unit cell during the self-consistency iterations of all calculations. Structures were considered as optimized when maximal force on atoms dropped below 0.04 eV/Å. In the search algorithm a 8 x 8 k-point Monkhorst-Pack mesh in plane of BZ corresponding to the plane of 2D materials was employed and only gamma point was used in the perpendicular direction. A denser k-point mesh of 12 x 12 was used for further optimization and calculation of band structure and density of states of the most stable structures obtained by the search algorithm.

Bands in Fig. 2(b) were obtained on 300 x 300 k-point grid around the corner of BZ (point R).

Molecular dynamics simulation, which confirmed the structural stability of P (Dg45) system, was conducted for 5 ps in 5000 steps of 1fs. Temperature was fixed at 100 K using the Nosé-Hoover thermostat. A super-cell comprising 3 x 3 x 1 repetition of a unit cell containing 36 P atoms was employed in the simulation.

ADDITIONAL REFERENCES



[S1] Wang, J.; Huang, H.; Duan, W.; Liu, Z. Identifying Dirac cones in carbon allotropes with square symmetry *J. Chem. Phys.* 2013, **139**, 184701

[S2] Soler, J. M.; Artacho, E.; Gale, J. D.; Garcia, A.; Junquera, J. P.; Ordejon, P.; Sanchez Portal. The SIESTA method for ab initio order-N materials simulation. *J. Phys. Cond. Mat.* 2002, **14**, 2745-2779.

[S3] Perdew, J. P.; Burke, K.; Ernzerhof, M. Generalized gradient approximation made simple. *Phys. Rev. Lett.* 1996, **77**, 3865-3868.

[S4] Troullier, N.; Martins, J. L. Efficient pseudopotentials for plane-wave calculations. *Phys. Rev. B* 1991, **43**, 1993-2006.

Fully linear band crossings at high symmetry points in layers: classification and role of spin–orbit coupling and time reversal

N Lazić¹ , V Damjanović^{2,*}  and M Damnjanović^{1,3} 

¹ NanoLab, Faculty of Physics, University of Belgrade, Studentski Trg 12, 11001 Belgrade, Serbia

² Institute of Physics Belgrade, University of Belgrade, Pregrevica 118, 11000 Belgrade, Serbia

³ Serbian Academy of Sciences and Arts, Kneza Mihaila St. 35, 11000 Belgrade, Serbia

E-mail: damlja@ipb.ac.rs

Received 22 November 2021, revised 17 June 2022

Accepted for publication 6 July 2022

Published 9 August 2022



CrossMark

Abstract

Symmetry imposed restrictions to the Hamiltonian are systematized and applied to all of 80 clusters of single/double ordinary/gray groups (320 groups in total), to single out linear (in all directions) band crossings and corresponding effective Hamiltonians in high-symmetry Brillouin zone points of layered materials. The resulting dispersion types are isotropic or anisotropic forms of: single cone (with double degenerate crossing point and non-degenerate branches, or four-fold degenerate crossing point with double degenerate conical branches), poppy-flower (four-fold degenerate crossing point with two pairs of non-degenerate mutually rotated conical branches), and fortune teller (with nodal lines). Further, we describe the nontrivial patterns of dispersions' behavior in high symmetry points when symmetry is varied within a cluster. Namely, Clebsch–Gordan series of the products of spin representation with the integer ones are relevant when spin–orbit coupling is included, and clarify observed scenarios (gap closing, gap opening, cone preserving, cone splitting etc). Analogously, analysis of behavior of dispersions in transition from ordinary to gray group enlightens the role of time reversal symmetry. The results refine and expand data existing in literature, and interesting or even unexpected cases are singled out in discussion.

*Author to whom any correspondence should be addressed.

Keywords: two-dimensional materials, Dirac fermions, Weyl fermions, symmetry

(Some figures may appear in colour only in the online journal)

1. Introduction

Interplay between symmetry and topology of band structures is among the most attractive topics in contemporary condensed matter physics. Besides topological insulators (TIs), nodal semimetals take a notable role, being a material realization of relativistic Dirac, Weyl, and Majorana particles [1–3], or lead to the emergence of unconventional quasiparticles [4–7]. Characterized by band crossings (touching) points (lines) at Fermi level, with energies dispersing linearly, they have various interesting properties: Dirac points represent the interphases between topologically different insulating phases, Weyl points lead to semimetals with chiral anomaly, Fermi arc surface states etc. Protected by crystal symmetries [8–16], these crossing points are robust with respect to various symmetry-preserving perturbations. Energy of the crossing cannot be predicted by symmetry alone; particularly important are those on Fermi level: when placed at (special) high symmetry points (HSPs) in Brillouin zone (BZ), the material is known as a symmetry-enforced semimetal.

Leaving accidental degeneracy aside, the band crossings are within group theory related to the multi-dimensional allowed irreducible representations (IRs) of underlying symmetries. Geometrical transformations are gathered into ordinary crystallographic groups. When time reversal (TR) symmetry (either pure for paramagnetic systems, or combined with spatial symmetries for anti/ferromagnets) is included, gray or black-and-white magnetic groups [17, 18] are obtained; these are represented by irreducible corepresentations (coIRs), which have, besides unitary, additional anti-unitary operators. When spin space is included (spinfull case) to consider spin–orbit (SO) interaction, half-integer irreducible (co)representations of double groups are assigned to electron bands.

The raising interest in exploring bands topology [19–21], including its symmetry based aspects, points out the necessity to systematize numerous particular studies, and fill in existing gaps. In particular, layer groups have been intensively used to predict Dirac and beyond-Dirac topological semimetals [11, 14, 22–30], but still there is no complete overview of such symmetry-enforced band structures of layered materials, unlike space groups [31, 32]. Our thorough and systematic presentation will facilitate both numerical and experimental search for the materials with preferred symmetry and desirable band topology, as well as sub-dimensional analysis of 3D crystals [33].

In this paper all band crossings with dispersion equations linear in all BZ directions around HSPs in quasi-2D crystals are singled out, with the corresponding effective low-energy Bloch Hamiltonians. We utilize allowed (co)IRs (calculated by POLSym code [34], and recently made available online [35]) of the symmetry groups of HSPs obtained by the action of layer (LGs), double layer (DLGs), and corresponding gray magnetic groups (gray LGs and gray DLGs) in BZ. It turns out that possible dimensions of (co)IRs, and therefore of the effective Hamiltonian models, are 1, 2, and 4. Among them, two-dimensional ones may correspond to the Hamiltonians with completely linear band crossings hosting non-degenerate conical dispersion (1DC), while four-dimensional (co)IRs support two-degenerate conical (2DC), poppy flower (PF), or fortune teller (FT) shape of energy. The conical and PF dispersions may characterize semimetals, while the presence of FT indicates nodal line metal (where equienergetic lines cross in HSP). In addition, precise usage of (co)IRs (Clebsch–Gordan series, Wigner’s types), enables to consider relations between single and double, or ordinary and gray groups enlightening

the impact of spin–orbit interaction or TR on the dispersions in HSPs. Results on the band crossings patterns (groups, HSPs, types, effects of spin and TR) are tabulated and discussed, stressing out the cases complementing or correcting those in literature.

The paper is structured as follows. Establishing basic concepts and notation, section 2 is a brief review of the group-theoretical apparatus within $\mathbf{k} \cdot \mathbf{p}$ theory. Then in section 3 we single out relevant HSPs in BZ of quasi-2D crystals, model Hamiltonians and the corresponding linear dispersions related to HSPs. Besides this, the robustness of the crossings (whether they are essential or not) is addressed in section 4, analyzing impact of spin and TR.

2. Symmetry of effective Bloch Hamiltonian

Following standard approach, we consider single-particle Hamiltonian H invariant under symmetry group G being one of the four types: ordinary group $G = L$, without TR symmetry θ , is either purely geometrical layer group, or its double extension (to include spin space and SO interaction), while with θ it becomes (single or double) gray layer group $G = L + \theta L$ (for nonmagnetic systems).

On momentum \mathbf{k} from BZ L acts by isogonal point group P_I . In this way LG makes stratification of BZ, singling out generic stratum, and special lines and points, each of them being fixed by characteristic little group (stabilizer) $L_{\mathbf{k}}$ (a subgroup in L) of a representative momentum point \mathbf{k} . Coset representatives h from Lagrange partition $L = \bigcup_h hL_{\mathbf{k}}$ generate star of \mathbf{k} , and the set of representative points of all stars is irreducible domain (ID). Also, due to the trivial action of translations in BZ, all translations are in $L_{\mathbf{k}}$, turning it into a (double) layer group.

While TR symmetry acts trivially on a position vector, it changes the sign of a momentum. Therefore, the addition of TR to the symmetry of layered systems in general changes stratification of the BZ, and three types of stabilizers $G_{\mathbf{k}}$ (as subgroups in $G = L + \theta L$) may occur. For a TR invariant momentum (TRIM) \mathbf{k} the stabilizer is (i) gray group $G_{\mathbf{k}} = L_{\mathbf{k}} + \theta L_{\mathbf{k}}$; otherwise, if \mathbf{k} is not TRIM, $G_{\mathbf{k}}$ is either (ii) black-and-white $G_{\mathbf{k}} = L_{\mathbf{k}} + \theta hL_{\mathbf{k}}$ (if there is a non-identity element h such that $h\mathbf{k} = -\mathbf{k}$), or (iii) ordinary $G_{\mathbf{k}} = L_{\mathbf{k}}$ (either single or double) group. Notably, only in the latest case (iii) the star is doubled due to the TR symmetry, while otherwise it remains the same (cases (i) and (ii)).

Commuting with the translational subgroup, the Hamiltonian reduces into the Bloch spaces. If g belongs to $G_{\mathbf{k}}$, meaning that g stabilizes momentum \mathbf{k} up to the vector of inverse lattice, then

$$[D(g), H(\mathbf{k})] = 0, \quad (1)$$

where $D(G_{\mathbf{k}})$ is representation of stabilizer $G_{\mathbf{k}}$ in the Bloch space and $H(\mathbf{k})$ is the Bloch Hamiltonian. The TR is antilinear operation in the state space, and therefore linear-antilinear representations $D(G_{\mathbf{k}})$ of magnetic little groups are considered: $D(L_{\mathbf{k}}) = d(L_{\mathbf{k}})$ are linear operators, while the other elements are represented by antilinear operators $D(\theta hL_{\mathbf{k}}) = d(\theta hL_{\mathbf{k}})\mathbf{K}$, where $d(\theta hL_{\mathbf{k}})$ are linear factors and \mathbf{K} is the complex conjugation. Only matrix parts $d(L_{\mathbf{k}})$ and $d(\theta h)$ of all elements constitute co-representations. For gray groups, h is the identity element, and $d^2(\theta) = \omega I$, where ω is 1 for spinless, and -1 for spinfull cases (I is identity matrix). Obviously, rewritten in the terms of co-representation for the antilinear coset the relation (1) is $d(g^{-1})H(\mathbf{k})d(g) = H^*(\mathbf{k})$ (for $g \in \theta hL_{\mathbf{k}}$).

Consequently, symmetry provides that the corresponding Bloch Hamiltonian and the stabilizer representation are reduced in $|\alpha|$ -dimensional subspaces, where $|\alpha|$ is the dimension of

the allowed irreducible linear(-antilinear) representation $D^{(k,\alpha)}(G_k)$. Eigenvectors $|\mathbf{k}, \alpha; \mathbf{a}\rangle$ of Bloch Hamiltonian:

$$H(\mathbf{k})|\mathbf{k}, \alpha; \mathbf{a}\rangle = \varepsilon_\alpha(\mathbf{k})|\mathbf{k}, \alpha; \mathbf{a}\rangle, \tag{2}$$

are assigned by quantum numbers (\mathbf{k}, α) of linear(-antilinear) IRs (and allowed representations), meaning [36] that:

$$D(g)|\mathbf{k}, \alpha; \mathbf{a}\rangle = \sum_{\mathbf{a}'} D_{\mathbf{a}'\mathbf{a}}^{(k,\alpha)}(g)|\mathbf{k}, \alpha; \mathbf{a}'\rangle. \tag{3}$$

Expansion of the Bloch Hamiltonian in the vicinity of HSP \mathbf{k}_0 is

$$H(\mathbf{k}_0 + \mathbf{k}) = \sum_{n \geq 0} H^{(n)}(\mathbf{k}_0 + \mathbf{k}),$$

$$H^{(n)}(\mathbf{k}_0 + \mathbf{k}) = \frac{1}{n!} \sum_{p_1, \dots, p_n} \frac{\partial^n H(\mathbf{k}_0)}{\partial k_{p_1} \dots \partial k_{p_n}} k_{p_1} \dots k_{p_n}, \tag{4}$$

where $p_i = 1, 2$. Gathering terms with $n > 0$ within perturbation $H'(\mathbf{k}_0 + \mathbf{k})$, an effective Hamiltonian is obtained with help of projector $P_\alpha = \sum_{\mathbf{a}=1}^{|\alpha|} |\mathbf{k}_0, \alpha; \mathbf{a}\rangle \langle \mathbf{k}_0, \alpha; \mathbf{a}|$ composed of the eigenvectors of unperturbed Hamiltonian $H^{(0)}(\mathbf{k}_0) = H(\mathbf{k}_0)$ (matrix with zero order term $n = 0$). In the first perturbation order, the effective Hamiltonian is $H'_\alpha(\mathbf{k}) = P_\alpha H'(\mathbf{k}) P_\alpha$, and the symmetry conditions (1) for each effective term $H_\alpha^{(n)}$ of the expansion (4) becomes:

$$D^{(k_0,\alpha)}(g)H_\alpha^{(n)}(\mathbf{k}_0 + \mathbf{k})D^{(k_0,\alpha)}(g^{-1}) = H_\alpha^{(n)}(\mathbf{k}_0 + g\mathbf{k}). \tag{5}$$

As before, depending on the type of a considered system, $D^{(k,\alpha)} = d^{(k,\alpha)}$ is a unitary integer (spinless) or a half-integer (spinfull) IR of a (double) layer group, or, a linear-antilinear representation composed of the unitary matrix of coIR $d^{(k,\alpha)}$ (multiplied by operator of complex-conjugation on the coset accompanied by TR) for a magnetic little group. In all these cases of layer groups the dimensions of IRs are 1, 2 or 4.

Stabilizer $G_{\mathbf{k}_0+\mathbf{k}}$ of a representative momentum $\mathbf{k}_0 + \mathbf{k}$ from the generic stratum (dense in BZ) is a subgroup of $G_{\mathbf{k}_0}$, and the subduced (co)representation obeys compatibility relations

$$d^{(k_0,\alpha)}(G_{\mathbf{k}_0}) \downarrow G_{\mathbf{k}_0+\mathbf{k}} = \oplus_i f_i d^{(k_0+\mathbf{k},\alpha_i)}(G_{\mathbf{k}_0+\mathbf{k}}), \tag{6}$$

where f_i is frequency number of the irreducible component $d^{(k_0+\mathbf{k},\alpha_i)}$. For the elements of $G_{\mathbf{k}_0+\mathbf{k}}$ the symmetry condition (5) becomes commutation causing that the energy branches in the vicinity of \mathbf{k}_0 have degeneracies (1 or 2) of (co)representations $d^{(k_0+\mathbf{k},\alpha_i)}(G_{\mathbf{k}_0+\mathbf{k}})$, while the degeneracy of the energy at crossing point \mathbf{k}_0 coincides with the dimension (2 or 4) of (co)representation $d^{(k_0,\alpha)}(G_{\mathbf{k}_0})$.

3. Linear dispersions

3.1. Effective Hamiltonian

At first, the forms of the effective Hamiltonians having completely linear dispersions in BZ around HSPs will be derived. According to (4), the matrix elements of the effective low-energy Hamiltonian linear ($n = 1$) in momentum are $[H_\alpha^{(1)}(\mathbf{k}_0 + \mathbf{k})]_{ab} = \sum_p w_{ab}^p k_p$, where parameters

$w_{ab}^p = \partial[H_\alpha(\mathbf{k}_0)]_{ab}/\partial k_p$ are constrained by symmetry conditions (5) and hermiticity ($w_{ab}^p = w_{ba}^{p*}$). The conditions (5) can be rewritten in the super-operator form as:

$$\left[d^{(\mathbf{k}_0, \alpha)}(g) \otimes d^{(\mathbf{k}_0, \alpha)*}(g) \otimes v(g) \right] w = w, \quad \text{for } g \in L_{k_0} \quad (7)$$

$$\left[d^{(\mathbf{k}_0, \alpha)}(g) \otimes d^{(\mathbf{k}_0, \alpha)*}(g) \otimes I_2 \right] w^* = w, \quad \text{for } g = \theta h, \quad (8)$$

where w is a column of parameters w_{ab}^p , which is looked for. The group action in 2D BZ is introduced by usual two-dimensional polar-vector representation $v(L_{k_0})$ of subgroup, and $v(\theta h) = I_2$. Since a linear effective Hamiltonian is bi-uniquely related to a non-vanishing column w , from (7) it follows that w is a fixed point for subgroup representation $d^{(\mathbf{k}_0, \alpha)} \otimes d^{(\mathbf{k}_0, \alpha)*} \otimes v$, i.e. linear terms exist if [21] vector representation $v(L_{k_0})$ appears in $d^{(\mathbf{k}_0, \alpha)} \otimes d^{(\mathbf{k}_0, \alpha)*}(L_{k_0})$; for magnetic groups there is additional condition (8) for the antiunitary coset.

Linearly independent columns $w_{ab} = (w_{ab}^1, w_{ab}^2)^T$ define *linearity rank*: number of BZ directions along which energies are linear in \mathbf{k} . Obviously, completely linear dispersions have linearity rank 2. Since it is beyond the scope of the paper, herein the details about the dispersions are not studied, we only note in section 4 which groups have linearity rank 1 (the vanishing linear term could be either nodal line when all higher order terms cancel, or of higher order dispersion). Linearity rank 0 refers to Hamiltonians without linear terms.

Instead of using absolute basis and parameters w_{ab}^p , it is more convenient to give the effective Hamiltonians in the basis of Hermitian matrices. With Pauli matrices σ_i ($i = 1, 2, 3$) and identity matrix $\sigma_0 = I_2$, the effective 2D and 4D Hamiltonians (1D does not yield band crossing) are:

$$H_2 = \sum_{i=0}^3 \sum_{p=1}^2 v_i^p k_p \sigma_i, \quad (9)$$

$$H_4 = \sum_{i,j=0}^3 \sum_{p=1}^2 v_{ij}^p k_p (\sigma_i \otimes \sigma_j). \quad (10)$$

Clearly, real parameters v_i^p and v_{ij}^p are bi-uniquely related to w_i^p and w_{ij}^p , respectively. For each HSP and its allowed (co)IRs [35] of dimension 2 and 4, the symmetry allowed parameters v_i^p and v_{ij}^p are to be found. The task is performed assuming that layer is perpendicular to the z -axis. All calculations follow notation from [34, 35] (labels of HSPs, IDs), including (co)IRs.

Orthogonal part of any Euclidean transformation from arbitrary layer group leaves both the xy -plane and the z -axis invariant, having thus block-diagonal $2 \times 2 + 1 \times 1$ form. Action in 2D BZ is defined by the upper block. As a result, there is 10 different isogonal groups [35] composed of these 2×2 matrices, which, due to torus topology, yield 14 IDs of 2D BZ. IDs are the same for LG and DLG, while adding TR changes ID of noncentrosymmetric groups. Ordinals of the IDs are associated to the ordinary (gray) groups in the row ID (ID') in figure 2.

There are seven special points (figure 1): $\Gamma = (0, 0)$, $X = (1/2, 0)$, $Y = (0, 1/2)$, $S = (1/2, 1/2)$, $M = (1/2, 0)$, $K = (1/3, 1/3)$ and $L = (2/3, -1/3)$, with coordinates given in primitive basis $\{\mathbf{b}_1, \mathbf{b}_2\}$. They are distributed over 10 IDs: ID1 and ID3-ID5 have no HSPs; ID2 and ID8 have Γ , X , Y , and S ; ID9 has Γ , Y , and S ; ID7 and ID13 have Γ , X , and S ; ID6 and ID12 have Γ , K , and L ; ID10 and ID14 have Γ , M , and K ; ID11 has Γ and K . For oblique and rectangular-p groups with all non-symmorphic elements having fractional translations parallel

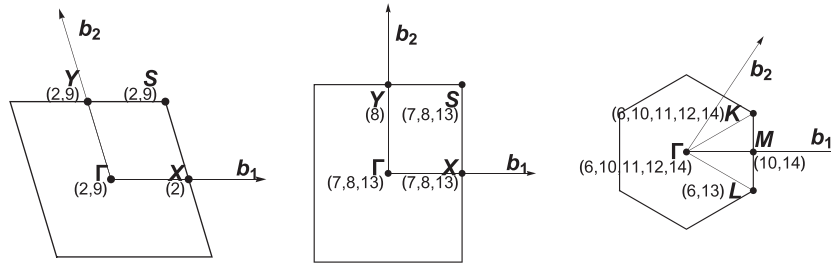


Figure 1. HSPs. Each point is shown only in ID (equivalent copies from BZ are missing). Ordinals of IDs [35] are listed in brackets; IDs are associated to groups in figure 2. Left panel: oblique and c-centered rectangular ($|b_1| = |b_2|$) groups; middle panel: rectangular-p and square ($|b_1| = |b_2|$) groups; right panel: hexagonal groups.

to one direction (for group 45), b_1 is perpendicular to that direction (to the symmorphic reflection plane). For group 34 (32, 33, 43) b_1 is along axis (screw axis) of order two. This notation differs from [37] in the following way (notation in brackets corresponds to [37]): for oblique groups $X(Y)$, $Y(B)$, $S(A)$; for rectangular-c $Y(S)$, $S(Y)$; for square $Y(X)$, $S(M)$; for rectangular-p groups 8, 11, 12, 16, 17, 20, 24, 31, 32, 33, 34, 38, 40, 41, 43, 45 $X(Y)$, $Y(X)$. For other cases the two notations are the same.

All of the HSPs are TRIM except K and L . Therefore, the stabilizer of Γ , X , Y , S , M is a gray group, while for K it is either a black-and-white (in hexagonal gray LGs: 66, 67, 69, 71–73, 75–78, 80) or an ordinary group (in the hexagonal gray LGs: 65, 68, 70, 74, 79). Stabilizers of L are ordinary, as it is the HSP only in ordinary groups (68, 70 and 79). In the most of the cases the stabilizer is the whole group, exceptions are points Y in ID9, K in ID11 and ID14, and X in ID13 where it is a halving subgroup, and point M in ID14 where the stabilizer is index-three subgroup.

Altogether we found 42 different effective Hamiltonians with completely linear dispersions at HSPs: 21 for 2D and 21 for 4D Hamiltonians are presented in tables 1 and 2. Number of nonzero coefficients v_i^p and v_{ij}^p may be 6, 4, 3, 2 or 1, as emphasized; the other vanish due to the symmetry. In particular, this includes those responsible for slope, which manifests that neither of the dispersions is tilted.

The results for all of 80 layer group clusters are summarized in figure 2. All HSPs hosting linearity rank 2 dispersions are listed, once for each of the associated allowed representations assigning/supporting such dispersions, with indicated effective model (subscript). The list of linear dispersions systematized in this way may be used for various analyzes, and in the following sections some of them will be performed.

3.2. Dispersion types

Band crossings of the presented Hamiltonian models have linearity rank 2 with conical, PF (both can be realized in isotropic or anisotropic forms) or FT shape of dispersion. A conical dispersion corresponds to compatibility relations (6) with dimensions $2 \rightarrow 1 \oplus 1$ (1DC), or $4 \rightarrow 2 \oplus 2$ (2DC), while the both PF and FT are related to splitting dimensions $4 \rightarrow 1 \oplus 1 \oplus 1 \oplus 1$. The cases with 1DC and 2DC are usually referred to as Weyl and Dirac fermions respectively. PF consists of two mutually rotated non-degenerate anisotropic cones (some authors consider PF as generalized Dirac dispersion [25, 39]), while FT is composed of locally flat bands, with equienergetic nodal lines.

Table 1. Two-dimensional effective Hamiltonian forms. Non-vanishing symmetry adapted parameters v_i^p in (9) are defined in terms of independent constants c_i (obtaining values in concrete problems). Symbol in column S is used in figure 2 to identify model, while the number of the independent parameters, and corresponding dispersion equation are in columns Par. and equation; all energy branches are non-degenerate. Two coefficients v_0^1 and v_0^2 , vanishing in all models, are omitted.

S	v_1^1	v_2^1	v_3^1	v_1^2	v_2^2	v_3^2	Par.	Equation
a	0	0	c_1	0	c_2	0	2	(11b)
b	0	0	c_1	c_2	0	0	2	(11b)
c	0	0	c_1	c_2	c_3	0	3	(11b)
d	0	$-c_1$	0	c_1	0	0	1	(11c)
e	0	c_1	0	c_1	0	0	1	(11c)
f	0	c_2	0	0	0	c_1	2	(11b)
g	0	c_2	0	c_1	0	0	2	(11b)
h	c_1	0	0	0	c_1	0	1	(11c)
i	c_1	0	0	0	c_2	0	2	(11b)
j	c_1	$-c_1$	0	$-c_1$	$-c_1$	0	1	(11c)
k	c_1	c_1	0	$-c_1$	c_1	0	1	(11c)
l	$\sqrt{3}c_1$	$-c_1$	0	c_1	$\sqrt{3}c_1$	0	1	(11c)
m	c_1	$-\sqrt{3}c_1$	0	$-\sqrt{3}c_1$	$-c_1$	0	1	(11c)
n	$\sqrt{3}c_1$	$-\sqrt{3}c_2$	0	c_1	$3c_2$	0	2	(11a)
o	c_1	$-c_2$	0	c_2	c_1	0	2	(11c)
p	c_1	c_2	0	c_2	$-c_1$	0	2	(11c)
q	c_1	c_3	0	c_2	c_4	0	4	(11a)
r	c_2	c_3	0	0	0	c_1	3	(11b)
s	$\sqrt{3}c_2$	$\sqrt{3}c_3$	$\sqrt{3}c_1$	c_2	c_3	$-3c_1$	3	(11a)
t	$\sqrt{3}c_2$	$-\sqrt{3}c_3$	$\sqrt{3}c_1$	$-3c_2$	$3c_3$	c_1	3	(11a)
u	c_3	c_5	c_1	c_4	c_6	c_2	6	(11a)

For completeness, a brief overview of all types of dispersions (of linearity rank 2) are given, despite some of them have been already studied [11, 23, 24, 28, 29]. For each model (row of the tables 1 and 2) the Hamiltonian matrix is formed according to (9) or (10) with non-vanishing v_i^p and v_{ij}^p ; it is expressed in terms of independent coefficients c_1, \dots, c_6 (given in the row). As eigenvalues of these \mathbf{k} -dependent matrices, the obtained dispersions are parametrized by coefficients c_i . For example $c_1(\sqrt{3}k_1 + k_2)\sigma_1 - c_2(\sqrt{3}k_1 - 3k_2)\sigma_2$ is the matrix for the two dimensional Hamiltonian in 14th row in table 1 (symbol n).

General anisotropic IDC dispersion is

$$\varepsilon_{\pm}(k_1, k_2) = \pm \sqrt{ak_1^2 + bk_1k_2 + ck_2^2}, \quad (11a)$$

where a, b, c are c_i -related parameters with ranges providing real energies. Equienergetic curves on this cone are ellipses with semi-axes a' and c' ($\frac{a}{\varepsilon^2} = \frac{\cos^2 \varphi}{a'^2} + \frac{\sin^2 \varphi}{c'^2}$, $\frac{c}{\varepsilon^2} = \frac{\sin^2 \varphi}{a'^2} + \frac{\cos^2 \varphi}{c'^2}$, $\frac{b}{\varepsilon^2} = 2 \cos \varphi \sin \varphi \left(\frac{1}{a'^2} - \frac{1}{c'^2} \right)$), which are rotated with respect to the k_1k_2 -coordinate system for the angle φ between axes a' and k_1 . To illustrate, the Hamiltonian n (table 1) from the above example has dispersion (11a), with $a = 3(c_1^2 + c_2^2)$, $b = \sqrt{12}(c_1^2 - 3c_2^2)$ and $c = c_1^2 + 9c_2^2$. For $b = 0$ the dispersion is still an anisotropic IDC (but not rotated)

$$\varepsilon_{\pm}(k_1, k_2) = \pm \sqrt{ak_1^2 + ck_2^2}, \quad (11b)$$

Table 2. Four-dimensional effective Hamiltonian forms. Non-vanishing symmetry adapted parameters v_{ij}^p in (10) are defined in terms of independent constants c_i (obtaining values in concrete problems). Symbol in column S is used in figure 2 to identify model, while the number of the independent parameters, corresponding dispersion equation, and the degeneracy of the branches are in columns Par, equation, and Deg. Ten coefficients $v_{00}^1, v_{01}^1, v_{03}^1, v_{32}^1, v_{00}^2, v_{01}^2, v_{03}^2, v_{12}^2, v_{22}^2$ and v_{32}^2 , vanishing in all models, are omitted.

S	v_{02}^1	v_{10}^1	v_{11}^1	v_{12}^1	v_{13}^1	v_{20}^1	v_{21}^1	v_{22}^1	v_{23}^1	v_{30}^1	v_{31}^1	v_{33}^1	v_{02}^2	v_{10}^2	v_{11}^2	v_{13}^2	v_{20}^2	v_{21}^2	v_{23}^2	v_{30}^2	v_{31}^2	v_{33}^2	Par.	Equation	Deg.
A	0	0	0	0	0	0	0	0	0	0	0	c_1	0	0	0	c_2	0	0	c_3	0	0	0	3	(11b)	2
B	0	0	0	0	0	0	0	0	0	0	0	c_1	0	c_2	0	0	c_3	0	0	0	0	0	3	(11b)	2
C	0	0	0	0	0	0	0	0	0	0	0	c_1	0	c_3	0	0	c_4	0	0	0	c_2	0	4	(11b)	2
D	0	0	0	0	0	0	0	0	0	0	c_1	0	0	c_2	0	0	c_3	0	0	0	0	0	3	(11b)	2
E	0	0	0	0	0	$-c_1$	0	0	0	0	0	0	0	0	0	0	0	0	0	0	0	0	1	(11c)	2
F	0	0	0	0	0	$-\frac{c_1+c_2}{2}$	0	0	$\frac{c_1-c_2}{2}$	0	0	0	0	$\frac{c_1+c_2}{2}$	0	$\frac{c_1-c_2}{2}$	0	0	0	0	0	0	2	(12d)	1
G	0	0	0	0	c_2	0	0	0	$-c_3$	0	0	0	0	0	0	0	0	0	0	0	0	c_1	3	(11b)	2
H	0	0	0	0	c_2	0	0	0	c_4	0	0	c_1	c_3	0	0	0	0	0	0	0	0	0	4	(11b)	2
I	0	0	0	0	c_3	0	0	0	c_5	0	0	c_1	0	0	c_4	0	0	c_6	0	0	c_2	0	6	(12a)	1
J	0	0	0	c_3	0	0	0	c_1	0	0	0	0	c_2	0	0	0	0	0	0	0	0	0	3	(12c)	1
K	0	0	0	c_4	0	0	0	c_2	0	c_1	0	0	c_3	0	0	0	0	0	0	0	0	0	4	(12c)	1
L	0	0	c_4	0	0	0	c_6	0	0	0	c_2	0	0	c_3	0	0	c_5	0	0	c_1	0	0	6	(12a)	1
M	0	c_1	0	0	0	$-c_2$	0	0	0	0	0	0	0	c_2	0	0	c_1	0	0	0	0	0	2	(11c)	2
N	0	c_2	0	0	0	c_3	0	0	0	0	0	0	0	0	0	0	0	0	0	0	c_1	0	3	(11b)	2
O	0	c_2	0	0	0	c_4	0	0	0	c_1	0	0	c_3	0	0	0	0	0	0	0	0	0	4	(12c)	1
P	0	c_3	0	0	0	c_5	0	0	0	0	c_1	0	0	c_4	0	0	c_6	0	0	0	c_2	0	6	(11a)	2
Q	0	c_3	0	0	0	c_5	0	0	0	c_1	0	0	0	0	0	c_4	0	0	c_6	0	0	c_2	6	(12a)	1
R	c_1	c_2	0	0	c_3	$-c_3$	0	0	c_2	0	c_1	0	c_1	c_2	0	$-c_3$	$-c_3$	0	$-c_2$	0	$-c_1$	0	3	(12b)	1
S	c_2	0	0	0	0	0	0	0	0	0	0	0	0	0	0	0	0	0	0	0	c_1	0	2	(11b)	2
T	c_3	0	0	0	0	0	0	0	0	0	0	0	0	0	0	c_2	0	0	c_4	0	0	c_1	4	(11b)	2
U	c_3	0	0	0	0	0	0	0	0	0	0	0	0	c_2	0	0	c_4	0	0	c_1	0	0	4	(12c)	1

	Gray DLG	DLG	LG	C	ID	ID'	P _I	H
Gray LG								
DLG								
LG								
C								
ID								
ID'								
P _I								
H	C_{2h} Oblique	D_{2h} Rectangular	D_{4h} Square	D_{6h} Hexagonal				

Figure 2. HSPs (see figure 1) hosting completely linear dispersions obtained by action of LG, DLG, and their gray extensions in 2D BZ for each cluster C; ordinals are according to [38]. Dimensions of the allowed (co)IRs are distinguished by colors: blue stands for 2D, while green corresponds to 4D (co)IRs. The subscript is the label of the Hamiltonian model in tables 1 and 2. The superscripts correspond to the labels of SO transitions from the tables 3 and 4. Also, the first column H is holoedry (with lattice type) and isogonal groups P_I are given in the second one. Those groups with inversion symmetry included are orange colored, while non-symmorphic groups are singled out by red in column C. In the column ID and ID' are ordinals of IDs of (gray) LGs according to [35].

which isohypses are ellipses with semi-axes ε/\sqrt{a} and ε/\sqrt{c} . Finally, *isotropic IDC* is obtained by $a = c$:

$$\varepsilon_{\pm}(k_1, k_2) = \pm a|\mathbf{k}|. \quad (11c)$$

As for 4D, *general anisotropic PF* dispersion [29] is:

$$\varepsilon_{\pm,u}(k_1, k_2) = \pm \sqrt{ak_1^2 + ub|k_1k_2| + ck_2^2}, \quad u = \pm 1. \quad (12a)$$

Substituting $a = c$ the *isotropic PF* is obtained:

$$\varepsilon_{\pm,u}(k_1, k_2) = \pm \sqrt{ak^2 + ub|k_1k_2|}, \quad u = \pm 1, \quad (12b)$$

while (12a) for $b^2 = 4ac$ becomes nodal line *FT dispersion* [28]:

$$\varepsilon_{\pm,u}(k_1, k_2) = \pm |\sqrt{a}|k_1| + u\sqrt{c}|k_2||, \quad u = \pm 1. \quad (12c)$$

Effective model Hamiltonian F from table 2 describes also isotropic PF but slightly modified:

$$\varepsilon_{\pm,u}(k_1, k_2) = \pm \sqrt{\frac{(c_1^2 + c_2^2)(k_1^2 + k_2^2) + u|c_1^2 - c_2^2||k_1^2 - k_2^2|}{2}}, \quad u = \pm 1; \quad (12d)$$

substitution $k_1 \pm k_2 \rightarrow k_{\pm}$ reduces it to the form (12b). Here, positive $\varepsilon_{+,u}$ (as well as negative $\varepsilon_{-,u}$) branches are touched along the lines $k_1 = \pm k_2$. The rest of the 4D Hamiltonians result in 2DC (double degenerate cones described by equations discussed in 2D case). All dispersions are given in figure 3.

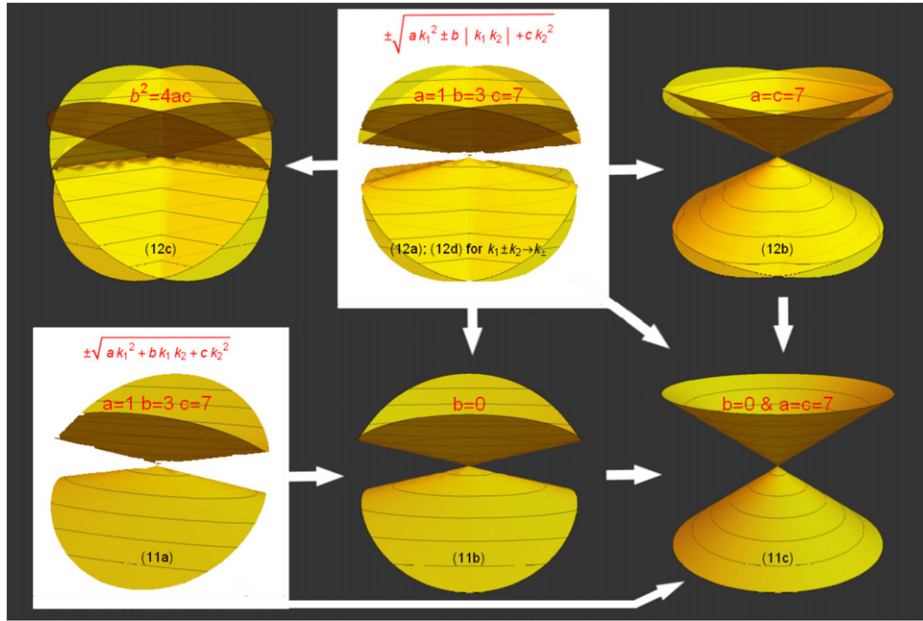


Figure 3. Fully linear dispersions in the vicinity of HSPs in quasi-2D systems. For each type the equation number is given; the value of parameters are set to $a = 1, b = 3, c = 7$, unless it is specified otherwise. All the cases can be obtained from the two most general marked cases; this is denoted by the arrows.

4. Analysis

Having at disposal all possible completely linear dispersions in the HSPs of layered systems, we analyze their interrelations. In this context the roles of SO coupling and TR symmetry are examined. In the group-theoretical language inclusion of spin can be seen as transition from single to double group, while TR relates ordinary and gray group.

4.1. Spin-orbit interaction

SO interaction is taken into account through the relation between integer and half-integer representations. Total space is tensor product of the orbital space with two-dimensional spin-half space, the later carrying spin representation $u(G_{k_0}) \in SU(2)$. Since composed of $SU(2)$ matrices, u can be either irreducible or reducible $u = u_1 \oplus u_2$ (u_i are irreducible). Hence, each integer irreducible (allowed) co-representation $d^{(k_0, \alpha)}(G_{k_0})$ is multiplied by $u(G_{k_0})$, yielding a half-integer representation, either irreducible itself $d^{(k_0, \tilde{\alpha})}(G_{k_0})$ (with frequency number $f^{\tilde{\alpha}} = 1$ in the decomposition below), or decomposed onto irreducible components (associated to k_0 and counted by $\tilde{\alpha}$):

$$d^{(k_0, \alpha)}(G_{k_0}) \otimes u(G_{k_0}) = \oplus_{\tilde{\alpha}} f^{\tilde{\alpha}} d^{(k_0, \tilde{\alpha})}(G_{k_0}). \tag{13}$$

However, not all completely linear band crossings remain such when spin space is added. Besides (13), this depends also on compatibility relation (6) between HSP and generic point stabilizer (co)IRs. Namely, the tensor product of the both sides of (6) by the spin representation

u can be found: obvious rule $u(G_{k_0} \downarrow G_{k_0+k}) = u(G_{k_0+k})$ gives $(d^{(k_0,\alpha)}(G_{k_0}) \otimes u(G_{k_0})) \downarrow G_{k_0+k} = \oplus_i f_i(d^{(k_0+k,\alpha_i)}(G_{k_0+k}) \otimes u(G_{k_0+k}))$. Then right and left sides are reduced in Clebsch–Gordan series.

As an illustration of mechanism how band splitting (the degeneracy of branches around a crossing point) is changed after the SO inclusion, let us consider the u -reducible case. The components u_j ($j = 1, 2$) are one-dimensional, and remain irreducible when subduced onto generic domain. Clearly, following the relation (13), each integer (orbital) (co)IR is decomposed onto two half-integer (co)IRs $d^{(k_0,\tilde{\alpha}_j)}(G_{k_0})$ of the same dimension, equivalent to $d^{(k_0,\alpha)}(G_{k_0}) \otimes u_j(G_{k_0})$, giving essentially two independent energies. Applying further the compatibility relation leads to $(d^{(k_0,\alpha)}(G_{k_0}) \otimes u_j(G_{k_0})) \downarrow G_{k_0+k} = \sum_i f_i^j(d^{(k_0+k,\alpha_i)}(G_{k_0+k}) \otimes u_j(G_{k_0+k}))$, which determines the degeneracy of branches around HSP for each group of bands counted by j when SO is considered.

We calculated the decompositions (13) for the both cases without and with TR symmetry. Results with crossing bands are presented in the table 3 for ordinary groups and table 4 for gray groups, together with linearity rank. Extracting the data from these tables, i.e. analyzing (13) for all possible dimensions (1, 2, and 4) of (co)IRs, different ways how SO may affect band crossings are listed below, where notation $|\alpha| \xrightarrow{\text{SO}} \oplus_{\tilde{\alpha}} |\tilde{\alpha}|$ is used to explicate the dimensions of the allowed representations in spinless and spinful cases. Non-crossing cases correspond to linearity rank 0.

- $1 \xrightarrow{\text{SO}} 2$. SO induces transition from an orbital nondegenerate band (no crossing) to a band crossing, with one of the following dispersions:
 - (α) 1DC;
 - (β) Linearity rank 1.
- $2 \xrightarrow{\text{SO}} 4$. Transitions from 2D integer (co)IR are:
 - (γ) A two-fold orbital band (no crossing) becomes four-degenerate point with (modified) PF or 2DC;
 - (δ) 2D crossing point of linearity rank 1 yields four-degenerate band crossing with PF, FT or 2DC;
 - (ϵ) 2D crossing point of linearity rank 1 becomes 4D crossing with linearity rank 1.
- $2 \xrightarrow{\text{SO}} 2 \oplus 2$. When 2D integer (co)IR produces two 2D half-integer (co)IRs, possible patterns are:
 - (ζ) Single two-fold orbital band (no crossing) yields two 1DC (differing in energy);
 - (η) Single two-fold orbital band (no crossing) becomes a 1DC and a two-fold band (without crossing);
 - (θ) Single two-fold orbital band (no crossing) gives two two-degenerate crossings of linearity rank 1;
 - (ι) Two-degenerate point of linearity rank 1 gives two 1DC;
 - (κ) Two-degenerate point of linearity rank 1 gives two two-degenerate linearity rank 1 crossings;
 - (λ) Spinless 1DC yields two 1DC;
 - (μ) Spinless 1DC transforms into two two-fold band (gap opening pattern).
- $2 \xrightarrow{\text{SO}} 2 \oplus 1 \oplus 1$. Transition from a spinless 1DC crossing to:
 - (ν) 1DC and two non-degenerate bands (cone preserving).

Table 3. Influence of SO coupling to the type of the splitting without TR symmetry: each row denotes a particular type (label in the column T is used as superscript in figure 2) of transition from spinless case (described s by degeneracy $|\alpha|$ at the crossing point and linearity rank L_α) to the spinfull case (characterized by frequency $f^{\tilde{\alpha}}$ in decomposition (13), crossing point degeneracy $|\tilde{\alpha}|$, and linearity rank $L_{\tilde{\alpha}}$). In the last column are corresponding groups with hosting HSPs (also specified in figure 2).

T	$ \alpha $	L_α	$f^{\tilde{\alpha}}$	$ \tilde{\alpha} $	$L_{\tilde{\alpha}}$..., Group HSP ₁ HSP ₂ ..., ...
α	1	0	1	2	2	19SXY Γ , 20X Γ , 21S Γ , 22S Γ , 23SXY Γ , 24X Γ , 25S Γ , 26S Γ , 53SXT, 54S Γ , 55SXT, 57SXT, 58S Γ , 59SXT, 60S Γ , 67 Γ , 68KLG, 69 Γ , 70KLG, 71K 72K, 76KMT, 77KMT 56S Γ
γ	2	0	1	4	2	62S, 64S
ζ	2	0	1	2	2	39S, 46S, 53S Γ , 54S Γ , 55S Γ , 56S Γ , 57S Γ , 58S Γ , 59S Γ , 60S Γ
η	2	0	1	2	0	76 Γ , 77 Γ
	2	1	2	2	1	7S, 7Y, 48Y, 52X
κ	2	1	1	2	1	38SY, 39XY, 41SY, 42XY 43SY, 45SY, 46XY, 62X, 64X
λ	2	2	2	2	2	15SY, 16SY, 17XY
μ	2	2	1	2	0	40SY, 43X, 44XY, 45X, 63X, 78 Γ , 79KLG, 80K
			1	1	0	
ν	2	2	1	1	0	67 Γ , 68KLG, 69 Γ , 70KLG, 71K, 72K, 76K, 77K
			1	2	2	
			1	1	0	
ξ	2	2	1	1	0	20SY, 21XY, 24SY, 25XY, 54X, 56X, 58X, 60X
			1	1	0	

- $2 \xrightarrow{SO} 1 \oplus 1 \oplus 1$: another gap opening pattern, where a spinless 1DC splits into (ξ) Four non-degenerate bands (no crossing).
- $4 \xrightarrow{SO} 4 \oplus 4$: one way to split spinless FT dispersion (4D allowed integer representation) is to (o) Two four-fold crossings of the linearity rank 1.
- $4 \xrightarrow{SO} 2 \oplus 2 \oplus 2$: also, spinless FT dispersion may be transformed into (π) Four 2D crossings of linearity rank 1.

Table 4. Influence of SO coupling to the type of the splitting with TR symmetry: each row is a particular type (label in the column T is used as superscript in figure 2) of transition from spinless case (described by degeneracy $|\alpha|$ at the crossing point, linearity rank L_α , and a number W_α of the subgroup IR) to the spinfull case (characterized by frequency $f^{\tilde{\alpha}}$ in decomposition (13), crossing point degeneracy $|\tilde{\alpha}|$, linearity rank $L_{\tilde{\alpha}}$ and Wigner’s kind of subgroup IR $W_{\tilde{\alpha}}$). In the last column are corresponding groups with hosting HSPs (also specified in figure 2).

T	$ \alpha $	L_α	W_α	$f^{\tilde{\alpha}}$	$ \tilde{\alpha} $	$L_{\tilde{\alpha}}$	$W_{\tilde{\alpha}}$..., Group HSP ₁ HSP ₂ ..., ...
α	1	0	1	1	2	2	-1	1SXY Γ , 10Y, 13Y, 65M
α	1	0	1	1	2	2	0	3SXY Γ , 8SXY Γ , 9X Γ , 10S Γ , 11SXY Γ , 12X Γ , 13S Γ , 22Y, 26Y, 49SXY Γ , 50SXY Γ , 65 Γ , 67M, 68M, 69M, 70M, 73KM Γ
α	1	0	1	1	2	2	1	19SXY Γ , 20X Γ , 21 Γ , 22S Γ , 23SXY Γ , 24X Γ , 25 Γ , 26S Γ , 53SXY Γ , 54 Γ , 55SXY Γ , 56 Γ , 58 Γ , 59SXY Γ , 60 Γ , 67 Γ , 68K Γ , 69 Γ , 70K Γ , 76KM Γ , 77KM Γ , 57SXY Γ
β	1	0	1	1	2	1	0	4SXY Γ , 5X Γ , 35Y, 74M
β	1	0	1	1	2	1	1	27SXY Γ , 28X Γ , 29X Γ , 30X Γ , 31X Γ , 32 Γ , 33 Γ , 34 Γ , 35S Γ , 36S Γ , 78M 79M
γ	2	0	0	1	4	2	-1	21S, 25S
γ	2	0	0	1	4	2	0	54S, 56S, 58S, 60S
γ	2	0	1	1	4	2	0	39S, 46S, 52S, 54S, 56S, 58S, 60S
γ	2	0	1	1	4	2	1	62S, 64S
δ	2	1	0	1	4	2	-1	28SY, 29SY, 30SY, 32X, 33X, 34X
δ	2	1	1	1	4	2	-1	7SY, 15SY, 16SY, 17XY, 48Y, 52X
δ	2	1	1	1	4	2	0	38SY, 39XY, 41SY, 42XY, 43Y, 45Y, 46XY, 62X, 64X
ϵ	2	1	1	1	4	1	0	40SY, 43X, 44XY, 45X, 63X
ζ	2	0	0	1	2	2	0	49S Γ , 50S Γ
ζ	2	0	1	1	2	2	1	53S Γ , 54 Γ , 55S Γ , 56 Γ , 57S Γ , 58 Γ , 59S Γ , 60 Γ
η	2	0	0	1	2	0	-1	65 Γ
η	2	0	0	1	2	0	0	73 Γ

(continued on next page)

Table 4. Continued.

T	$ \alpha\rangle$	L_α	W_α	$f^{\tilde{\alpha}}$	$ \tilde{\alpha}\rangle$	$L_{\tilde{\alpha}}$	$W_{\tilde{\alpha}}$..., Group HSP ₁ HSP ₂ ..., ...
η	2	0	1		1 2 0 0 1 2 2 1			67 Γ , 68 Γ , 69 Γ , 70 Γ
η	2	0	1		1 2 0 1 1 2 2 1			76 Γ , 77 Γ
θ	2	0	1		1 2 1 0 1 2 1 0			32 S , 34 S
ι	2	1	0		1 2 2 -1 1 2 2 -1			5 SY , 36 Y
ι	2	1	1		1 2 2 0 1 2 2 0			31 SY , 32 Y , 33 Y , 34 Y
κ	2	1	0		1 2 1 -1 1 2 1 -1			9 SY , 12 SY
κ	2	1	1		1 2 1 0 1 2 1 0			20 SY , 21 XY , 24 SY , 25 XY , 54 X , 56 X , 58 X , 60 X
μ	2	2	0		1 2 0 -1 1 2 0 0			66 K
μ	2	2	0		1 2 0 0 1 2 0 0			75 K
μ	2	2	1		1 2 0 0 1 2 0 1			71 K , 72 K
μ	2	2	1		1 2 0 1 1 2 0 1			79 K , 80 K
ν	2	2	0		1 2 2 0 2 1 0 1			73 K
ν	2	2	1		1 1 0 1 1 1 0 1 1 2 2 1			68 K , 70 K , 76 K , 77 K
o	4	2	0		1 4 1 -1 1 4 1 -1			43 S , 45 S

(continued on next page)

Table 4. Continued.

T	$ \alpha $	L_α	W_α	$f^{\tilde{\alpha}}$	$ \tilde{\alpha} $	$L_{\tilde{\alpha}}$	$W_{\tilde{\alpha}}$..., Group	HSP ₁	HSP ₂	..., ...	
					1	2	1	-1				
π	4	2	-1		1	2	1	-1	33S			
					1	2	1	-1				
					1	2	1	-1				
					1	2	1	-1				

4.2. Time-reversal symmetry

The role of TR symmetry is clarified through the transition from ordinary L to gray groups G . This involves magnetic (black-and-white, as well) little groups, and possibly new strata (with change of the ID), including HSPs of G not characterizing the corresponding L . An enlarged stabilizer of a momentum k may give rise to an enlarged degeneracy of the energy in k , while enlarged star necessarily enlarges the dimension of the associated coIR. In fact, the impact of TR symmetry is essentially encoded in the algorithm for co-representations construction. Irreducible co-representations [17, 18] of G_k are derived from IRs of L_k : each real IR (Wigner’s I kind) of L_k is extended to co-IR of G_k , a quaternion IR (II kind, equivalent to its conjugate, but without equivalent real IR) gives co-IR of the double dimension, while two mutually conjugate complex IRs give one co-IR of the double dimension. Hence, besides the case of an ordinary stabilizer $G_k = L_k$, TR symmetry preserves the HSP degeneracy also for crossings hosted by HSP invariant under magnetic group, but with allowed coIR determined by a real subgroup IR. On the other hand, the HSP degeneracy may be doubled for magnetic stabilizers with quaternion or complex subgroup IR. However, even when HSP degeneracy remains the same, the dispersion need not stay completely linear, and its shape may be not preserved. The enlarged group by TR imposes new conditions on Hamiltonian parameters and also affect the compatibility relations.

For this purpose to each of the stabilizer’s (co)IR we assign the number [18] $W = \frac{1}{L_k} \sum_{\ell \in L_k} \chi((\theta h \ell)^2)$, which shows whether it is composed of two (mutually non-equivalent $W = 0$, kind III, or equivalent $W = -1$, kind II) or one ($W = 1$, kind I) subgroup IR. It is given as the last entry in the tables 3 and 4 to enable tracking the role of TR symmetry. To illustrate, let us consider, for example, the transition $1 \xrightarrow{SO} 2 (\alpha)$ to IDC described in the subsection 4.1. In the table 4 this appears in 3 rows mutually differing by the last entry (column $W_{\tilde{\alpha}}$). In the third case, when both integer and half-integer coIRs carry the value $W_\alpha = W_{\tilde{\alpha}} = 1$, the corresponding groups appear also in table 3; this means that this type of transition is preserved under TR symmetry. On the contrary, the remaining two cases (with last entries 0 and -1 for half-integer coIRs) do not appear in table 3. This is expected since herein a conical dispersion in gray DLG is hosted by the half-integer coIR composed of two 1D subgroup half-integer IRs. Thus, breaking TR symmetry in these cases leads to non-crossing bands. The both situations are sketched in figure 4.

One can further similarly analyze relations between ordinary and gray groups case-by-case. In this way, combining the results from the both tables 4 and 3, different cluster processes can be found. Some of them are illustrated in figure 4; recall that all the crossings are symmetry enforced (thus no avoided crossing can appear). The skipped cases are with linearity rank 1 either in spinless or in spinfull case.

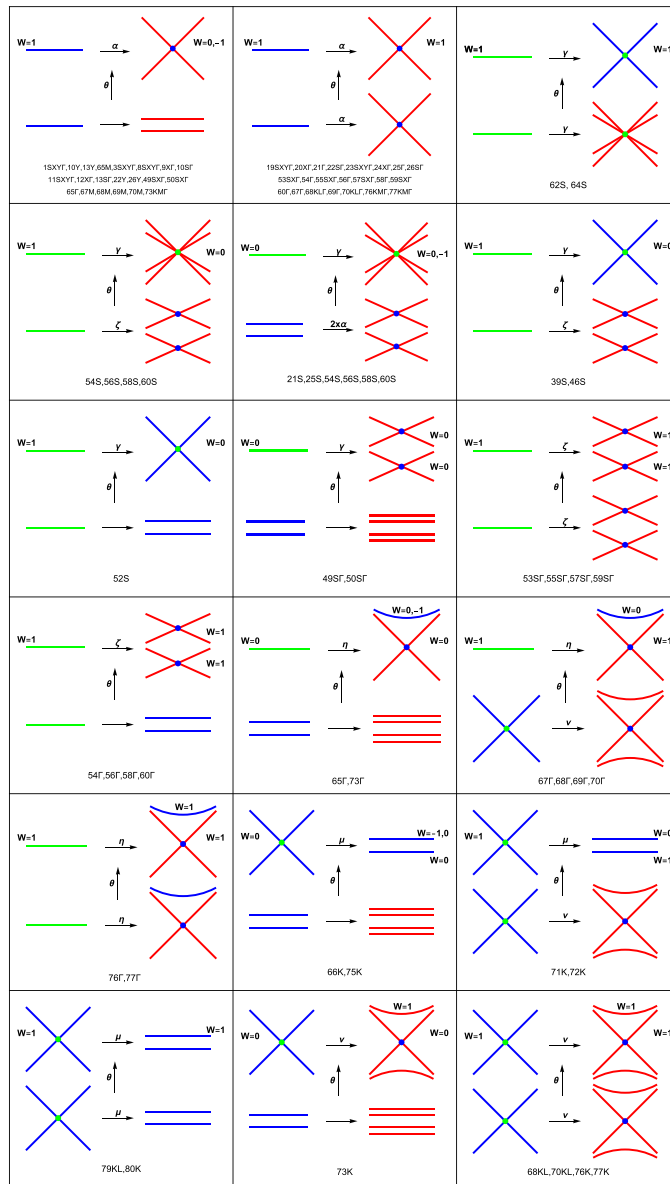


Figure 4. Manifestations of SO coupling and TR symmetry. Each figure describes transitions within a cluster at HSP (cluster and HSP are indicated at the bottom): horizontal arrows are for transitions from single to double groups (with the Greek letter indicating type from tables 3 and 4), while vertical ones are from ordinary to gray (with indicated kind of hosting coIR from table 4). Color of the bands is degeneracy in orbital-spin space: red, blue and green are for degeneracy 1, 2 and 4.

5. Discussion and conclusions

The linear dispersions at HSPs and underlying effective models allowed by integer and half-integer 2D and 4D (co)IRs are studied. Different dispersion types linear in all directions are classified and listed, completing thus the results existing in literature. Having these data at disposal, it was possible to analyze influence of SO coupling and TR symmetry to interrelate dispersions within the same cluster of the single/double ordinary/gray layer groups.

Obtained classification of the effective Hamiltonians may give some insight to band topology. One natural invariant is winding number, along paths around HSP hosting linear dispersion, as this point is a sort of singularity. For illustration, we calculated it for Hamiltonian (9), with result for each of the two bands $w = \text{sgn}(v_1^1 v_2^2 - v_1^2 v_2^1)$.

Summarizing results, firstly note that the LG clusters 2, 6, 14, 18, 37, 47, 51, 61, all of them being centrosymmetric, do not support linear band crossing in HSPs at all, while 4, 27, 35 and 74 do not support fully linear (with linearity rank 2), but have linearity rank 1 band crossings (see table 4). Further, as visible in table 2, the only fully linear 2D band crossing model in HSPs is 1DC. Notably, these are hosted at TRIM and non-TRIM points in ordinary single, as well as in ordinary and gray double groups in both symmorphic and non-symmorphic cases. In the remaining (gray single) groups, 1DC occurs only in K (thus not TRIM) point of some (symmorphic) groups [23, 24].

As for 4D models, inclusion of spin gives four-fold degenerate point with PF in two double groups (LG 62 and LG 64), while TR gives rise to FT dispersion [28] in 3 gray LGs. The presence of both spin and TR give rise to 4D coIRs in 27 gray double layer groups. Only 3 of them (7, 48, 52) are without special lines; their special points are surrounded by generic points with 2D allowed coIRs, enabling only 2DC dispersions. In all other 4D cases, besides 2DC cases (for 2D generic allowed coIRs), nondegenerate generic coIRs enable also four-band dispersion structures, but special lines with degenerate coIRs impose touching of pairs of bands, restricting linear rank 2 dispersions to PF and FT types. PF and FT types appear in noncentrosymmetric gray DLGs with a non-symmorphic symmetry: FT in 2 groups, and PF in 10 groups in total [29]. Degeneracy of the generic allowed representations in centrosymmetric gray DLGs admits 2DC dispersions, as it was proposed [11]; actually, this is realized in 15 of these groups, as in the remaining 3 (40, 44 and 63, nonsymmorphic) the dispersion is linear along a single direction, while the second one is special line (at BZ edge) with single 4D allowed coIR, thus becoming four-fold degenerate nodal line. In particular, concerning IDs, 2DC is found in three HSPs X, Y, S (gray DLGs 39, 46), in two HSPs X, S (52, 62, 64), in two HSPs Y, S (7, 15, 16, 38, 41), in two HSPs X, Y (17, 42), and single point Y (gray DLGs 43, 45, 48). In the groups 43 and 45 additional HSPs with four-fold band crossings, as required by fermion doubling theorem [15], are at X and S , but have linearity rank 1 (table 4). Concerning the whole BZ, note that for the groups 48, 52, 62, and 64 points X and Y are symmetry related. Thus, for engineering Dirac semimetals, it is particularly important to single out group 48, since effectively one need to tune band contacts only at a single point, i.e. for filling $4n + 2$, both (symmetry related) cones in BZ are on the Fermi level, if there are no additional electron or hole pockets.

It is interesting that simultaneously 2D and 4D completely linear dispersions are hosted only by the gray DLGs 21, 25, 32, 33, 34, 54, 56, 58, 60 (note that in these groups there are also HSPs with linearity rank 1). Note further, our results indicate that fermion doubling is not a general rule; namely, in some groups FT (e.g. gray LG33, LG43, LG45) and 2DC (e.g. double gray LG39 and LG46) are the only linear dispersions and appear in odd number of HSPs. More complex situation is with 1DC and PF, since whenever there are odd number of these dispersion, there are also other dispersion types.

Inclusion of the spin–orbit interaction causes various effects on the HSPs’ dispersions, including gap closing (α, γ, η), gap opening (ξ), cone preserving (ν), cone splitting (λ) scenarios (discussion about the cases with the linearity rank 1 is skipped). For example, an isotropic 1DC in gray LGs [23, 24], which is preserved (ν) by SO perturbation also in gray DLG, is at K point in symmorphic cluster 68, 70, 73, 76, 77. Similar analysis reported in [30] omitted symmorphic gray DLG 73. Concerning the TR symmetry breaking, we found also that the cone persists at K point in corresponding LGs and DLGs 68, 70, 76, 77, except in the group LG and DLG 73, where the vanishing TR symmetry opens a gap.

Besides spinless to spinfull transition, we examined influence of TR symmetry to dispersion at crossing point. Addition of TR symmetry may preserve or double the degeneracy in HSP. Concerning the preserved double degeneracy, our results single out the cases where 1DC appears both with and without TR symmetry, as well as those when TR even prevent linearity of dispersion. On the other hand, TR symmetry in centrosymmetric groups 62 and 64, although does not change four-fold degeneracy, modifies the dispersion type: in ordinary double groups two generic nondegenerate allowed IRs enable two positive (and two negative) bands touching along special lines (with single degenerate allowed IR); TR symmetry joins these IRs in a single 2D allowed coIR, transforming PF to 2DC dispersion.

Focusing on TR symmetric materials without and with SO from the literature, we further discuss applicability of our results. The frequently elaborated honeycomb lattice belongs to LG 80 with K point hosting Dirac cone being gaped by SO. That is symmetry prediction confirmed by DFT calculations in honeycomb lattices of C, Si, Ge, Sn or Pb elements [40, 41]. Buckled honeycomb lattice belongs to LG 72 with the same behavior of bands near K as in LG 80. Tight binding model on Si, Ge and Se elemental lattices [42] and DFT band structure of As_2X_2 ($X = Cl, F, I, Br$) monolayers [43] confirm our predictions. Similarly, Dirac cones split by SO near K point shows LG 66 with nonmagnetic high buckled $Co_2C_{18}H_{12}$ as DFT-example [44]. On the other hand LG 77 supports Dirac cones at K both without and with SO, with monolayer FeB_2 [45] and HfB_2 [46] as DFT-examples. Square LG 64 supports Dirac cones at X and S only in the presence of SO interaction; this is confirmed by DFT band structure of MX compounds ($M = Sc, Y; X = S, Se, Te$) [47] as well as in X point (S point was not discussed since the corresponding energies are too far from the Fermi level) in ARPES experiments and DFT calculations in synthesized layered 3D $ZrSiS$ [48] and numerically in monolayer $HfGeTe$ [49]. Experimentally synthesized α -bismuthene belongs to LG 42 and hosts spinfull Dirac cones at X and Y points, as confirmed by micro-ARPES technique and DFT calculations [50].

Among already reported structures with PF or FT dispersions are monolayer $GaXY$ ($X = Se, Te; Y = Cl, Br, I$), with non-centrosymmetric symmetry LG 32 providing SO caused Dirac cones at X point and PF at Y point. Indeed, fourfold degeneracy at Y point (called Dirac point in [51]) splits linearly away from it, as justified numerically [51] (dispersion near X point was not discussed more closely). DFT band structure of monolayer Ta_3SiTe_6 and Nb_3SiTe_6 [52] requires some attention. Corresponding structure with space group $Pmc2_1$ (SG 26 in notation [53]) is obtained by periodic distribution of monolayers along vertical axis. The monolayers may be of the symmetry either LG 28 or LG 29; these two groups are similar, both with the horizontal screw axis of order two, and two planes, the vertical one is mirror and the horizontal glide in LG 28, while in LG 29 the vertical is glide and the horizontal is mirror. LG 28 should host PF dispersions at the points Y and S , with low energy effective six-parameters Hamiltonian. However, monolayers Ta_3SiTe_6 and Nb_3SiTe_6 have horizontal symmorphic mirror plane [52], and their symmetry group is LG 29, with FT dispersions (special case of PF) at Y and S points, and effective Hamiltonian having four independent real parameters. Indeed, linear dispersion in Y and S points are reported [52] (instead of minimal 4 parameters authors use 6 as for LG 28, which can not affect the result).

Since surfaces of (semi-infinite) 3D single crystals are also periodic in two directions, some layer groups are also wallpaper groups being the symmetries of surfaces. Those contain symmetry elements that do not flip the surface-normal: perpendicular (to the surface) rotational axes of order two, three, four, or six, and perpendicular mirror, or glide planes. It may happen that surface reconstruction or adding atoms at surface in regular manner can lower the symmetry. Such is the case for thin layer consisting of odd number of silicon (110)-sheets, where FT dispersion was found experimentally [54]. FT dispersion was caused by the Coulomb interaction (described by gray LGs) rather than by the relativistic corrections (described by gray DLGs) so linear dispersion is maintained over wide energy range. In addition, BZ of reconstructed surface shrinks, so that another FT dispersion at the center of rectangular surface BZ might be obtained by intersection from FT bands originating from the corners. This might explain why FT dispersion at \bar{X} of Si(110)-surface BZ, seen in ARPES [54], remained intact by different surface reconstruction types.

3D TIs are known [19] to have large SO coupling that causes Dirac cones at surface states. Our results apply also to TIs with the remark that only surface states that fall within the bulk gap are investigated in the literature, since they give rise to surface conductivity. The surface states with the energy within the bulk gap, are identified by analysis of topological properties of bulk bands (via bulk-boundary correspondence) and cannot be predicted by group theory alone. 3D compounds Bi_2Se_3 , Bi_2Te_3 , Sb_2Te_3 and Sb_2Se_3 belong to the SG 166 ($R\bar{3}m$) with (111) surface with symmetry gray DLG 69 so Dirac cones are expected in $\bar{\Gamma}$ and \bar{M} of the surface BZ. DFT calculations show that first three materials have surface Dirac cone at $\bar{\Gamma}$ within the bulk gap, while states near \bar{M} fall far out of the bulk gap and were not shown. On the other hand the last compound Sb_2Se_3 does not have surface states in the gap and it is not TI [55]. Surface low energy effective Hamiltonian near $\bar{\Gamma}$ has one real parameter, in accordance with our results. Surface Dirac cone in $\bar{\Gamma}$ has been seen in ARPES experiments in Bi_2Te_3 and Sb_2Te_3 [56]. Similarly, 3D compound LaBi crystallizes in SG 225 ($Fm\bar{3}m$) with (001) surface having symmetry LG 55. SOC Dirac cones are expected to appear on \bar{S} , $\bar{\Gamma}$, and \bar{X} points of the BZ. ARPES experiments supported by DFT calculations show Dirac cones at $\bar{\Gamma}$ and \bar{S} in the bulk gap, while bands near \bar{X} were outside the gap [57]. Theoretically proposed 3D compound Sr_2Pb_3 , that belongs to SG 127 ($P4/m\bar{3}m$) and its (001) surface to LG 56 (wallpaper group 12 in notation [53]), is expected to be non-symmorphic TI [15]. Our result show that SO causes Dirac cone at $\bar{\Gamma}$ and PF at \bar{M} point for LG 56. DFT band structure show linear dispersions from fourfold degenerate energy at \bar{M} [15]. Their effective low energy Hamiltonian has two independent real parameters and suggests that the dispersion is Dirac-like (2DC in our notation). Necessary splitting that causes bands along $\bar{M}-\bar{\Gamma}$ to be non-degenerate (as required by symmetry) was attributed to quadratic corrections to the effective Hamiltonian [15]. Our analysis indicates that the dispersion at \bar{M} should be PF, with three-parameters Hamiltonian and with bands along $\bar{M}-\bar{\Gamma}$ being non-degenerate already in the linear approximation.

The presented theoretical framework is straightforwardly extendable to (ferro/anti-ferro) magnetic systems invariant under black-and-white ordinary or double groups. Also, it can be used on an equal footing to analyze higher order dispersion terms, dispersions in the vicinity of special lines which occur in 2D BZ of layer materials, as well as to clarify the cases with single linear direction in energy.

Acknowledgments

Authors acknowledge funding by the Ministry of Education, Science and Technological Development of the Republic of Serbia provided by the Institute of Physics Belgrade (VD), Faculty of Physics (NL and MD) and Serbian Academy of Sciences and Arts (MD).

Data availability statement

All data that support the findings of this study are included within the article (and any supplementary files).

ORCID iDs

N Lazić  <https://orcid.org/0000-0002-3634-0301>

V Damljanović  <https://orcid.org/0000-0001-7517-6439>

M Damjanović  <https://orcid.org/0000-0003-2806-253X>

References

- [1] Yan B and Felser C 2017 Topological materials: Weyl semimetals *Annu. Rev. Condens. Matter Phys.* **8** 337–54
- [2] Armitage N P, Mele E J and Vishwanath A 2018 Weyl and Dirac semimetals in three-dimensional solids *Rev. Mod. Phys.* **90** 015001
- [3] Gao H, Venderbos J W F, Kim Y and Rappe A M 2019 Topological semimetals from first principles *Annu. Rev. Mater. Res.* **49** 153–83
- [4] Wieder B J, Kim Y, Rappe A M and Kane C L 2016 Double Dirac semimetals in three dimensions *Phys. Rev. Lett.* **116** 186402
- [5] Barry B, Cano J, Wang Z, Vergniory M G, Felser C, Cava R J and Andrei Bernevig B 2016 Beyond Dirac and Weyl fermions: unconventional quasiparticles in conventional crystals *Science* **353** aaf5037
- [6] Zhu Z, Winkler G W, Wu Q, Ju L and Soluyanov A A 2016 Triple point topological metals *Phys. Rev. X* **6** 031003
- [7] Wang Z, Alexandradinata A, Cava R J and Andrei Bernevig B 2016 Hourglass fermions *Nature* **532** 189–94
- [8] Abrikosov A A and Beneslavskii S D 1971 Possible existence of substances intermediate between metals and dielectrics *Sov. Phys. JETP* **32** 699–708
- [9] Mañes J L 2012 Existence of bulk chiral fermions and crystal symmetry *Phys. Rev. B* **85** 155118
- [10] Fang C, Gilbert M J, Dai X and Andrei Bernevig B 2012 Multi-Weyl topological semimetals stabilized by point group symmetry *Phys. Rev. Lett.* **108** 266802
- [11] Young S M and Kane C L 2015 Dirac semimetals in two dimensions *Phys. Rev. Lett.* **115** 126803
- [12] van Miert G and Morais Smith C 2016 Dirac cones beyond the honeycomb lattice: a symmetry-based approach *Phys. Rev. B* **93** 035401
- [13] Kim J, Baik S S, Jung S W, Sohn Y, Ryu S H, Choi H J, Yang B-J and Kim K S 2017 Two-dimensional Dirac fermions protected by space-time inversion symmetry in black phosphorus *Phys. Rev. Lett.* **119** 226801
- [14] Park S and Yang B-J 2017 Classification of accidental band crossings and emergent semimetals in two-dimensional noncentrosymmetric systems *Phys. Rev. B* **96** 125127
- [15] Wieder B J, Barry B, Wang Z, Cano J, Kim Y, Kim H-S D, Rappe A M, Kane C L and Andrei Bernevig B 2018 Wallpaper fermions and the nonsymmorphic Dirac insulator *Science* **361** 246–51
- [16] Yang J, Fang C and Liu Z-X 2021 Symmetry-protected nodal points and nodal lines in magnetic materials *Phys. Rev. B* **103** 245141

- [17] Dimmock J O and Wheeler R G 1962 Irreducible representations of magnetic groups *J. Phys. Chem. Solids* **23** 729–41
- [18] Bradley C J and Davies B L 1968 Magnetic groups and their corepresentations *Rev. Mod. Phys.* **40** 359–79
- [19] Hasan M Z and Kane C L 2010 Colloquium: topological insulators *Rev. Mod. Phys.* **82** 3045–67
- [20] Qi X-L and Zhang S-C 2011 Topological insulators and superconductors *Rev. Mod. Phys.* **83** 1057–110
- [21] Kruthoff J, de Boer J, van Wezel J, Kane C L and Slager R-J 2017 Topological classification of crystalline insulators through band structure combinatorics *Phys. Rev. X* **7** 041069
- [22] Asano K and Hotta C 2011 Designing Dirac points in two-dimensional lattices *Phys. Rev. B* **83** 245125
- [23] Damljanić V and Gajić R 2016 Existence of Dirac cones in the Brillouin zone of diperiodic atomic crystals according to group theory *J. Phys.: Condens. Matter* **28** 085502
- [24] Damljanić V and Gajić R 2016 Addendum to ‘existence of Dirac cones in the Brillouin zone of diperiodic atomic crystals according to group theory’ *J. Phys.: Condens. Matter* **28** 439401
- [25] Wieder B J and Kane C L 2016 Spin–orbit semimetals in the layer groups *Phys. Rev. B* **94** 155108
- [26] Wang J 2017 Antiferromagnetic Dirac semimetals in two dimensions *Phys. Rev. B* **95** 115138
- [27] Young S M and Wieder B J 2017 Filling-enforced magnetic Dirac semimetals in two dimensions *Phys. Rev. Lett.* **118** 186401
- [28] Damljanić V, Popov I and Gajić R 2017 Fortune teller fermions in two-dimensional materials *Nanoscale* **9** 19337–45
- [29] Damljanić V, Lazić N, Šolajić A, Pešić J, Nikolić B and Damjanović M 2020 Peculiar symmetry-protected electronic dispersions in two-dimensional materials *J. Phys.: Condens. Matter* **32** 485501
- [30] Luo W, Ji J, Lu J, Zhang X and Xiang H 2020 Two-dimensional topological semimetals protected by symmorphic symmetries *Phys. Rev. B* **101** 195111
- [31] Tang F and Wan X 2021 Exhaustive construction of effective models in 1651 magnetic space groups *Phys. Rev. B* **104** 085137
- [32] Yu Z-M, Zhang Z, Liu G-B, Wu W, Li X-P, Zhang R-W, Yang S A and Yao Y 2022 Encyclopedia of emergent particles in three-dimensional crystals *Sci. Bull.* **67** 375–80
- [33] Bouhon A, Lange G F and Slager R-J 2021 Topological correspondence between magnetic space group representations and subdimensions *Phys. Rev. B* **103** 245127
- [34] Damjanović M and Milošević I 2015 Full symmetry implementation in condensed matter and molecular physics—modified group projector technique *Phys. Rep.* **581** 1–43
- [35] Nikolić B, Milošević I, Vuković T, Lazić N, Dmitrović S, Popović Z and Damjanović M 2022 Irreducible and site-symmetry-induced representations of single/double ordinary/grey layer groups *Acta Crystallogr. A* **78** 107–14
- [36] Jansen L and Boon M 1967 *Theory of Finite Groups. Applications in Physics* (Amsterdam: North-Holland)
- [37] de la Flor G, Souvignier B, Madariaga G and Aroyo M I 2021 Layer groups: Brillouin-zone and crystallographic databases on the Bilbao crystallographic server *Acta Crystallogr. A* **77** 559–71
- [38] Kopsky V and Litvin D B 2002 *International Tables of Crystallography Volume E: Subperiodic Groups* (Dordrecht: Kluwer)
- [39] Jin Y J, Zheng B B, Xiao X L, Chen Z J, Xu Y and Xu H 2020 Two-dimensional Dirac semimetals without inversion symmetry *Phys. Rev. Lett.* **125** 116402
- [40] Yakovkin I N 2017 Spin–orbit band gaps and destruction of Dirac cones *Surf. Sci.* **662** 1–5
- [41] Gutzler R and Christian Schön J C 2017 Two-dimensional silicon-carbon compounds: structure prediction and band structures *Z. Anorg. Allg. Chem.* **643** 1368–73
- [42] Liu C-C, Jiang H and Yao Y 2011 Low-energy effective Hamiltonian involving spin–orbit coupling in silicene and two-dimensional germanium and tin *Phys. Rev. B* **84** 195430
- [43] Tang W, Sun M, Ren Q, Wang S and Yu J 2016 Halogenated arsenenes as Dirac materials *Appl. Surf. Sci.* **376** 286–9
- [44] Ma Y, Dai Y, Li X, Sun Q and Huang B 2014 Prediction of two-dimensional materials with half-metallic Dirac cones: $\text{Ni}_2\text{C}_{18}\text{H}_{12}$ and $\text{Co}_2\text{C}_{18}\text{H}_{12}$ *Carbon* **73** 382–8
- [45] Zhang H, Li Y, Hou J, Du A and Chen Z 2016 Dirac state in the FeB_2 monolayer with graphene-like boron sheet *Nano Lett.* **16** 6124–9
- [46] Liu Z, Wang P, Cui Q, Yang G, Jin S and Xiong K 2019 Theoretical prediction of HfB_2 monolayer, a two-dimensional Dirac cone material with remarkable Fermi velocity *RSC Adv.* **9** 2740–5

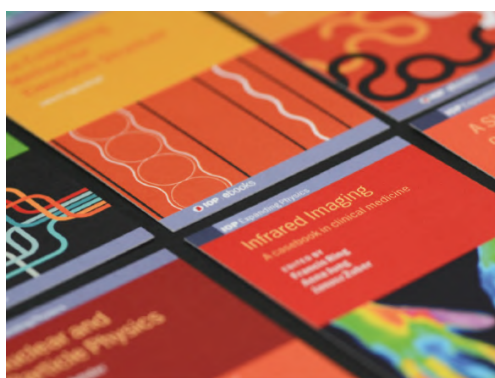
- [47] Guo H, Zhao J, Chen C, Li S, Jiang W, Fan H, Tian X and Yang S A 2020 Nonsymmorphic nodal-line metals in the two-dimensional rare earth monochalcogenides MX ($M = \text{Sc, Y}$; $X = \text{S, Se, Te}$) *J. Mater. Sci.* **55** 14883–92
- [48] Schoop L M *et al* 2016 Dirac cone protected by non-symmorphic symmetry and three-dimensional Dirac line node in ZrSiS *Nat. Commun.* **7** 11696
- [49] Guan S, Liu Y, Yu Z-M, Wang S-S, Yao Y and Yang S A 2017 Two-dimensional spin-orbit Dirac point in monolayer HfGeTe *Phys. Rev. Materials* **1** 054003
- [50] Kowalczyk P J *et al* 2020 Realization of symmetry-enforced two-dimensional Dirac fermions in nonsymmorphic α -bismuthene *ACS Nano* **14** 1888–94
- [51] Wu W, Jiao Y, Li S, Sheng X-L, Yu Z-M and Yang S A 2019 Hourglass Weyl loops in two dimensions: theory and material realization in monolayer GaTeI family *Phys. Rev. Mater.* **3** 054203
- [52] Li S, Liu Y, Wang S-S, Yu Z-M, Guan S, Sheng X-L, Yao Y and Yang S A 2018 Nonsymmorphic-symmetry-protected hourglass Dirac loop, nodal line, and Dirac point in bulk and monolayer $X_3\text{SiTe}_6$ ($X = \text{Ta, Nb}$) *Phys. Rev. B* **97** 045131
- [53] Hahn T 2005 *International Tables of Crystallography Volume A: Space-Group Symmetry* (Berlin: Springer)
- [54] Kopcuszyński M, Krawiec M, Żurawek L and Zdyb R 2020 Experimental evidence of a new class of massless fermions *Nanoscale Horiz.* **5** 679–82
- [55] Zhang H, Liu C-X, Qi X-L, Dai X, Fang Z and Zhang S-C 2009 Topological insulators in Bi_2Se_3 , Bi_2Te_3 and Sb_2Te_3 with a single Dirac cone on the surface *Nat. Phys.* **5** 438–42
- [56] Hsieh D *et al* 2009 Observation of time-reversal-protected single-Dirac-cone topological-insulator states in Bi_2Te_3 and Sb_2Te_3 *Phys. Rev. Lett.* **103** 146401
- [57] Nayak J *et al* 2017 Multiple Dirac cones at the surface of the topological metal LaBi *Nat. Commun.* **8** 13942

PAPER

Peculiar symmetry-protected electronic dispersions in two-dimensional materials

To cite this article: V Damjanovi *et al* 2020 *J. Phys.: Condens. Matter* **32** 485501

View the [article online](#) for updates and enhancements.



IOP | ebooks™

Bringing together innovative digital publishing with leading authors from the global scientific community.

Start exploring the collection—download the first chapter of every title for free.

Peculiar symmetry-protected electronic dispersions in two-dimensional materials

V Damljanović^{1,3} , N Lazic² , A Šolajić¹ , J Pešić¹ , B Nikolić²  and M Damjanović² 

¹ Institute of Physics Belgrade, University of Belgrade, Pregrevica 118, 11080 Belgrade, Serbia

² NanoLab, Faculty of Physics, University of Belgrade, PO Box 44, Belgrade 11001, Serbia

E-mail: damlja@ipb.ac.rs

Received 16 June 2020, revised 23 July 2020

Accepted for publication 30 July 2020

Published 8 September 2020



Abstract

Symmetry indicates that low energy spectra of materials could be richer than well-known Dirac, semi-Dirac, or quadratic, hosting some unusual quasiparticles. Performing the systematic study of exact forms of low energy effective Hamiltonians and dispersions in high-symmetry points with fourfold degeneracy of bands, we found new, previously unreported dispersion, which we named poppy flower (PF) after its shape. This massless fermion exists in non-magnetic two-dimensional (2D) crystals with spin-orbit coupling (SOC), which are invariant under one of the proposed ten noncentrosymmetric layer groups. We suggest real three-dimensional (3D) layered materials suitable for exfoliation, having layers that belong to these symmetry groups as candidates for realization of PF fermions. In 2D systems without spin-orbit interaction, fortune teller (FT)-like fermions were theoretically predicted, and afterward experimentally verified in the electronic structure of surface layer of silicon. Herein, we show that such fermions can also be hosted in 2D crystals with SOC, invariant under additional two noncentrosymmetric layer groups. This prediction is confirmed by density functional based calculation: layered BiIO₄, which has been synthesized already as a 3D crystal, exfoliates to stable monolayer with symmetry *pb2₁a*, and FT fermion is observed in the band structure. Analytically calculated density of states (DOS) of the PF shows semimetallic characteristic, in contrast to metallic nature of FT having non-zero DOS at the bands contact energy. We indicate possibilities for symmetry breaking patterns which correspond to the robustness of the proposed dispersions as well as to the transition from Dirac centrosymmetric semimetal to PF.

Keywords: electronic dispersions, spin-orbit coupling, symmetry, new fermions

(Some figures may appear in colour only in the online journal)

1. Introduction

Electronic dispersion essentially determines crystal properties and it is well known that it is assigned by quantum numbers of the underlying symmetry group. These are space, layer (including wallpaper) or line groups, referring respectively to dimensionality of crystals: 3D, quasi-2D (Q2D), or quasi-1D. Probably the most famous example of a low-dimensional material is graphene (there are also related single layers, such as borophene [1], borophosphene [2], graphynes

[3], etc), which hosts Dirac like (linear in quasi-momentum) dispersion in the vicinity of high symmetry Dirac points. Such shape of energy bands, besides being responsible for some intriguing phenomena, provides material realization of relativistic electron. This triggered numerous investigations of the connection between symmetry of materials and appearance of Dirac and Weyl points in their band structures. These points are attributed to existence of rotational [4], nonsymmorphic [5], mirror [6], space-time inversion [7, 8], time-reversal plus fractional translation [9], and generalized chiral symmetry [10]. There are also results on the search for Weyl and Dirac

³ Author to whom any correspondence should be addressed.

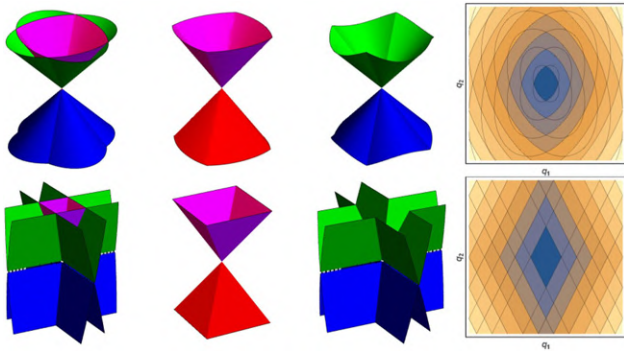


Figure 1. PF (up) and FT (bottom) dispersions (given by equations (3.1)): from left to right are all bands, bands $E_{\pm 1,+1}$, bands $E_{\pm 1,-1}$ and horizontal sections of the bands (iso-energetic lines).

points according to group theoretical criteria in Brillouin zones (BZs) of all space [11], layer [12–14] or wallpaper groups [15].

In addition, geometrical symmetries impose conditions that lead to the emergence of unconventional quasiparticles in condensed matter systems. In 3D materials, enforced by space groups, double Dirac points [16], three-component [17, 18] or hourglass fermions [19] are found, inspiring further theoretical and experimental research [20–25]. Concerning Q2D systems, besides Dirac (as in graphene [26]), there are also semi-Dirac (Dirac-like in one direction, and quadratic in the orthogonal one, as in black phosphorus [27]), quadratic (as in molybdenum disulphide [28]), and fortune teller (FT) dispersions [29], which corresponds to the coexistence of a nodal point and lines. Namely, symmetry analysis of the possible completely linear dispersions in non-magnetic, Q2D materials with negligible spin–orbit coupling (SOC) has shown that only completely massless fermions appearing in layers are Dirac and FT [29]. Recently, FT dispersion has been experimentally confirmed in a surface layer of silicon [30].

A question arises whether new types of fermions are possible in Q2D materials by inclusion of SOC? With help of layer double groups (LDGs) and time-reversal symmetry (TRS) (i.e. gray LDG), we made a quite general search for linear dispersions in the vicinity of high symmetry points (HSPs); since no reference to nonsymmorphic symmetries is made, the topological (hour-glass like) band crossing mechanisms are not *a priori* assumed, as it is usual. Indeed, it turns out that there are two peculiar types (figure 1) featuring twelve nonsymmorphic and noncentrosymmetric groups: two groups support previously predicted FT, and the remaining ones poppy flower (PF) dispersion (generalizing both FT and Dirac types).

After a brief overview of necessary group-theoretical methods, the obtained results are discussed on the basis of effective low-energy model, calculated densities of states and symmetry breaking patterns. Also, a list of material candidates supporting the new dispersions is provided. The predicted effect is justified by density functional based relaxation and band structure calculation in BiIO₄ monolayer. Synthesis of this layered 3D material was reported around a decade ago [31]. Numerical band structure con-

firms our group theoretical prediction, which may be the motivation for future laboratory synthesis of this material as monolayer.

2. Method

Symmetry determines Bloch Hamiltonian in the vicinity of high-symmetry BZ wave vector through the allowed irreducible representations (IRs) of the little group [32]. Allowed IRs of LDGs are subduced from the corresponding space groups IRs (found on Bilbao Crystallographic Server [33]), and also independently constructed by POL-Sym code [34]. Concerning LDGs with TRS, the dimensions [33, 35] of the allowed IRs (actually co-representations) are 1, 2 or 4, and for generic ones, giving bands degeneracy, this is 1 or 2. Here we focus on the band structures near quadruple points at high-symmetry momenta. Further, we do not consider generically degenerate bands, giving double degenerate Dirac dispersion (precisely, it consists of two double spinfull degenerate cones meeting at one fourfold degenerate point); this automatically excludes centrosymmetric crystals, as Kramers degeneracy in them forbids non-degenerate bands [36]. Among the remaining groups, only twelve are with special points with four-dimensional allowed (co)representation.

Analysis of all allowed IRs R of little groups $G(\mathbf{k}_0)$ of HSPs \mathbf{k}_0 in LDG lacking the inversion symmetry gives the following conditions for quadruple point: \mathbf{k}_0 is time-reversal invariant momentum, R is two-dimensional, either real or complex IR. Therefore, we consider $\hat{H}(\mathbf{k})$ being Hamiltonian of the system \hat{H}_0 (including spin–orbit) in the basis $\{|\Psi_1\rangle, |\Psi_2\rangle, |\theta\Psi_1\rangle, |\theta\Psi_2\rangle\}$, where the spinors $|\Psi_i\rangle = |\Psi_i(\mathbf{k})\rangle$ ($i = 1, 2$ counts two bands touching each other at \mathbf{k}_0 also in the absence of TRS) belong to R at \mathbf{k}_0 and θ is an anti-unitary operator of TRS, for which we used $\theta^2 = -\hat{\sigma}_0$, since spinfull case is considered. Throughout the text $\hat{\sigma}_0$ is two-by-two unit matrix, and $\hat{\sigma}_1, \hat{\sigma}_2, \hat{\sigma}_3$ are Pauli matrices. Denoting the little group elements by $\ell = (h|\mathbf{r}_{\hat{h}} + \mathbf{b})$, where h is crystallographic double point group element, while $\mathbf{r}_{\hat{h}}$ and \mathbf{b} are fractional and lattice translation, respectively, one gets the conditions imposed by time-reversal and geometrical symmetries on $\hat{H}(\mathbf{k}_0 + \mathbf{q})$ in the vicinity of \mathbf{k}_0 (therefore, the wavevector \mathbf{q} is small):

$$\hat{H}^*(\mathbf{k}_0 + \mathbf{q}) = \hat{T}^\dagger \hat{H}(\mathbf{k}_0 - \mathbf{q}) \hat{T}, \quad (2.1)$$

$$\hat{H}(\mathbf{k}_0 + \mathbf{q}) = \hat{D}^\dagger(\ell) \hat{H}(\mathbf{k}_0 + \hat{h}'\mathbf{q}) \hat{D}(\ell). \quad (2.2)$$

Here, $\hat{D} = \text{diag}(\hat{R}, \hat{R}^*)$, and \hat{h}' is an operator reduction of vector representation \hat{h} to 2D BZ, while $\hat{T} = -i\hat{\sigma}_2 \otimes \hat{\sigma}_0$ represents the action of θ on the basis of spinors.

To focus on the terms linear in \mathbf{q} , Hamiltonian is expanded in the form $\hat{H}(\mathbf{k}_0 + \mathbf{q}) \approx \sum_{i=1,2} q_i \frac{\partial \hat{H}(\mathbf{k}_0 + \mathbf{q})}{\partial q_i} \Big|_{\mathbf{q}=0}$ (energy scale is conveniently shifted such that $\hat{H}(\mathbf{k}_0) = 0$). To incorporate symmetry, the matrix elements of the Hamiltonian gradient are arranged into the four-by-eight matrix \hat{W} , which entries $w_{pq} = (w_{pq}^1 \ w_{pq}^2)$ are pairs $w_{pq}^i = \frac{\partial H_{pq}(\mathbf{k}_0 + \mathbf{q})}{\partial q_i} \Big|_{\mathbf{q}=0}$. The form

Table 1. Groups providing dispersions (3.1). Notations for layer (columns 1 and 2) and space groups (columns 4, 5 and 6) are according to [37, 38] respectively. IR notation in the eighth column is as in Bilbao Crystallographic Server [33]. Effective Hamiltonian is indicated in the last column by the nonzero parameters (and their interrelations) of (2.5). For the last four groups $a = c$ while \bar{M}_6 and \bar{M}_7 are conjugated pair of IRs.

Layer double group			Corresponding space double group				Dispersion	Nonzero v_{pq}^i	
Group	IR	Group	Plane	IR	IR				
21	$p2_12_12$	\bar{S}_5	18	$P2_12_12$	D_2^3	$z = 0$	\bar{S}_5	(3.1a)	$v_{13}^1, v_{23}^1, v_{33}^1, v_{11}^2, v_{21}^2, v_{31}^2$
25	$pba2$	\bar{S}_5	32	$Pba2$	C_{2v}^8	$z = 0$	\bar{S}_5	(3.1a)	$v_{13}^1, v_{23}^1, v_{33}^1, v_{11}^2, v_{21}^2, v_{31}^2$
28	$pm2_1b$	\bar{Y}_5, \bar{S}_5	26	$Pmc2_1$	C_{2v}^2	$y = 0$	\bar{Z}_5, \bar{U}_5	(3.1a)	$v_{11}^1, v_{21}^1, v_{31}^1, v_{10}^2, v_{20}^2, v_{30}^2$
29	$pb2_1m$	\bar{Y}_5, \bar{S}_5	26	$Pmc2_1$	C_{2v}^2	$x = 0$	\bar{Z}_5, \bar{T}_5	(3.1b)	$v_{11}^1, v_{21}^1, v_{31}^1, v_{10}^2, v_{20}^2, v_{30}^2$
30	$pb2b$	\bar{Y}_5, \bar{S}_5	27	$Pcc2$	C_{2v}^3	$x = 0$	\bar{Z}_5, \bar{T}_5	(3.1a)	$v_{11}^1, v_{21}^1, v_{31}^1, v_{10}^2, v_{20}^2, v_{30}^2$
32	$pm2_1n$	\bar{Y}_5	31	$Pmn2_1$	C_{2v}^7	$y = 0$	\bar{Z}_5	(3.1a)	$v_{13}^1, v_{23}^1, v_{33}^1, v_{10}^2, v_{20}^2, v_{30}^2$
33	$pb2_1a$	\bar{Y}_5	29	$Pca2_1$	C_{2v}^5	$y = 0$	\bar{Z}_5	(3.1b)	$v_{13}^1, v_{23}^1, v_{33}^1, v_{10}^2, v_{20}^2, v_{30}^2$
34	$pb2n$	\bar{Y}_5	30	$Pnc2$	C_{2v}^6	$x = 0$	\bar{Z}_5	(3.1a)	$v_{13}^1, v_{23}^1, v_{33}^1, v_{10}^2, v_{20}^2, v_{30}^2$
54	$p42_12$	(\bar{M}_6, \bar{M}_7)	90	$P42_12$	D_4^2	$z = 0$	(\bar{M}_6, \bar{M}_7)	(3.1a)	$\left\{ \begin{array}{l} v_{02}^1 = v_{02}^2 = v_{31}^1 = -v_{31}^2 \\ v_{10}^1 = v_{10}^2 = v_{23}^1 = -v_{23}^2 \\ v_{13}^1 = -v_{13}^2 = -v_{20}^1 = -v_{20}^2 \end{array} \right\}$
56	$p4bm$	(\bar{M}_6, \bar{M}_7)	100	$P4bm$	C_{4v}^2	$z = 0$	(\bar{M}_6, \bar{M}_7)	(3.1a)	
58	$p\bar{4}2_1m$	(\bar{M}_6, \bar{M}_7)	113	$P\bar{4}2_1m$	D_{2d}^3	$z = 0$	(\bar{M}_6, \bar{M}_7)	(3.1a)	
60	$p\bar{4}b2$	(\bar{M}_6, \bar{M}_7)	117	$P\bar{4}b2$	D_{2d}^7	$z = 0$	(\bar{M}_6, \bar{M}_7)	(3.1a)	

$$\hat{W} = \begin{pmatrix} w_{11} & w_{12} & w_{13} & w_{14} \\ w_{12}^* & w_{22} & w_{14} & w_{24} \\ w_{13}^* & w_{14}^* & -w_{11} & -w_{12}^* \\ w_{14}^* & w_{24}^* & -w_{12} & -w_{22} \end{pmatrix} \quad (2.3)$$

follows from the relation (2.1), together with $w_{pq}^i = w_{qp}^{i*}$ corresponding to the requirement that Hamiltonian \hat{H} is a Hermitian operator. Note that the form (2.3) of \hat{W} leads to the traceless Hamiltonian: it excludes the scalar term (which imposes the tilt of the bands). The geometrical symmetries are incorporated by (2.2), which is rewritten [11, 29] as an efficient fixed point condition

$$\left| \hat{W} \right\rangle = \hat{D} \otimes \hat{D}^* \otimes \hat{h}' \left| \hat{W} \right\rangle, \quad (2.4)$$

on the column vector (32×1) form $\left| \hat{W} \right\rangle$ of \hat{W} . The equation (2.4) is solved with help of the group projection operators for all of the twelve noncentrosymmetric groups hosting quadruple points at high symmetry momenta; in this way, the symmetry determines form of \hat{W} . To explicate this, it is more convenient to use another general expansion of the effective low energy Hamiltonian,

$$\hat{H}(\mathbf{q}) = \sum_{p,q=0}^3 \sum_{i=1}^2 q_i v_{pq}^i \hat{\sigma}_p \otimes \hat{\sigma}_q, \quad (2.5)$$

and find the constraints imposed by symmetry on the real coefficients v_{pq}^i (simply interrelated with w_{pq}^i).

3. Results and discussion

3.1. Symmetry adapted Hamiltonians and dispersions

Groups hosting new dispersions are listed in table 1. Besides intrinsic layer group notation (the first part), the space group

of the system obtained by periodic repetition of the layer along axis perpendicular to it (column plane) according to Bilbao Crystallographic Server is also given (second part), where the directions x , y and z are along axes of orthorhombic/tetragonal 3D primitive unit cell. On the other hand, in POLSym approach we used convention that layers are in xy -plane. Orthogonal lattice vectors \mathbf{a}_1 and \mathbf{a}_2 span primitive rectangular/square 2D unit cell, while reciprocal lattice vectors \mathbf{k}_1 and \mathbf{k}_2 satisfy $\mathbf{a}_j \cdot \mathbf{k}_l = 2\pi\delta_{jl}$ and q_1, q_2 are projections of \mathbf{q} along \mathbf{k}_1 and \mathbf{k}_2 . Relevant BZs are in figure 2.

Effective Hamiltonians allowed by symmetry group in the special points of Brillouin's zone are presented in the last column of the table 1: the nonzero real coefficients v_{pq}^i in the expansion (2.5) are specified, together with the constraints among them. The listed forms correspond to the group settings (lattice vectors and coordinate origin) and double valued irreducible co-representations obtained by POLSym code. In fact, this enabled flexibility in the choice of generators (coordinate system and translational periods), which finally results in the form of irreducible co-representations. These are chosen such to get the same form of the effective Hamiltonian whenever it is possible (for different groups). Equivalent (but different) settings (and co-representations) produce different (still equivalent with respect to dispersions) Hamiltonian forms. Clearly, the exact values of the nonzero coefficients v_{pq}^i (listed in the last column of the table 1) are material dependent. The groups' generators and their representative matrices in the allowed co-representations associated to the specified high-symmetry points are in the table 2. It should be remarked that in all the considered cases this point is fixed by the whole gray group, i.e. the little group is the gray (double) group, and the allowed co-representations of the little group are simultaneously the irreducible co-representations of the gray group. The matrices of the relevant co-representations are four-dimensional. In all the cases time-reversal corresponds to the matrix \hat{T} ; all other generators are represented by the block-diagonal

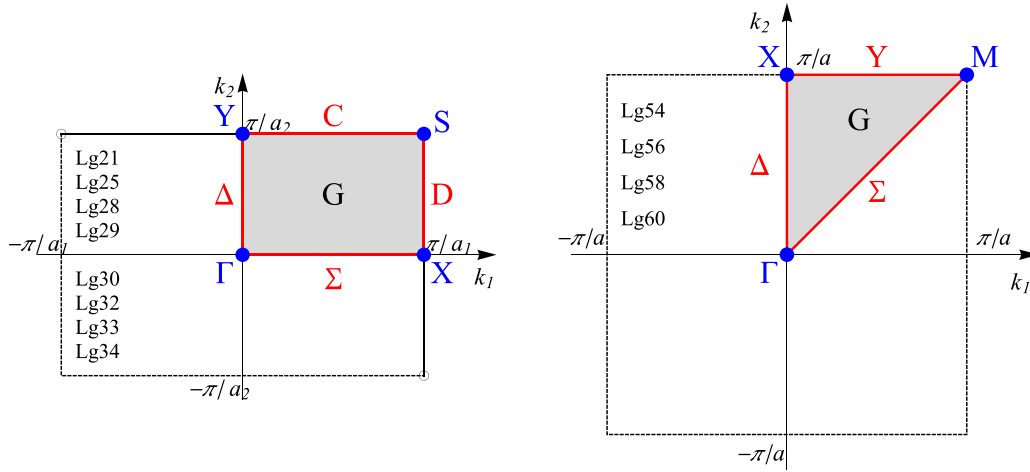


Figure 2. BZs of the groups (listed in table 1) supporting dispersions (3.1). For layer groups 28, 29, 30, 32, 33 and 34 vector k_2 is along (screw) axis of order two.

matrices $\hat{D} = \text{diag}(\hat{R}, \hat{R}^*)$, with mutually conjugated 2×2 blocks. Therefore, only this block, \hat{R} , is given in the table 2.

The described technique leads to two new types of dispersions (figure 1; crossings are taken at $E = 0$). The first one is PF, with four bands (obtained for $u, v = \pm 1$):

$$E_{v,u}(\mathbf{q}) = v\sqrt{aq_1^2 + cq_2^2 + ub|q_1q_2|}. \quad (3.1a)$$

The expression under the square root is non-negative since a, b and c are positive quantities (functions of v_{pq}^i) such that $b^2 - 4ac < 0$. For quadratic layer groups (54, 56, 58, 60) $c = a$, and above dispersion degenerates to the isotropic one $E_{v,u} = v\sqrt{aq^2 + ub|q_1q_2|}$. Two groups, 29 and 33, enforce $b^2 - 4ac = 0$, hosting thus FT dispersions (with bands counted by $u, v = \pm 1$):

$$E_{v,u}(\mathbf{q}) = v|f|q_1| + ug|q_2||, \quad (3.1b)$$

with f, g positive quantities, also functions of v_{pq}^i . Note that on the other side, the limit $b \rightarrow 0^+$ gives Dirac dispersion.

3.2. Density of states

Dispersion (3.1), differing from the well-known Dirac, semi-Dirac or quadratic, impose specific physical properties. In this context, one must take into account the range of validity of these forms, describing the realistic band structures only in the vicinity of high-symmetry point. In particular, corresponding density of states (DOS) near $E = 0$ are:

$$\rho_{\text{PF}}^{\text{SOC}} = \frac{2|E|}{\pi\sqrt{4ac - b^2}}, \quad (3.2a)$$

$$\rho_{\text{FT}}^{\text{SOC}} \approx \frac{L}{4\pi^2\sqrt{f^2 + g^2}}. \quad (3.2b)$$

Unlike to PF, but similarly to 3D nodal semimetals [39], exact calculation of DOS of FT is prevented due to the non-circular iso-energetic lines (figure 1). Thus, the last expression corresponds to realistic situations where the horizontal parts of band crossing lines are of the length L (this is an effective

range of approximation). In non-SOC case calculation of DOS gives doubled results (3.2), since each energy is spin degenerate, which is then decoupled from the orbital one. Non zero DOS of FT near $E = 0$ is in contrast to DOS of Dirac or PF dispersions being proportional to $|E|$, as well as to semi-Dirac which is proportional to $\sqrt{|E|}$. This affects many properties, to mention only charge and spin transport. Further, it can be shown that the electron effective mass, obtained from band curvatures, for all dispersions (3.1) vanishes. Let us emphasize that the higher order terms, neglected in derivation cannot change the obtained band topology (figure 1), though may distort bands slightly.

3.3. Symmetry breaking

Despite the obtained dispersions are essential, i.e. resistant to symmetry preserving perturbation, an interesting additional insight is gained by considering symmetry breaking. Herein, taking into account group-subgroup relations, we discuss the possibilities of robustness or switching between various dispersions at the same BZ-point by lowering the symmetry, e.g. due to strain. It is expected that decreasing the number of symmetry elements leads to relaxing the constraints imposed on Hamiltonians, and consequently increasing (or preserving) the number of independent parameters. In this context, taking into account the number of non-zero parameters v_{pq}^i of (2.5) given in table 1, it is meaningful to consider the transitions from FT to anisotropic PF, as well as from isotropic PF to FT, when the symmetry is lowered. Precisely, the allowed four-band model Hamiltonian diagonalizing in PF dispersion have six real independent parameters, which are reduced to three for quadratic groups; similarly, there are 4 real independent Hamiltonian parameters for FT. Before proceeding, let us take a brief look into the robustness of FT and PF.

Regarding groups 29 and 33 supporting FT dispersion, symmetry reduction in which either nonsymmorphic glide plane or screw axis (but not both) is retained causes that FT at the Y point splits into two non-degenerate conical dispersions. Opposite out-of-plane shifts of the adjacent nuclei positioned

Table 2. Allowed irreducible co-representations: for each group and corresponding HSP, the generators are listed, and the block-diagonal part \hat{R} of double valued co-representation \hat{D} representing these generators (in the same order). Here, $C_{n\hat{n}}$ is rotation for $2\pi/n$ around axis \hat{n} (which is $\hat{x}, \hat{y}, \hat{z}$, or $\hat{c} = \frac{1}{\sqrt{2}}(\hat{x} + \hat{y})$), $m_{\hat{n}}$ is vertical mirror plane which contains \hat{n} axis, m_h is horizontal mirror plane, and $S_n = C_{n\hat{z}}m_h$.

Group	HSP	Generators		\hat{R}			
21	S	$(C_{2\hat{x}} \frac{1}{2}0)$	$(C_{2\hat{y}} 0\frac{1}{2})$	$\hat{\sigma}_3$	$\hat{\sigma}_1$		
25	S	$(m_{\hat{x}} \frac{1}{2}0)$	$(m_{\hat{y}} 0\frac{1}{2})$	$\hat{\sigma}_3$	$\hat{\sigma}_1$		
28	Y	$(I 10)$	$(C_{2\hat{y}} 0\frac{1}{2})$	$m_{\hat{y}}$	$\hat{\sigma}_0$	$-\hat{\sigma}_3$	$-i\hat{\sigma}_2$
28	S	$(I 10)$	$(C_{2\hat{y}} 0\frac{1}{2})$	$m_{\hat{y}}$	$-\hat{\sigma}_0$	$-\hat{\sigma}_3$	$-i\hat{\sigma}_2$
29	Y	$(I 10)$	$(C_{2\hat{y}} 0\frac{1}{2})$	m_h	$\hat{\sigma}_0$	$-\hat{\sigma}_3$	$-i\hat{\sigma}_2$
29	S	$(I 10)$	$(C_{2\hat{y}} 0\frac{1}{2})$	m_h	$-\hat{\sigma}_0$	$-\hat{\sigma}_3$	$-i\hat{\sigma}_2$
30	Y	$(I 10)$	$(m_{\hat{y}} 0\frac{1}{2})$	$C_{2\hat{y}}$	$\hat{\sigma}_0$	$-\hat{\sigma}_3$	$-i\hat{\sigma}_2$
30	S	$(I 10)$	$(m_{\hat{y}} 0\frac{1}{2})$	$C_{2\hat{y}}$	$-\hat{\sigma}_0$	$-\hat{\sigma}_3$	$-i\hat{\sigma}_2$
32	Y	$(I 10)$	$(m_h \frac{1}{2}\frac{1}{2})$	$m_{\hat{y}}$	$\hat{\sigma}_0$	$-\hat{\sigma}_3$	$-i\hat{\sigma}_2$
33	Y	$(m_h \frac{1}{2}0)$	$(C_{2\hat{y}} 0\frac{1}{2})$		$i\hat{\sigma}_3$	$\hat{\sigma}_1$	
34	Y	$(I 10)$	$(m_h \frac{1}{2}\frac{1}{2})$	$C_{2\hat{y}}$	$\hat{\sigma}_0$	$-\hat{\sigma}_3$	$-i\hat{\sigma}_2$
54	M	$(I 10)$	$(C_{2\hat{c}} \frac{1}{2}\frac{1}{2})$	$C_{4\hat{z}}$	$-\hat{\sigma}_0$	$-i\hat{\sigma}_2$	$e^{-i\frac{3\pi}{4}}$ diag(1, i)
56	M	$(I 10)$	$(m_{\hat{c}} \frac{1}{2}\frac{1}{2})$	$C_{4\hat{z}}$	$-\hat{\sigma}_0$	$-i\hat{\sigma}_2$	$e^{-i\frac{3\pi}{4}}$ diag(1, i)
58	M	$(I 10)$	$(m_{\hat{c}} \frac{1}{2}\frac{1}{2})$	S_4	$-\hat{\sigma}_0$	$-i\hat{\sigma}_2$	$e^{-i\frac{3\pi}{4}}$ diag(1, i)
60	M	$(I 10)$	$(C_{2\hat{c}} \frac{1}{2}\frac{1}{2})$	S_4	$-\hat{\sigma}_0$	$-i\hat{\sigma}_2$	$e^{-i\frac{3\pi}{4}}$ diag(1, i)

in the mirror plane, transforms mirror into a glide plane, while doubling the lattice constant; this in turn halves primitive vector \mathbf{k}_1 of the reciprocal lattice. Group 29 reduces to 33 and the S point in 29 becomes Y point in 33. Consequently, FT in Y and S points in 29 are robust against lowering the symmetry to group 33. Similarly, concerning the PF, any homogeneous stretching along \mathbf{a}_1 or \mathbf{a}_2 axis deforms square primitive cell to rectangular, reducing the symmetries of layer groups 54 and 58 (56 and 60) to the group 21 (25) and causes PF to change from isotropic to anisotropic form, which implies direction-dependent electronic and related properties.

Since PF is a generalized form of FT, one could expect that the parameters of these dispersions can be interrelated by tuning. However, continuous transformation from FT to PF at the same point of the BZ is not possible, since neither of groups supporting FT is a subgroup of any of groups allowing PF, nor vice-versa. The expression (3.2a) for DOS of PF shows that the changing parameters such that PF approaches to FT results in a singularity at zero energy. In the other words, if opposite would hold, arbitrarily small displacements of nuclei, being sufficient to lower the symmetry, would cause a jump of (graphene-like) negligible DOS of PF to a finite and constant DOS of FT, which we found unlikely. At the same time, such obstruction from DOS does not forbid the transition between Dirac (double degenerate cones with four-fold degenerate point) and PF, nor it forbids splitting of FT and PF into two non-degenerate conical dispersions (with double degenerate point).

Following the above arguments, it is expected that transition from Dirac cone to PF may be realized by lowering the symmetry, since Dirac dispersions has less independent parameters than PF. According to [5] Dirac semimetals in time-reversal invariant two-dimensional systems with strong SOC are possible in nonsymmorphic groups with inversion symmetry. E.g. let us consider the layer group 46 ($pmmn$), hosting Dirac cones

at X , Y and S HSPs (the BZ is the same as this one given on the left panel in figure 2). It is expected that the violation of the inversion symmetry leads to Weyl points or node [5]. However, listing all subgroups, it turns out that the two of the subgroups, 32 and 21, actually host PF in the points Y and S , respectively. Indeed, in [46], using spinfull tight-binding model with four sites (with s-orbitals) per unit cell, authors show that at fillings 2, 6, system invariant under double layer group 21 is semimetal, which hosts one fourfold degenerate and four Weyl points. A plethora of such cases, where groups allowing PF from the table 1 are subgroups of symmetry groups of Dirac semimetals, indicates candidates for transitions between centrosymmetric and noncentrosymmetric crystals with protected four-fold band crossing point. Moreover, the existence of such essential fourfold degenerate point simultaneously with double degenerate Weyl points in the same system, makes that the layers from our list represent possible two-dimensional materials suitable for the study of their interplay.

3.4. Material realization

Despite the fabrication of freestanding layers is not always feasible, the above theoretical predictions required material realizations, or at least numerical simulations. To find realistic material with layer groups from table 1 we searched the list [41] of 3D layered materials, synthesis of which has been reported in the literature. In the table 3 we listed potential material candidates with symmetry groups allowing the predicted peculiar dispersions. These are laboratory fabricated 3D crystals with layered structures, which could be easily or potentially exfoliated into layers.

It is interesting to single out our group-theoretical findings indicated that dispersions (3.1) are not preserved when SOC is neglected, except for the LDG 33, which supports FT dispersion also in that case [29]. Inclusion of SOC moves FT from

Table 3. Material candidates: layered systems with symmetry groups hosting the dispersions (3.1). Layer and corresponding space groups are listed for materials given by a formula and materials project ID. Abbreviations EE and PE stand for easily and potentially exfoliable, respectively, according to [41].

Layer group	Space group	Formula	ID	EE/PE		
21	$p2_12_12$	18	$P2_12_12$	As ₂ SO ₆	mp-27230	EE
				MgMoTeO ₆	mp-1210722	EE
25	$pba2$	32	$Pba2$	Au ₂ Se ₂ O ₇	mp-28095	EE
				Re ₂ S ₂ O ₁₃ -I	mp-974650	EE
28	$pm2_1b$	26	$Pmc2_1$	TIP ₅	mp-27411	EE
				KO ₂ H ₄ F	mp-983327	PE
				NaGe ₃ P ₃	mp-1104707	PE
29	$pb2_1m$	26	$Pmc2_1$	WO ₂ Cl ₂	mp-32539	EE
32	$pm2_1n$	31	$Pmn2_1$	CuCOCl	mp-562090	EE
33	$pb2_1a$	29	$Pca2_1$	BiIO ₄	mp-1191266	PE
				KPSe ₆	mp-18625	EE
58	$p\bar{4}2_1m$	113	$P\bar{4}2_1m$	LiReO ₂ F ₄	mp-554108	EE

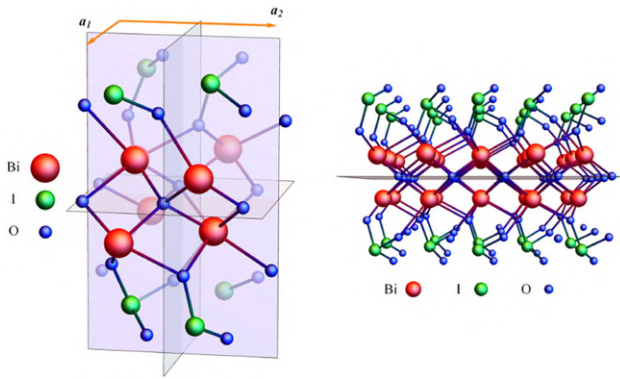


Figure 3. Crystal structure of BiIO₄ mono-layer: elementary cell (left) and a part of layer (right).

BZ corners to the Y -point. The material BiIO₄ belongs to corresponding space group 29 and has layers parallel to the $y = 0$ plane. Consequently, it should exfoliate to layer group 33 so we choose it for further DFT investigations, as an example of achievements of our theory. Since IRs from table 1 are the only extra IRs in these BZ points, the dispersions (3.1) are unavoidable for crystals with symmetry of these groups. On the other hand, the position of Fermi level cannot be determined solely by symmetry arguments, nor it can be guaranteed that no other bands cross or touch the Fermi level.

We determined crystal (figure 3) and band structure (figure 4) of BiIO₄ mono-layer configuration using DFT calculations: full relaxation and bands calculations were performed by QUANTUM ESPRESSO software package [42], full relativistic PAW pseudopotentials [43, 44], with the Perdew–Burke–Ernzerhof exchange–correlation functional [45]. The energy cutoff for electron wavefunction and charge density of 47 Ry and 476 Ry were chosen, respectively. The band structures were found in 500 k -points on selected path, and 2500 k -points for 2D band structure plots in the vicinity of HSPs.

Crystal structure of mono-layer is shown in figure 3. It belongs to rectangular lattice of the group 33, with nearly equal $a_1 = 0.566$ nm and $a_2 = 0.575$ nm. Band structure of BiIO₄

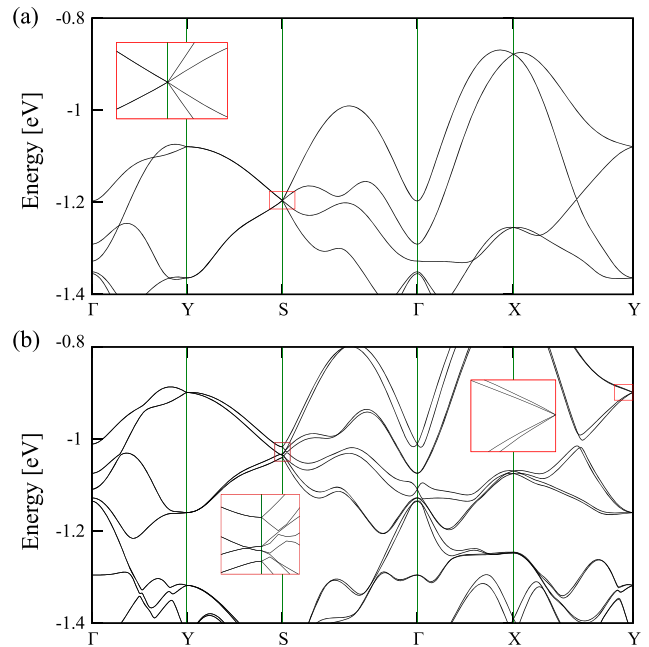


Figure 4. Band structure of BiIO₄ mono-layer without SOC (top) and with SOC (bottom), with insets showing magnified FT and split FT dispersions. The Fermi level is set to zero eV.

mono-layer with and without SOC is shown in figure 4. It turns out that the system is insulating in undoped and ungated regime. The closest to Fermi level FT state is at -0.9 eV. When SOC is neglected energy at the point S is eightfold degenerate (including spin), which gives electron filling of $8n$ that is necessary for insulating systems [40]. With inclusion of SOC the eightfold spinfull degeneracy at S is lifted, but sets of eight non-degenerate bands each, form *cat's cradle* structure along ΓX line, as predicted in reference [46]. This gives again electron filling of $8n$ [46, 47]. Our electron filling of 184, derived from DFT calculations, is indeed divisible by 8. Electron filling for DLG 33 prevents FT to be the only dispersion at the Fermi level, while for remaining groups in table 1 the filling condition necessary for Fermi surface consisting of isolated points is $\nu = 4n + 2$.

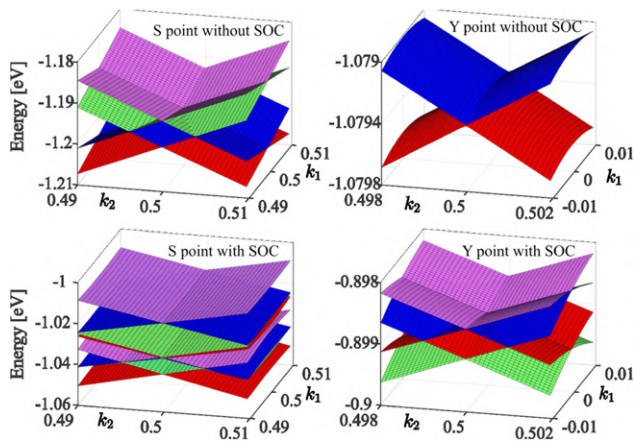


Figure 5. Band structures of BiIO₄ mono-layer without and with SOC near points *S* and *Y*. Inclusion of SOC turns FT dispersion into nodal lines in *S*, and degenerate Dirac line into FT in *Y*.

Behavior of FT states with inclusion of SOC is shown in figure 5. In non-SOC case, two pairs of Dirac lines meet at the point *S* and form the FT states. SOC splits eightfold degenerate band at *S* into four double degenerate ones. Near point *Y*, SOC splits fourfold spinfull degenerate Dirac line into one FT state. Since SOC strength is proportional to the fourth power of the atomic number [48], heavy elements in the material induced observable splitting.

4. Conclusions

Characterized by band crossings (touching) points (lines) at Fermi level from which energies disperse linearly, nodal metals/semimetals take an important role in investigations of various topological properties of crystals. Among them, symmetry-enforced ones represent a class of materials hosting such dispersions in HSPs due to increased degeneracy. In the language of group theory, while the spinless case is described by the ordinary group of geometrical transformations, the spinfull situation, when system is robust on spin-orbit perturbation, needs double groups. Additional inclusion of TRS leads to gray magnetic ordinary or double group. The increased degeneracy of energy is enabled by higher dimensional allowed irreducible (co)representations of the corresponding underlying crystal symmetry.

New fermions in 2D materials revealed by application of full gray double layer group symmetry contribute to the interesting physical phenomena of layered systems: two new types of dispersions beyond Dirac, PF and FT, accompany the fourfold degeneracy of bands in high-symmetry points. Our findings single out list of twelve nonsymmorphic and non-centrosymmetric layer groups that support such unusual linear electronic dispersions. As the method is not based on the topological mechanism (invoking nonsymmorphic symmetry), the result is general, verifying *a posteriori* the necessity of nonsymmorphic elements for the considered dispersions. Providing this list, numerical simulations aimed to find material realizations of the peculiar dispersions are facilitated, which is of a great importance to achieve corresponding physical properties. PF dispersion occurs in ten groups; in particular, there

are single isolated HSP hosting it in the groups $p2_12_12$, $pba2$ (point *S*), $pm2_1n$, $pb2n$ (*Y*), and $p42_12$, $p4bm$, $p42_1m$, $p4b2$ (*M*), while the groups $pm2_1b$ and $pb2b$ have two such points (*Y*, *S*). On the other hand, the FT type of dispersion in the group $pb2_1a$ is hosted in single (*Y*), and in the group $pb2_1m$ in two HSPs (*Y*, *S*).

Particularly interesting are groups $pb2_1a$, supporting FT dispersion both with and without SOC, as well as $pba2$ and $p4bm$, which are also wallpaper groups, preserved even when perpendicular, homogenous electric field is applied (e.g. due to gating). Moreover, coexistence of degenerate point and lines at the same energy in FT dispersion may lead to some new phenomena. FT dispersion has constant contribution to DOS, manifested as a plateau nearby zero energy in FT. This may be important in technological applications, especially when electron and/or spin transport are looked for, like materials for solar cells [49], spintronic etc. On the contrary, PF dispersion, similarly to Dirac ones, contributes by linear DOS with no states on zero energy. It has both isotropic and anisotropic forms which may be continuously transformed into each other by crystal deformations.

Our numerical calculations show that layered BiIO₄ 3D crystal, exfoliates to stable mono-layer having a symmetry group from our list. Band structure of BiIO₄ mono-layer confirms theoretical prediction, but further efforts are necessary in order to place the Fermi level at right energy.

Acknowledgments

Authors VD, AŠ and JP acknowledge funding provided by the Institute of Physics Belgrade, through the Grant by the Ministry of Education, Science and Technological Development of the Republic of Serbia. NL, BN and MD were supported by the Serbian Ministry of Education, Science and Technological Development under Project Number OI171035. DFT calculations were performed using computational resources at Johannes Kepler University, Linz, Austria.

ORCID iDs

V Damjanović <https://orcid.org/0000-0001-7517-6439>
 N Lazić <https://orcid.org/0000-0002-3634-0301>
 A Šolajić <https://orcid.org/0000-0002-0553-0858>
 J Pešić <https://orcid.org/0000-0002-8600-7187>
 B Nikolić <https://orcid.org/0000-0002-7241-3248>
 M Damjanović <https://orcid.org/0000-0003-2806-253X>

References

- [1] Gupta S, Kutana A and Yakobson B I 2018 Dirac cones and nodal line in borophene *J. Phys. Chem. Lett.* **9** 2757–62
- [2] Zhang Y, Kang J, Zheng F, Gao P-F, Zhang S-L and Wang L-W 2019 Borophosphene: a new anisotropic Dirac cone mono-layer with a high Fermi velocity and a unique self-doping feature *J. Phys. Chem. Lett.* **10** 6656–63
- [3] Zhang L Z, Wang Z F, Wang Z M, Du S X, Gao H-J and Liu F 2015 Highly anisotropic Dirac fermions in square graphynes *J. Phys. Chem. Lett.* **6** 2959–62

- [4] Fang C, Gilbert M J, Dai X and Andrei Bernevig B 2012 Multi-Weyl topological semimetals stabilized by point group symmetry *Phys. Rev. Lett.* **108** 266802
- [5] Young S M and Kane C L 2015 Dirac semimetals in two dimensions *Phys. Rev. Lett.* **115** 126803
- [6] van Miert G and Smith C M 2016 Dirac cones beyond the honeycomb lattice: a symmetry-based approach *Phys. Rev. B* **93** 035401
- [7] Wang J 2017 Antiferromagnetic Dirac semimetals in two dimensions *Phys. Rev. B* **95** 115138
- [8] Kim J, Baik S S, Jung S W, Sohn Y, Ryu S H, Choi H J, Yang B-J and Kim K S 2017 Two-dimensional Dirac fermions protected by space-time inversion symmetry in black phosphorus *Phys. Rev. Lett.* **119** 226801
- [9] Young S M and Wieder B J 2017 Filling-enforced magnetic Dirac semimetals in two dimensions *Phys. Rev. Lett.* **118** 186401
- [10] Kawarabayashi T, Aoki H and Hatsugai Y 2019 Topologically protected doubling of tilted Dirac fermions in two dimensions *Phys. Status Solidi B* **256** 1970025
- [11] Mañes J L 2012 Existence of bulk chiral fermions and crystal symmetry *Phys. Rev. B* **85** 155118
- [12] Damljanović V and Gajić R 2016 Existence of Dirac cones in the Brillouin zone of diperiodic atomic crystals according to group theory *J. Phys.: Condens. Matter* **28** 085502
- [13] Damljanović V and Gajić R 2016 Addendum to existence of Dirac cones in the Brillouin zone of diperiodic atomic crystals according to group theory *J. Phys.: Condens. Matter* **28** 439401
- [14] Park S and Yang B-J 2017 Classification of accidental band crossings and emergent semimetals in two-dimensional noncentrosymmetric systems *Phys. Rev. B* **96** 125127
- [15] Wieder B J, Bradlyn B, Wang Z, Cano J, Kim Y, Kim H-S D, Rappe A M, Kane C L and Andrei Bernevig B 2018 Wallpaper fermions and the nonsymmorphic Dirac insulator *Science* **361** 246–51
- [16] Wieder B J, Kim Y, Rappe A M and Kane C L 2016 Double Dirac semimetals in three dimensions *Phys. Rev. Lett.* **116** 186402
- [17] Bradlyn B, Cano J, Wang Z, Vergniory M G, Felser C, Cava R J and Andrei Bernevig B 2016 Beyond Dirac and Weyl fermions: unconventional quasiparticles in conventional crystals *Science* **353** aaf5037
- [18] Zhu Z, Winkler G W, Wu Qian, Ju L and Alexey A 2016 Soluyanov. Triple point topological metals *Phys. Rev. X* **6** 031003
- [19] Wang Z, Alexandradinata A, Cava R J and Andrei Bernevig B 2016 Hourglass fermions *Nature* **532** 189–94
- [20] Lv B Q *et al* 2017 Observation of three-component fermions in the topological semimetal molybdenum phosphide *Nature* **546** 627–31
- [21] Barik R K, Shinde R and Singh A K 2018 Multiple triple-point fermions in Heusler compounds *J. Phys.: Condens. Matter* **30** 375702
- [22] Yang Y *et al* 2019 Topological triply degenerate point with double Fermi arcs *Nat. Phys.* **15** 645–9
- [23] Ma J *et al* 2017 Experimental evidence of hourglass fermion in the candidate nonsymmorphic topological insulator KHgSb *Sci. Adv.* **3** e1602415
- [24] Wang S-S, Liu Y, Yu Z-M, Sheng X-L and Yang S A 2017 Hourglass Dirac chain metal in rhenium dioxide *Nat. Commun.* **8** 1844
- [25] Singh B, Ghosh B, Su C, Lin H, Agarwal A and Bansil A 2018 Topological hourglass Dirac semimetal in the nonpolar phase of Ag_2BiO_3 *Phys. Rev. Lett.* **121** 226401
- [26] Novoselov K S, Geim A K, Morozov S V, Jiang D, Zhang Y, Dubonos S V, Grigorieva I V and Firsov A A 2004 Electric field effect in atomically thin carbon films *Science* **306** 666–9
- [27] Kim J *et al* 2015 Observation of tunable band gap and anisotropic Dirac semimetal state in black phosphorus *Science* **349** 723–6
- [28] Wang Z M 2014 *MoS₂ Materials, Physics and Devices* (Berlin: Springer)
- [29] Damljanović V, Popov I and Gajić R 2017 Fortune teller fermions in two-dimensional materials *Nanoscale* **9** 19337–45
- [30] Kopciszynski M, Krawiec M, Żurawek L and Zdyb R 2020 Experimental evidence of a new class of massless fermions *Nanoscale Horiz.* **5** 679–82
- [31] Nguyen S D, Yeon J, Kim S-H and Shiv Halasyamani P 2011 $\text{BiO}(\text{IO}_3)$: a new polar iodate that exhibits an Aurivillius-type $(\text{Bi}_2\text{O}_2)^{2+}$ layer and a large SHG response *J. Am. Chem. Soc.* **133** 12422–5
- [32] Cornwell J F 1984 *Group Theory in Physics* (New York: Academic)
- [33] Elcoro L *et al* 2017 Double crystallographic groups and their representations on the Bilbao Crystallographic Server *J. Appl. Crystallogr.* **50** 1457–77
- [34] Damljanović M and Milošević I 2015 Full symmetry implementation in condensed matter and molecular physics—modified group projector technique *Phys. Rep.* **581** 1–43
- [35] Litvin D B and Wike T R 1991 *Character Tables and Compatibility Relations of the Eighty Layer Groups and Seventeen Plane Groups* (New York: Plenum)
- [36] Dresselhaus M S, Dresselhaus G and Jorio A 2008 *Group Theory* (Berlin: Springer)
- [37] Kopsky V and Litvin D B 2002 *International Tables of Crystallography Volume E: Subperiodic Groups* (Dordrecht: Kluwer)
- [38] Hahn T 2005 *International Tables of Crystallography Volume A: Space-Group Symmetry* (Berlin: Springer)
- [39] Burkov A A, Hook M D and Leon B 2011 Topological nodal semimetals *Phys. Rev. B* **84** 235126
- [40] Watanabe H, Po H C, Zaletel M P and Vishwanath A 2016 Filling-enforced gaplessness in band structures of the 230 space groups *Phys. Rev. Lett.* **117** 096404
- [41] Mounet N *et al* 2018 Two-dimensional materials from high-throughput computational exfoliation of experimentally known compounds *Nat. Nanotechnol.* **13** 246–52
- [42] Giannozzi P *et al* 2009 QUANTUM ESPRESSO: a modular and open-source software project for quantum simulations of materials *J. Phys.: Condens. Matter* **21** 395502
- [43] Blöchl P E 1994 Projector augmented-wave method *Phys. Rev. B* **50** 17953–79
- [44] Kresse G and Joubert D 1999 From ultrasoft pseudopotentials to the projector augmented-wave method *Phys. Rev. B* **59** 1758–75
- [45] Perdew J P, Burke K and Ernzerhof M 1996 Generalized gradient approximation made simple *Phys. Rev. Lett.* **77** 3865–8
- [46] Wieder B J and Kane C L 2016 Spin-orbit semimetals in the layer groups *Phys. Rev. B* **94** 155108
- [47] Watanabe H, Po H C, Vishwanath A and Zaletel M 2015 Filling constraints for spin-orbit coupled insulators in symmorphic and nonsymmorphic crystals *Proc. Natl Acad. Sci.* **112** 14551–6
- [48] Yang S A 2016 Dirac and Weyl materials: fundamental aspects and some spintronic applications *SPIN* **06** 1640003
- [49] Boriskina S, Zhou J, Ding Z and Chen G 2018 Efficiency limits of solar energy harvesting via internal photoemission in carbon materials *Photonics* **5** 4



An example of diperiodic crystal structure with semi-Dirac electronic dispersion

V. Damljanović¹

Received: 30 October 2017 / Accepted: 14 June 2018
© Springer Science+Business Media, LLC, part of Springer Nature 2018

Abstract

In the physics of two-dimensional materials, notion semi-Dirac dispersion denotes electronic dispersion which is Dirac-like along one direction in the reciprocal space, and quadratic along the orthogonal direction. In our earlier publication (Damljanović and Gajić in *J Phys Condens Matter* 29:185503, 2017) we have shown that certain layer groups are particularly suitable for hosting semi-Dirac dispersion in the vicinity of some points in the Brillouin zone (BZ). In the present paper we have considered tight-binding model up to seventh nearest neighbors, on a structure belonging to layer group $Dg5$. According to our theory, this group should host semi-Dirac dispersion at A and B points in the BZ. The structure has four atoms per primitive cell, and it is isostructural with sublattice occupied by phosphorus atoms in the layered material SnPSe_3 . While the first order perturbation theory of double degenerate level gives two pairs of semi-Dirac cones and correctly reproduces dispersion in the Dirac-like direction, exact diagonalisation of four-by-four tight-binding Hamiltonian shows node lines caused by accidental degeneracy in the band structure. We discuss these degeneracies in the context of von Neumann–Wigner theorem, and conclude that although dispersion remains semi-Dirac in the exact diagonalisation method, the band structure does not necessarily form cones. In order to get full picture of behavior of bands in the vicinity of semi-Dirac points, first order perturbation theory may not be sufficient and one may need higher order corrections.

Keywords Semi-Dirac dispersion · Two-dimensional materials · Layer groups · Tight-binding model

This article is part of the Topical Collection on Focus on Optics and Bio-photonics, Photonica 2017.

Guest Edited by Jelena Radovanovic, Aleksandar Krmpot, Marina Lekic, Trevor Benson, Mauro Pereira, Marian Marciniak.

✉ V. Damljanović
damlja@ipb.ac.rs

¹ Institute of Physics Belgrade, University of Belgrade, Pregrevica 118, Belgrade, Serbia

1 Introduction

Two-dimensional (2D) materials are materials that are periodic in two spatial directions but finite in the third, orthogonal direction. These materials gain particular attention after discovery of graphene, a one atom thick layer of carbon atoms arranged in a honeycomb lattice. In contrast to graphene, in which all atoms belong to a single plane, buckled silicene and germanene for example, occupy Wyckoff positions with unequal z -coordinates. Existence of massless electrons whose dynamics is described by Dirac (Weyl) equation is among notable properties of graphene and related, so called Dirac, materials.

Besides Dirac materials, there is another class of 2D materials in which electronic dispersion is Dirac-like (linear) along some direction in the 2D Brillouin zone (BZ), and quadratic along the orthogonal direction. Such semi-Dirac dispersion supports both massless and massive electrons at the same point of the BZ, thus giving rise to highly anisotropic material properties. Using density functional theory (DFT), semi-Dirac dispersion has been predicted in TiO_2/VO_2 nanostructures (Pardo and Pickett 2009, 2010), in silicene oxide (Zhong et al. 2017) and in square selenene and tellurene (Xian et al. 2017). A tight-binding model show semi-Dirac dispersion in phosphorene under strain for certain critical values of hopping parameters (Duan et al. 2016). First experimental realization of material with semi-Dirac dispersion was reported in 2015. It was demonstrated that few-layer black phosphorus doped with potassium posses semi-Dirac dispersion at the BZ center for certain level of doping (Kim et al. 2015). The behavior of semi-Dirac fermions in external magnetic field and consequences that this dispersion imposes on Klein tunneling is examined in more detail in Banerjee et al. (2009) and Banerjee and Pickett (2012). Evolution of Hofstadter spectrum on a square lattice with the application of an on-site uniaxial staggered potential shows merging of two Dirac points into a semi-Dirac one (Deplace and Montambaux 2010). Analysis of semi-Dirac systems based on DFT show that in some cases, spin-orbit coupling (SOC) can open a small gap and can lead to topologically non-trivial bands, which contribute to non-zero total Chern number (Huang et al. 2015). Such systems are then suitable for demonstration of quantum Hall effect. Analogous conclusion is derived for semi-Dirac systems under laser light illumination (Saha 2016). On the other hand, Narayan (2015) concluded that for semi-Dirac semimetals circularly polarized light does not open a band gap. The influence of electronic correlations on semi-Dirac systems was also investigated. It was found by renormalization group theory, that interplay of Coulomb interaction between electrons and disorder can drive the semi-Dirac system to non-Fermi-liquid behavior (Zhao et al. 2016). Similarly, approximate solution of Schwinger–Dyson equation show that moderate Coulomb interaction can induce excitonic gap opening in semi-Dirac band structure (Wang et al. 2017). Anisotropic properties of semi-Dirac materials have potential applications in electronics (Mannhart and Schlom 2010). For example, a p – n junction made from such material would have negative differential conductance for certain bias voltage (Saha et al. 2017).

Group theory is a powerful tool in predicting various types of electronic dispersions. In some cases mere belonging of a crystal to some space groups, leads unavoidably to certain dispersion. For example, Mañes (2012) has found sufficient conditions for existence of bulk chiral fermions in 3D single crystals and has provided a list of space groups that host such dispersion in the vicinity of given points of the BZ. The non-symmorphic space group $P2_12_12_1$ (No. 19 in notation of Hahn 2005) belongs to Mañes list. Geilhufe et al. (2017) have searched the Organic Materials Database and have found six compounds that belong to this space group and in addition have only Dirac points at the Fermi level.

Another search was performed within reported DFT crystal structures collected in Materials Project database (Cheon et al. 2017). This search was for 3D crystal structures that consist of weakly interacting layers and hence, are suitable for obtaining 2D forms by e.g. exfoliation. Recently a list of four layer (diperiodic) groups that host semi-Dirac dispersion was given (Damljanović and Gajić 2017). The corresponding theory was formulated for non-magnetic, 2D materials with negligible SOC.

In this paper we have searched a list of layered 3D materials (Cheon et al. 2017), for structures that consist of layers belonging to layer group $p11b$ ($Dg5$ in notation of Kopsky and Litvin 2002), with layers periodically repeated along the z -axis. The layer group $p11b$ hosts semi-Dirac dispersion at A and B points of the BZ (Damljanović and Gajić 2017). In what follows, we have considered a tight-binding model from s -orbitals on a system isostructural to phosphorus sublattice in the single layer of material SnPSe_3 that belongs to the list (Cheon et al. 2017).

2 Method and results

Space group $P1c1$ (No. 7) is obtained by periodic repetition of layer group $Dg5$ along the axis that is perpendicular to diperiodic plane. On the other hand, diperiodic plane is perpendicular to the y -axis in the space group $P1c1$. For these reasons we have searched 3D layered materials given in Cheon et al. (2017), belonging to the space group $P1c1$, such that layers are parallel to the unique glide plane. We have found following five materials whose structures satisfy these requirements: Al_2CdCl_8 (Materials Project No. mp-28361 Bergerhoff et al. 1983; Staffel and Mayer 1987), $\text{Cr}(\text{PO}_3)_5$ (mp-705019 Bergerhoff et al. 1983; Jain et al. 2011; Hautier et al. 2011; El-Horr and Bagieu Beucher 1986), $\text{LiTi}(\text{PO}_3)_5$ (mp-684059 Bergerhoff et al. 1983; Jain et al. 2011; Hautier et al. 2011; El-Horr and Bagieu Beucher 1986), SnPSe_3 (mp-570370 Bergerhoff et al. 1983; Israel et al. 1998) and SnPS_3 (mp-13923 Bergerhoff et al. 1983; Dittmar and Schaefer 1974). If one would neglect SOC one would get semi-Dirac dispersion in these materials, irrespectively of the method used to calculate the band structure, as long as the approximation used is sufficiently fine (Damljanović and Gajić 2017). The inclusion of SOC would require analysis of double groups and it may be a topic of future research.

As an illustration, we will investigate electronic dispersion within a tight-binding model on a structure that belongs to layer group $Dg5$. In order to make the structure more realistic, we choose it to be isostructural with the sublattice of phosphorus ions in SnPSe_3 , a material whose stability was confirmed by DFT calculations (Bergerhoff et al. 1983; Israel et al. 1998). The crystal structure and corresponding BZ is shown on Fig. 1. The lattice parameters are 6.996 and 12.006 Å, while the oblique angle is 124.6°. The Wyckoff position $2a$ is occupied twice, with nuclei having (fractional) coordinates (0.12600, 0.56620, 2.83 Å) and (0.87540, 0.43600, 1.17 Å). The positions of other nuclei are determined by symmetry (Kopsky and Litvin 2002). Although our system is isostructural with phosphorus sublattice of SnPSe_3 , we do not assume that it is made from phosphorus atoms. We consider a tight-binding (LCAO MO) model from s -orbitals, in order to make the model simple. The internuclear distances and hopping integrals are given in the Table 1. The tight-binding Hamiltonian is (* denotes complex conjugation):

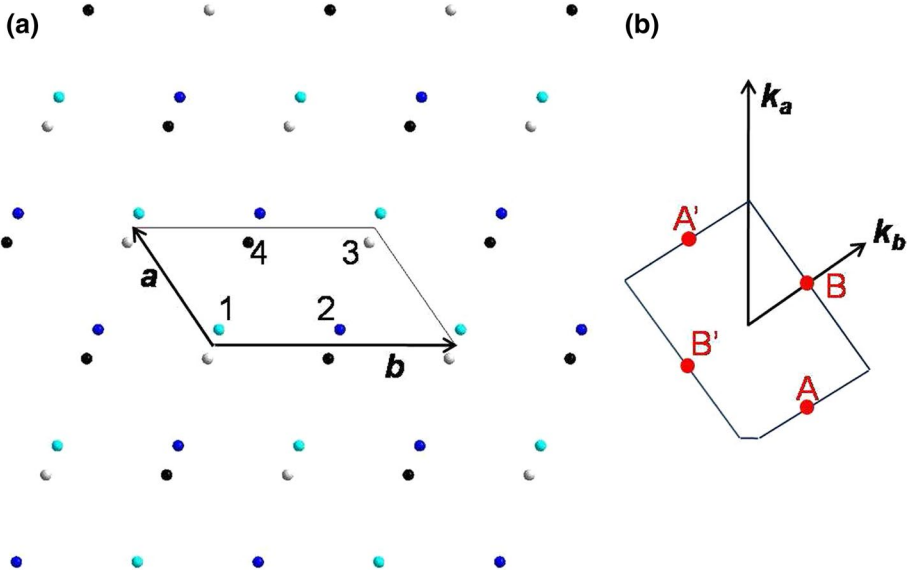


Fig. 1 **a** Crystal structure belonging to Dg_5 for the tight-binding model. Black parallelogram denotes primitive unit cell. All nuclei are of the same type. Height of nuclei above the drawing plane is denoted by colors: blue $+ 2.83 \text{ \AA}$, black $+ 1.17 \text{ \AA}$, gray $- 1.17 \text{ \AA}$, turquoise $- 2.83 \text{ \AA}$. **b** Corresponding Brillouin zone with basis vectors of the reciprocal lattice and positions of A and B points that host semi-Dirac dispersion. (Color figure online)

Table 1 Internuclear distances and corresponding hopping parameters for the structure from Fig. 1

Pair of nuclei	Internuclear distance (\AA)	Hopping integral
$\mathbf{r}_1, \mathbf{r}_1$	0	γ_{11}
$\mathbf{r}_3, \mathbf{r}_3$	0	γ_{33}
$\mathbf{r}_1, \mathbf{r}_3 - \mathbf{b} - \mathbf{a}$	2.2677	γ_{13}
$\mathbf{r}_1, \mathbf{r}_4$	6.0619	γ_{14}
$\mathbf{r}_3, \mathbf{r}_4$	6.4446	γ_{34}
$\mathbf{r}_3, \mathbf{r}_4 + \mathbf{b}$	6.4446	γ_{34}
$\mathbf{r}_1, \mathbf{r}_3 - \mathbf{b}$	6.4794	γ'_{13}
$\mathbf{r}_3, \mathbf{r}_4 - \mathbf{a}$	6.5389	γ'_{34}
$\mathbf{r}_3, \mathbf{r}_4 + \mathbf{a} + \mathbf{b}$	6.5389	γ'_{34}
$\mathbf{r}_1, \mathbf{r}_4 - \mathbf{a}$	6.9012	γ'_{14}
$\mathbf{r}_1, \mathbf{r}_1 + \mathbf{a}$	6.9960	γ'_{11}
$\mathbf{r}_1, \mathbf{r}_1 - \mathbf{a}$	6.9960	γ'_{11}
$\mathbf{r}_3, \mathbf{r}_3 + \mathbf{a}$	6.9960	γ'_{33}
$\mathbf{r}_3, \mathbf{r}_3 - \mathbf{a}$	6.9960	γ'_{33}

Other distances (higher neighbors of \mathbf{r}_1 or \mathbf{r}_3) are bigger than 7.8 \AA

$$H(\mathbf{k}) = \begin{pmatrix} \gamma_{11} + 2\gamma'_{11} \cos(\mathbf{k} \cdot \mathbf{a}) & 0 & \gamma_{13}e^{-i\mathbf{k} \cdot (\mathbf{a}+\mathbf{b})} + \gamma'_{13}e^{-i\mathbf{k} \cdot \mathbf{b}} & \gamma_{14} + \gamma'_{14}e^{-i\mathbf{k} \cdot \mathbf{a}} \\ 0 & \gamma_{11} + 2\gamma'_{11} \cos(\mathbf{k} \cdot \mathbf{a}) & \gamma_{14} + \gamma'_{14}e^{-i\mathbf{k} \cdot \mathbf{a}} & \gamma'_{13} + \gamma_{13}e^{-i\mathbf{k} \cdot \mathbf{a}} \\ \gamma_{13}e^{i\mathbf{k} \cdot (\mathbf{a}+\mathbf{b})} + \gamma'_{13}e^{i\mathbf{k} \cdot \mathbf{b}} & \gamma_{14} + \gamma'_{14}e^{i\mathbf{k} \cdot \mathbf{a}} & \gamma_{33} + 2\gamma'_{33} \cos(\mathbf{k} \cdot \mathbf{a}) & h_{34} \\ \gamma_{14} + \gamma'_{14}e^{i\mathbf{k} \cdot \mathbf{a}} & \gamma'_{13} + \gamma_{13}e^{i\mathbf{k} \cdot \mathbf{a}} & h_{34}^* & \gamma_{33} + 2\gamma'_{33} \cos(\mathbf{k} \cdot \mathbf{a}) \end{pmatrix}, \tag{1}$$

$$h_{34} = \gamma_{34}(1 + e^{i\mathbf{k} \cdot \mathbf{b}}) + \gamma'_{34}(e^{-i\mathbf{k} \cdot \mathbf{a}} + e^{i\mathbf{k} \cdot (\mathbf{a}+\mathbf{b})}). \tag{2}$$

We are interested in the electronic band structure in the vicinity of points $\mathbf{k}_A = (-\mathbf{k}_a + \mathbf{k}_b)/2$ and $\mathbf{k}_B = \mathbf{k}_b/2$. The band structure for certain ratios of hopping integrals is shown on Fig. 2. We can see in the vicinity of point (0, 0) the presence of dispersion which is Dirac-like along one direction in the BZ and quadratic along the perpendicular direction. In addition, we see that the band structure contains double spinless degenerate line (one line per each pair of bands) which is not caused by the TRS nor crystal symmetry.

To determine more precisely the exact type of dispersion in the vicinity of given BZ points, we calculate analytically the band structure, first by the perturbation theory of degenerate energy level and later exactly, by solving quartic equation. In order to simplify calculations we assume $\gamma'_{11} = \gamma'_{33} = \gamma'_{13} = \gamma'_{14} = \gamma'_{34} = 0$ and, although not required by symmetry, $\gamma_{11} = \gamma_{33}(= \gamma_1)$. The energies at both A and B points are $E_0 = \gamma_1 - \sqrt{\gamma_{13}^2 + \gamma_{14}^2}$ and $E'_0 = \gamma_1 + \sqrt{\gamma_{13}^2 + \gamma_{14}^2}$. Both E_0 and E'_0 are doubly degenerate. For the A-point we write $H(\mathbf{k}_A + \mathbf{q}) = H(\mathbf{k}_A) + H'$ and apply first order perturbation theory of degenerate levels E_0

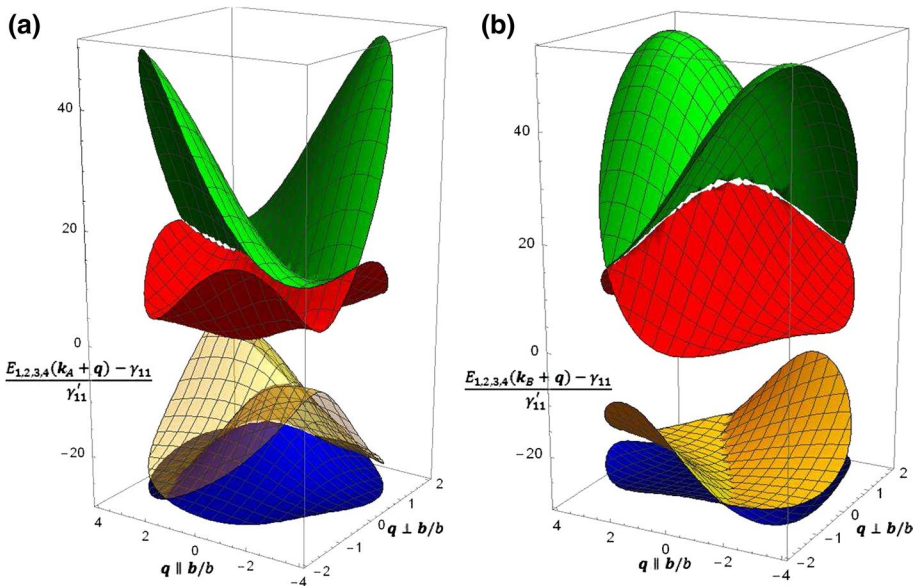


Fig. 2 The electronic band structure in the vicinity of A (a) and B (b) points of the BZ for $\gamma_{13}/\gamma'_{11} = 18$, $\gamma_{14}/\gamma'_{11} = 10.5$, $\gamma_{34}/\gamma'_{11} = 8$, $\gamma'_{13}/\gamma'_{11} = 6.5$, $\gamma'_{34}/\gamma'_{11} = 4.5$, $\gamma'_{14}/\gamma'_{11} = 2.5$, $\gamma'_{33}/\gamma'_{11} = 0.5$ and $(\gamma_{33} - \gamma_{11})/\gamma'_{11} = -0.5$. \mathbf{q} is in units $1/b$ in the direction parallel to \mathbf{b}/b , and in units $1/(\cos(34.6^\circ))$ in the direction perpendicular to \mathbf{b}/b . Coordinates of the A point in panel a, i.e. B point in panel b, are (0, 0)

and E'_0 , with $H' = H(\mathbf{k}_A + \mathbf{q}) - H(\mathbf{k}_A)$ being perturbation. We do the same for the B -point. The final result for the B -point is:

$$E_{1,2} \approx E'_0 - \frac{1}{2}C_2q_2'^2 \pm \frac{1}{2}\sqrt{u_2q_1'^2 + v_2q_2'^4}, \tag{3}$$

$$E_{3,4} \approx E_0 + \frac{1}{2}C_1q_2^2 \pm \frac{1}{2}\sqrt{u_1q_1^2 + v_1q_2^4}, \tag{4}$$

while for the A -point we obtain:

$$E_{1,2} \approx E'_0 - \frac{1}{2}C_1q_2^2 \pm \frac{1}{2}\sqrt{u_1q_1^2 + v_1q_2^4}, \tag{5}$$

$$E_{3,4} \approx E_0 + \frac{1}{2}C_2q_2'^2 \pm \frac{1}{2}\sqrt{u_2q_1'^2 + v_2q_2'^4}. \tag{6}$$

Here \mathbf{q} is a vector of small modulus, q_1, q_2, q'_1 and q'_2 are the projections of \mathbf{q} along vectors $\mathbf{e}_1, \mathbf{e}_2, \mathbf{e}_3$ and \mathbf{e}_4 , respectively. In addition:

$$u_{1,2} = \left[2 \frac{\gamma_{13}\gamma_{14}}{\sqrt{\gamma_{13}^2 + \gamma_{14}^2}} \mathbf{a} + \left(\frac{\gamma_{13}\gamma_{14}}{\sqrt{\gamma_{13}^2 + \gamma_{14}^2}} \mp \gamma_{34} \right) \mathbf{b} \right]^2, \tag{7}$$

$$v_{1,2} = 4 \frac{(\mathbf{a} \times \mathbf{b})^4 \gamma_{13}^6 \gamma_{14}^2 \gamma_{34}^2}{u_{1,2}^2 (\gamma_{13}^2 + \gamma_{14}^2)^2}, \tag{8}$$

$$C_{1,2} = \frac{(\mathbf{a} \times \mathbf{b})^2 \gamma_{13}^2}{u_{1,2} \sqrt{\gamma_{13}^2 + \gamma_{14}^2}} \left(\frac{\gamma_{13}^2 \gamma_{14}^2}{\gamma_{13}^2 + \gamma_{14}^2} + \gamma_{34}^2 \right), \tag{9}$$

$$\mathbf{e}_1 = \frac{2}{\sqrt{u_1}} \frac{\gamma_{13}\gamma_{14}}{\sqrt{\gamma_{13}^2 + \gamma_{14}^2}} \mathbf{a} + \frac{1}{\sqrt{u_1}} \left(\frac{\gamma_{13}\gamma_{14}}{\sqrt{\gamma_{13}^2 + \gamma_{14}^2}} - \gamma_{34} \right) \mathbf{b}, \tag{10}$$

$$\mathbf{e}_3 = \frac{2}{\sqrt{u_2}} \frac{\gamma_{13}\gamma_{14}}{\sqrt{\gamma_{13}^2 + \gamma_{14}^2}} \mathbf{a} + \frac{1}{\sqrt{u_2}} \left(\frac{\gamma_{13}\gamma_{14}}{\sqrt{\gamma_{13}^2 + \gamma_{14}^2}} + \gamma_{34} \right) \mathbf{b}, \tag{11}$$

$$\mathbf{e}_{2,4} = \frac{\mathbf{e}_{1,3} \times (\mathbf{a} \times \mathbf{b})}{|\mathbf{a} \times \mathbf{b}|}. \tag{12}$$

Since u_1, u_2, v_1 and v_2 are all greater than zero, the obtained dispersion is of semi-Dirac type as predicted by Damljanović and Gajić (2017), but the accidental double degeneracy is missed.

Exact solution, based on solving quartic characteristic equation, gives the following condition for double degeneracy:

$$(\gamma_{13}^2 + \gamma_{14}^2)\gamma_{34}^2 \sin^2(\mathbf{q} \cdot \mathbf{b}/2) = \gamma_{13}^2 \gamma_{14}^2 \sin^2(\mathbf{a} \cdot \mathbf{q} + \mathbf{b} \cdot \mathbf{q}/2), \tag{13}$$

which has solution for sufficiently small $|\mathbf{q}|$, irrespectively of relations between γ_{13} , γ_{14} and γ_{34} . The Taylor expansion of the exact energy around $\mathbf{q} = 0$ (B -point) gives $E_{1,2} \approx E'_0 \pm (1/2)\sqrt{u_2}|q'_1|$, in the direction \mathbf{e}_3 , and $E_{1,2} \approx E'_0 \pm (1/2)w_2|q'_2|^3$, in the direction perpendicular to \mathbf{e}_3 . Similarly, $E_{3,4} \approx E_0 \pm (1/2)\sqrt{u_1}|q_1|$ in the direction \mathbf{e}_1 and $E_{3,4} \approx E_0 \pm (1/2)w_1|q_2|^3$, in the direction perpendicular to \mathbf{e}_1 . Here:

$$w_{1,2} = \frac{|\mathbf{a} \times \mathbf{b}|^3}{3u_{1,2}^{3/2}} \frac{\gamma_{13}\gamma_{14}\gamma_{34}}{\sqrt{\gamma_{13}^2 + \gamma_{14}^2}} \left(\frac{\gamma_{13}^2 \gamma_{14}^2}{\gamma_{13}^2 + \gamma_{14}^2} - \gamma_{34}^2 \right). \tag{14}$$

For the A -point we make substitution $\gamma_{13} \rightarrow -\gamma_{13}$ in the above formulas. It follows that the first order perturbation theory gives correct BZ-direction of Dirac-like dispersion and correct behavior of band structure in this direction. For the orthogonal direction as well as behavior of bands in complete vicinity of A , B -points the first order perturbation theory is not sufficient and higher order corrections are needed.

Regarding line of accidental spinless degeneracy found in exact solution of four-component Hamiltonian, one has to note that similar degeneracy occurs in the tight-binding example for layer group $Dg48$ of Damljanić and Gajić (2017). In this case the degeneracy is a consequence of the fact that model Hamiltonian is two-component and that third order polynomial has at least one real zero. By studying the compatibility relations of all four layer single groups found in Damljanić and Gajić (2017) in the vicinity of \mathbf{k}_0 we get that two-dimensional irrep decomposes into two nonequivalent, one-dimensional irreps: $\Gamma_{2D}(G(\mathbf{k}_0)) = \Gamma_{1D}(G(\mathbf{k}_0 + \mathbf{q})) + \Gamma'_{1D}(G(\mathbf{k}_0 + \mathbf{q}))$, where \mathbf{q} is small, jet non-zero wave vector. According to von Neumann–Wigner theorem, two bands touching at \mathbf{k}_0 do not repel each other at nearby points and may cross there too (Landau and Lifshitz 1981).

3 Conclusions

In summary, we have investigated electronic dispersion on a structure belonging to layer group $Dg5$, using tight-binding model from s -orbitals. We applied two methods for obtaining electronic dispersion: the first order perturbation theory of doubly degenerate level and exact diagonalization based on solving quartic equation. The first order perturbation method gives correct behavior in the Dirac-dispersion direction, while for other directions one needs higher order corrections. Accidental node line present in the exact method does not appear in the first order perturbation method. Further investigation should show if e.g. band topology cause these lines to always appear in four groups from Damljanić and Gajić (2017).

In addition, we have pointed out that in the literature there have already been reported numerically stable 3D structures, which consist of weakly interacting layers belonging to $Dg5$. Closer ab initio electronic band structure investigations of single layers of these structures, could give more insight into the particular types of semi-Dirac dispersion that are expected to appear.

Acknowledgements This work was supported by the Serbian Ministry of Education, Science and Technological Development under Project Nos. OI 171005 and III 45016.

References

- Banerjee, S., Pickett, W.E.: Phenomenology of a semi-Dirac semi-Weyl semimetal. *Phys. Rev. B* **86**, 075124 (2012)
- Banerjee, S., Singh, R.R.P., Pardo, V., Pickett, W.E.: Tight-binding modeling and low-energy behavior of the semi-Dirac point. *Phys. Rev. Lett.* **103**, 016402 (2009)
- Bergerhoff, G., Hundt, R., Sievers, R., Brown, I.D.: The inorganic crystal structure data base. *J. Chem. Inf. Comput. Sci.* **23**, 66–69 (1983)
- Cheon, G., Duerloo, K.-A.N., Sendek, A.D., Porter, C., Chen, Y., Reed, E.J.: Data mining for new two- and one-dimensional weakly bonded solids and lattice-commensurate heterostructures. *Nano Lett.* **17**, 1915–1923 (2017)
- Damljanović, V., Gajić, R.: Existence of semi-Dirac cones and symmetry of two-dimensional materials. *J. Phys. Condens. Matter* **29**, 185503 (2017)
- Deplace, P., Montambaux, G.: Semi-Dirac point in the Hofstadter spectrum. *Phys. Rev. B* **82**, 035438 (2010)
- Dittmar, G., Schaefer, H.: Die Struktur des Di-Zinn-Hexathiohypodiphosphats $\text{Sn}_2\text{P}_2\text{S}_6$. *Z. Naturforschung B* **29**, 312–317 (1974)
- Duan, H., Yang, M., Wang, R.: Electronic structure and optic absorption of phosphorene under strain. *Phys. E* **81**, 177–181 (2016)
- El-Horr, N., Bagieu Beucher, M.: Structure d'un polyphosphate mixte de plomb et de lithium, $\text{Pb}_2\text{Li}(\text{PO}_3)_5$. *Acta Crystallogr. C* **42**, 647–651 (1986)
- Geilhufe, R.M., Borysov, S.S., Bouhon, A., Balatsky, A.V.: Data mining for three-dimensional organic Dirac materials: focus on space group 19. *Sci. Rep.* **7**, 7298 (2017)
- Hahn, T. (ed.): *International Tables for Crystallography Volume A: Space-Group Symmetry*. Springer, Dordrecht (2005)
- Hautier, G., Jain, A., Ong, S.P., Kang, B., Moore, C., Doe, R., Ceder, G.: Phosphates as lithium-ion battery cathodes: an evaluation based on high-throughput ab initio calculations. *Chem. Mater.* **23**, 3495–3508 (2011)
- Huang, H., Liu, Z., Zhang, H., Duan, W., Vanderbilt, D.: Emergence of a Chern-insulating state from a semi-Dirac dispersion. *Phys. Rev. B* **92**, 161115 (2015)
- Israel, R., de Gelder, R., Smits, J.M.M., Beurskens, P.T., Eijt, S.W.H., Rasing, T., van Kempen, H., Maior, M.M., Motrija, S.F.: Crystal structure of di-tin-hexa(seleno)hypodiphosphate, $\text{Sn}_2\text{P}_2\text{Se}_6$, in the ferroelectric and paraelectric phase. *Z. Krist. Cryst. Mater.* **213**, 34–41 (1998)
- Jain, A., Hautier, G., Moore, C.J., Ong, S.P., Fischer, C.C., Mueller, T., Persson, K.A., Ceder, G.: A high-throughput infrastructure for density functional theory calculations. *Comput. Mater. Sci.* **50**, 2295–2310 (2011)
- Kim, J., Baik, S.S., Ryu, S.H., Sohn, Y., Park, S., Park, B.-G., Denlinger, J., Yi, Y., Choi, H.J., Kim, K.S.: Observation of tunable band gap and anisotropic Dirac semimetal state in black phosphorus. *Science* **349**, 723–726 (2015)
- Kopsky, V., Litvin, D.B. (eds.): *International Tables for Crystallography Volume E: Subperiodic Groups*. Kluwer, Dordrecht (2002)
- Landau, L.D., Lifshitz, L.M.: *Quantum Mechanics: Non-Relativistic Theory*. Butterworth-Heinemann, London (1981)
- Mañes, J.L.: Existence of bulk chiral fermions and crystal symmetry. *Phys. Rev. B* **85**, 155118 (2012)
- Mannhart, J., Schlom, D.G.: Oxide interfaces—an opportunity for electronics. *Science* **327**, 1607–1611 (2010)
- Narayan, A.: Floquet dynamics in two-dimensional semi-Dirac semimetals and three-dimensional Dirac semimetals. *Phys. Rev. B* **91**, 205445 (2015)
- Pardo, V., Pickett, W.E.: Half-metallic semi-Dirac-point generated by quantum confinement in TiO_2/VO_2 nanostructures. *Phys. Rev. Lett.* **102**, 166803 (2009)
- Pardo, V., Pickett, W.E.: Metal-insulator transition through a semi-Dirac point in oxide nanostructures: VO_2 (001) layers confined within TiO_2 . *Phys. Rev. B* **81**, 035111 (2010)
- Saha, K.: Photoinduced Chern insulating states in semi-Dirac materials. *Phys. Rev. B* **94**, 081103 (2016)
- Saha, K., Nandkishore, R., Parameswaran, S.A.: Valley-selective Landau–Zener oscillations in semi-Dirac p–n junctions. *Phys. Rev. B* **96**, 045424 (2017)

- Staffel, T., Mayer, G.: Synthesis and crystal structures of $\text{Cd}(\text{AlCl}_4)_2$ and $\text{Cd}_2(\text{AlCl}_4)_2$. *Z. Anorg. Allg. Chem.* **548**, 45–54 (1987)
- Wang, J.-R., Liu, G.-Z., Zhang, C.-J.: Excitonic pairing and insulating transition in two-dimensional semi-Dirac semimetals. *Phys. Rev. B* **95**, 075129 (2017)
- Xian, L., Paz, A.P., Bianco, E., Ajayan, P.M., Rubio, A.: Square selenene and tellurene: novel group VI elemental 2D materials with nontrivial topological properties. *2D Mater.* **4**, 041003 (2017)
- Zhao, P.-L., Wang, J.-R., Wang, A.-M., Liu, G.-Z.: Interplay of Coulomb interaction and disorder in a two-dimensional semi-Dirac fermion system. *Phys. Rev. B* **94**, 195114 (2016)
- Zhong, C., Chen, Y., Xie, Y., Sun, Y.-Y., Zhang, S.: Semi-Dirac semimetal in silicene oxide. *Phys. Chem. Chem. Phys.* **19**, 3820–3825 (2017)

Bifurcation in reflection spectra of holographic diffraction grating recorded on dichromated pullulan

Svetlana Savić-Šević¹ · Dejan Pantelić¹ · Vladimir Damljanović¹ · Branislav Jelenković¹

Received: 6 November 2017 / Accepted: 3 April 2018
© Springer Science+Business Media, LLC, part of Springer Nature 2018

Abstract Volume diffraction gratings were created holographically on a dichromated pullulan (polysaccharide doped with chromium). Specific and very rare multi-peak structure in the reflection spectra is observed. It was found that multiple peaks are consequence of non-ideal structure of volume diffraction grating. Theoretical analysis and numerical simulations confirm that the observed behavior arise from a slight randomness of grating parameters: refractive index, grating period, film thickness. The results of calculation are in agreement with experimental results.

Keywords Holographic diffraction grating · Reflection spectra · Bifurcation · Polysaccharide

1 Introduction

Reflection volume hologram gratings, fabricated using a single-beam method, usually have only one Bragg peak in the spectrum. Wang et al. (2006) noted the appearance of multiple peaks in the spectrum of volume diffraction grating recorded in dichromated gelatin, phenomenon that looks like bifurcation within the Bragg plateau. We also observed bifurcation phenomena in the reflection spectrum of diffraction gratings recorded in dichromated pullulan (DCP), which is a polysaccharide doped with chromium. Compared to dichromated gelatin, the DCP material is simpler to prepare and process, it is weakly sensitive to humidity, thus retaining high resolution and diffraction

This article is part of the Topical Collection on Focus on Optics and Bio-photonics, Photonica 2017.

Guest Edited by Jelena Radovanovic, Aleksandar Krmpot, Marina Lekic, Trevor Benson, Mauro Pereira, Marian Marciniak.

✉ Svetlana Savić-Šević
savic@ipb.ac.rs

¹ Institute of Physics, University of Belgrade, Pregrevica 118, 11080 Zemun, Belgrade, Serbia

efficiency (Pantelic et al. 1998; Savic et al. 2002; Savić-Šević and Pantelic 2007). The typical number of peaks in the spectrum is between two and four. We have extended the research presented in (Wang et al. 2006) by taking into account that the grating parameters depend also on x, y coordinates.

In order to understand multi-peak structure of diffraction gratings, experimental results were compared with theory. The corresponding model investigates effects of several important parameters: absorption of radiation within the photosensitive layer, non-uniform thickness of layers, refractive index modulation and non-uniform spatial period of the grating. Reflection spectra of volume Bragg gratings were calculated using method of characteristic matrix (Born and Wolf 1980). Our model suggests that multi peak structures are produced by uneven modulation of Bragg layers inside the volume hologram. The results of calculation are in agreement with experimental results. Such behavior of reflection spectra is important for effect of broadening bandgaps of photonic crystals. Understanding mechanism of their formations and appearance can help us to establish standard procedure for fabrications of such spatially non uniform volume gratings.

2 Fabrication and optical characterization of volume holographic gratings

The results presented below were obtained by the following preparation procedure for DCP. Holographic photosensitive material was prepared by mixing 10% aqueous solution of pullulan (from Sigma–Aldrich) and 10% of the ammonium dichromate. DCP solution was stirred and warmed to 50 °C to achieve homogeneity. The solution was coated onto a thoroughly cleaned glass slides placed on the flat horizontal surface. Film was dried overnight under normal laboratory conditions. The thicknesses of the dried layers, was 14 μm .

The experimental setup is shown in Fig. 1. Periodic structures in a DCP were fabricated using a single-beam method schematically shown in Fig. 1a. Hologram recording was achieved by exposing DCP to a single longitudinal mode, diode pumped Nd-YAG laser (Verdi) at 532 nm. The laser beam was expanded and pullulan layer was exposed at normal incidence with 200 mW/cm^2 of optical power, for 120 s. After propagation through emulsion, the beam was reflected back from a mirror behind the holographic plate. The two counter-propagating beams interfere, creating a standing wave pattern within an emulsion.

Plates were chemically processed, after the exposure. Processing involves washing the plates in a mixture of water and isopropyl alcohol (3:1 ratio) for 120 s, and drying for 60 s in pure isopropyl alcohol. Periodic structure formed below the surface during the processing is revealed in cross-sectional view of the DCP grating, Fig. 2.

To measure reflection, and transmission spectra, of the DCP, light from the halogen lamp was collimated and directed onto the DCP plate using set-ups given in Fig. 1b, c, respectively. Spectra were measured using fiber type spectrometer (Ocean Optics).

The photonic structure obtained under usual experimental conditions looks uniform, as in Fig. 3a. However, magnified part of the same sample shows that the structure is not ideally uniform across the layer of the DCP, Fig. 3b. In Fig. 3c we show several transmission spectra of the same DCP grating. Spectra were measured using the microscope attached to the spectrometer, as schematically presented in Fig. 1c. Transmission spectra were measured at several positions and each spectrum corresponds to area which is approximately 50 μm in diameter, with 1 mm distance between two adjacent areas.

Fig. 1 Experimental setup for **a** generating holographic diffraction gratings in DCP; and for measuring reflection and transmission spectra **b** macroscopically; and **c** microscopically

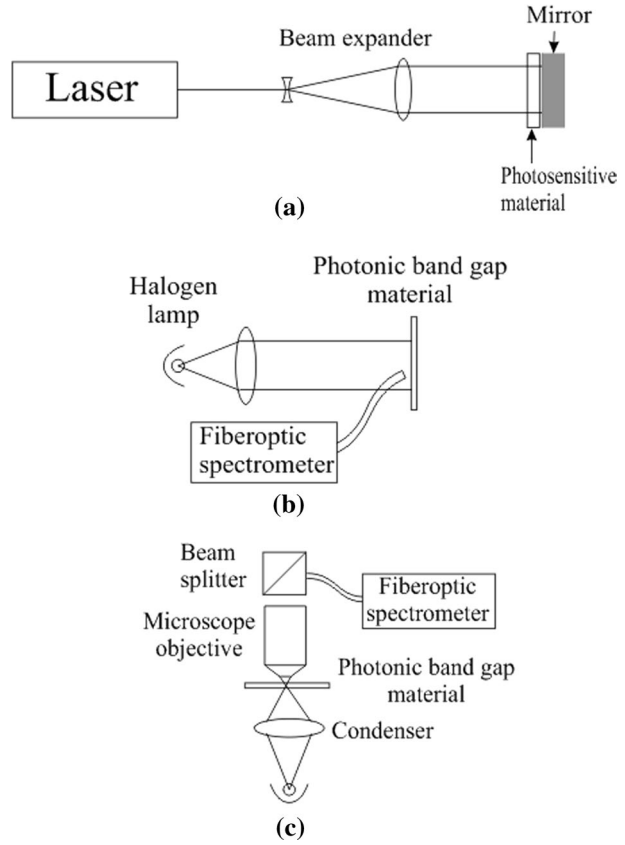
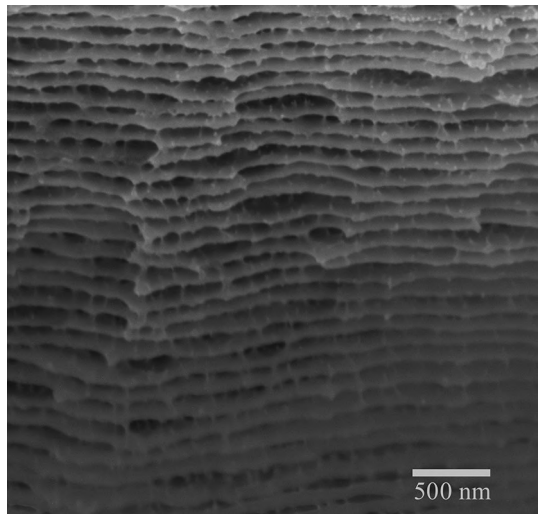


Fig. 2 SEM picture of the cross - section of DCP volume diffraction grating



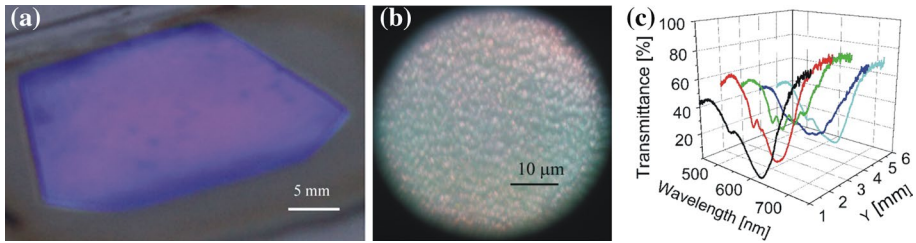


Fig. 3 **a** Image of the DCP sample, the scale bar is 5 mm; **b** zoomed part of the image **a** obtained using $\times 40$ objectives, and microscopic set-up shown in Fig. 1c. The scale bar is 10 μm ; **c** transmission spectra obtained from different areas (each of diameter of 50 μm) of the DCP sample, with 1 mm distance between two adjacent areas

3 Numerical simulations

We have calculated reflection spectra of a volume Bragg gratings by the method of characteristic matrix (Born and Wolf 1980). First, we approximated the refractive index variation along the direction perpendicular to the DCP surface, with a function whose mathematical expression is as follows (Wang et al. 2006, 2008; Liu and Zhou 1994):

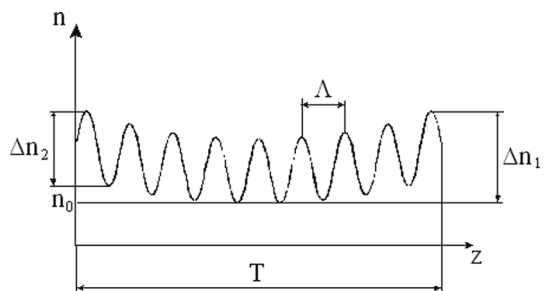
$$n(z) = n_0 + \Delta n_1 \exp(-\alpha_g T) \operatorname{ch} \left\{ \alpha_g \left[(N - j + 1)\Lambda - \frac{z}{M_j} \right] \right\} + \Delta n_2 \exp(-\alpha_g T) \cos \left(\frac{2\pi \times z}{\Lambda \times M_j} \right) \tag{1}$$

Graphical presentation of the function is given in Fig. 4. As can be seen from Eq. (1), z -dependence of the refractive index $n(z)$ incorporates three terms. The first one is the average refractive index of the material n_0 , indicated by the dashed line in Fig. 4.

The second term describes the effects of attenuation of two counter-propagating beams leading to global variation of the refractive index Δn_1 (described by hyperbolic cosine). The last term describes a sinusoidal modulation (with amplitude Δn_2) of the index of refraction. Additional parameters are: α_g —absorption coefficient, T —the material thickness, Λ —grating period, N —the number of grating layers. We assume that the grating period is not constant, due to uneven expansion of the material during processing. Instead, each period of the grating (defined by parameter j ; $1 \leq j \leq N$) is slightly changed, as defined by random variable M_j :

$$M_j = 1.262 - \frac{0.26}{N - 1} j + \frac{R_j}{45} \tag{2}$$

Fig. 4 Refractive index variation of a Bragg grating recorded in DCP, used in theoretical calculations



where R_j is a random number with Gaussian statistics, zero mean value and the standard deviation of 1.5. Variation of the layer thickness is small, however, consequences on optical properties are significant, leading to the band gap broadening.

With the above assumptions, the method of characteristic matrix produces rapidly oscillating spectra. This is different from experimentally recorded smooth spectra. Therefore, we had to modify the theoretical model. In previous research (Wang et al. 2006), it was assumed that grating parameters vary only along z-axis (i.e. depth of material). As we have found from microscope images (Fig. 3b, c) transmission or reflection spectra depend on the location on the material surface (x and y coordinates). This means that the grating parameters depend on x, y coordinates too. The resulting spectrum (as measured by any finite aperture optical device) is an average value of many spectra integrated along the aperture.

Therefore, we introduced an additional random factor $r_{k,j}$ into Eq. (2):

$$M_j \rightarrow M_j + \frac{r_{k,j}}{45} = 1.262 - \frac{0.26}{N-1}j + \frac{R_j}{45} + \frac{r_{k,j}}{45} \quad (3)$$

here $r_{k,j}$ is also Gaussian random number with mean value 0 and standard deviation of 1.5. The meaning of other parameters is the same as in Eq. (2).

First we use Eq. (2) to calculate spectrum by the characteristic matrix method. This calculation is repeated several times giving typically reflection spectra with 2, 3 and 4 peaks. The following values for parameters were used: $n_0=1.45$, $\Lambda=184$ nm, $N=78$, $\Delta n_1 \exp(-\alpha_g T) = \Delta n_2 \exp(-\alpha_g T) = 0.08$, $T=14$ μm , and $\alpha_g = 0.02(\mu\text{m})^{-1}$ (measured value). Then we fixed R_j and generate arrays $r_{k,j}$ where k is from 1 to 15 and j from 1 to 78. These way k different spectra were calculated and the result is obtained by averaging individual spectra.

The results of the model given in (Wang et al. 2006) show that appearance of multi peak band gap can be due to uneven spatial modulation of interference pattern recorded inside the material. There are two reasons for uneven modulation, irregular swelling of material during processing, and attenuation of radiation inside the emulsion.

The results of our calculations are shown in Fig. 5. We can see that for different variations of layer thickness after processing, different number of peaks appear. Since differences in the variations in the layer thickness are exclusively due to presence of random parameter with Gaussian distribution, we can assign appearance of peaks to this parameter, which is in agreement with (Wang et al. 2006).

Results presented in the upper row in Fig. 5, calculated assuming that thickness of layers varies (middle row) according to Eq. (2), contain noise-like, rapidly oscillating part. The bottom row in Fig. 5 presents resulting spectra obtained by lateral averaging defined by Eq. (3). Averaging over spectrums from several neighboring points eliminates rapidly oscillating part. In the bottom row of Fig. 5 we compare reflection spectra obtained experimentally using set-up shown in Fig. 1b (black dotted curves) and by numerical simulation (red solid curves). The results of calculation are in agreement with experimental results.

4 Discussion of fabrication of structured band gaps in DCP

Structured reflection spectra under the usual chemical processing are very rare [0.5% probability (Wang et al. 2006)]. In order to investigate how special techniques in processing volume holograms lead to more frequent appearance of structured reflection spectra, we prepared 250 samples of DCP photonic crystals with different concentration of ammonium

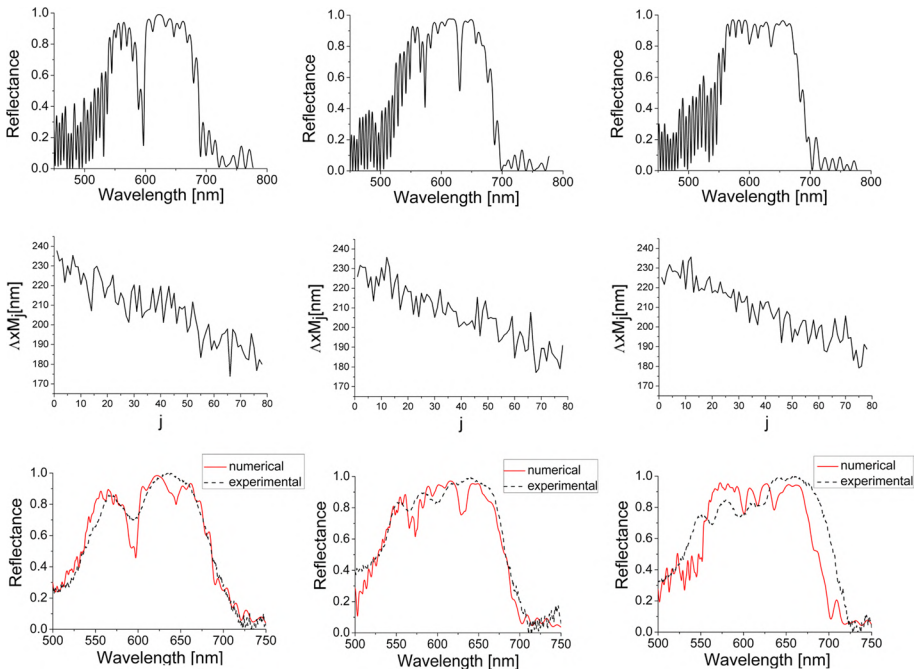


Fig. 5 Calculated reflection spectra of photonic structures in DCP showing multiple peaks as result of the layer thickness variation (upper row). Layer thickness variation (middle row). Averaged results taking into account the different thickness variation of layers in adjacent lateral regions of the film (red solid curve) and reflection spectra obtained experimentally (black dotted curve) using set-up shown in Fig. 1b (bottom row). (Color figure online)

dichromate (from 10 to 50% by weight of pullulan), different thickness of DCP (6–30 μm) and use various chemical processing. Samples were developed in mixture of water and isopropyl alcohol. We noticed that probability of obtaining multi peak and wider band gap photonic crystals is higher (although by only a few percent), by increasing the water to isopropyl ratio. If water to isopropyl ratio is 3:1 or more, analysis of our samples shows that probability of obtaining two peak photonic crystals is about 10 and 1.5% for three or more peaks.

5 Conclusions

In this paper we investigated bifurcation in the reflection spectra of the holographic DCP gratings. Volume holograms in DCP were made using simple, single-beam holographic technique. Although these types of diffraction spectra of volume hologram are usually rare, there are exact ways to increase the frequency of appearance of multi peak structure by using certain techniques in processing of DCP, as described in Sect. 2. Our simulation model suggests that multi peak structures are produced by uneven modulation of interference pattern inside the volume hologram. In addition, smoothness of reflectivity function is due to the difference in layer thickness in neighboring regions of the grating.

Acknowledgements This work was funded by the Ministry of Education, Science and Technological Development of the Republic of Serbia, under Grants Number OI 171038 and III 45016.

References

- Born, M., Wolf, E.: Principles of Optics. Pergamon, New York (1980)
- Liu, D., Zhou, J.: Nonlinear analysis for a reflection hologram. *Opt. Commun.* **107**, 471–479 (1994)
- Pantelić, D., Savić, S., Jakovljević, D.: Dichromated pullulan as a novel photosensitive holographic material. *Opt. Lett.* **23**, 807–809 (1998)
- Savić, S., Pantelić, D., Jakovljević, D.: Real-time and postprocessing holographic effects in dichromated pullulan. *Appl. Opt.* **41**, 4484–4488 (2002)
- Savić-Sević, S., Pantelić, D.: Dichromated pullulan diffraction gratings: influence of environmental conditions and storage time on their properties. *Appl. Opt.* **46**, 287–291 (2007)
- Wang, Z., Liu, D., Zhou, J.: Investigation of a peculiar bifurcation phenomenon in diffraction spectra of volume holograms. *Opt. Lett.* **31**, 3270–3272 (2006)
- Wang, Z., Zhai, T., Zhao, R., Liu, D.: The influence of asymmetric expansion properties and random fluctuation on the bandwidth of a hologram. *J. Opt. A Pure Appl. Opt.* **10**, 085205 (2008)

BOOK OF ABSTRACTS



7-10 July 2020

NN20

**17th International
Conference
on Nanosciences
& Nanotechnologies**

2020

WS2-Computational	
16:30-16:45	KEYNOTE (L) M. Damnjanovic, University of Belgrade, Serbia
16:45-17:00	Topological phases of layers: elementary band representations
17:00-17:15	INVITED (L) V. Damljanović, University of Belgrade, Serbia
17:15-17:30	Electronic Dispersions in Two- and Three-Dimensional Single Crystals From Symmetry Point of View
17:30-17:45	INVITED (L) I. Miloević, University of Belgrade, Serbia
17:45-18:00	Electronic-band topology of group VI layered transition metal dichalcogenides
18:00-18:15	INVITED (V) M. Zacharias, Cyprus University of Technology, Cyprus
18:15-18:30	Temperature dependence of the optical properties of silicon nanocrystals
18:30-18:45	E. Antoniou Aristotle University of Thessaloniki, Greece (V) Ab Initio Computational Investigation of Structure & Magnetic Properties of SmCo ₅ -XNi _x Intermetallic Compounds
18:45-19:00	Ronald Columbié-Leyva, Instituto de Investigación en Materiales, UNAM, México. (V) Theoretical studies of high-T _c Fe-superconductors based on BaFe ₂ As ₂ in presence of dopants Rh and Pd.
19:00-19:15	C. Simserides, National and Kapodistrian University of Athens, Greece (V) Hole transfer in cumulenic and polyyenic carbynes
19:15-19:30	M. Witkowski, University of Warsaw, Poland (V) DFT modeling of SERS spectra of dipeptides: A comprehensive study of vibrational structure for Cys-Trp and Trp-Cys adsorbed on Au and Ag

Topological phases of layers: elementary band representations

M. Damjanovic¹

NanoLab, Faculty of Physics, University of Belgrade Studentski trg 12, 11000 Belgrade, Serbia

Research of topological phases is probably the main stream of condensed matter physics. In brief, Bloch theory transforms band structure of the hamiltonian spectrum into the fibre bundle over Brillouin zone (BZ), in this way enabling topological characterization of such bundles. Extensive work is performed within differential-geometric framework: Berry phase and derived notions (connection, curvature and Wilson loop e.g.), are used to find topological invariants like winding and Chern numbers. However, 30 years ago Mischel and Zak, pathed the symmetry based combinatorial way to classify band structures. Reconsidered recently, these results are firmly related to topological phases of crystals. This purely algebraic method considers graphs graphs imposed by symmetry. The first one is graph of Brillouin zone: as a contractible manifold, each stratum of k -vectors with equivalent (conjugated) stabilizers is a vertex of the graph, while (oriented) edges connect neighbouring strata. Bands are made of patches over strata, each corresponding to specific allowed irreducible representation (IR) associated to the stratum. Contraction of BZ to graph, causes simultaneous contraction of the band patches, and the whole band structure becomes IR-graph: vertices are IRs, while edges represent connected patches. These edges are subdued to compatibility relations, or better, they depict them. Therefore, having BZ-graph, and compatibility relations (the both are directly and fully symmetry-determined), all possible IR-graphs are found in a combinatorial manner. This procedure is implemented in POLSym code, and applied to all layer groups (single and double, with or without time reversal). The results are presented, together with various analyses. For example, the disconnected graphs are looked for, as pointing out topologically non-trivial phases. Also, selected are band structures with special subgraphs which indicate possible atomic limits.

Electronic Dispersions in Two- and Three-Dimensional Single Crystals From Symmetry Point of View

V. Damljanović¹

Institute of Physics Belgrade, University of Belgrade, Pregrevica 118, Belgrade, Serbia

In spatially periodic atomic arrangements, the electronic energy depends on the wave vector and forms a band structure. The form of a band in the vicinity of some point in the Brillouin zone is called the electronic dispersion and determines many physical properties of a material. Examples of electronic dispersions are Dirac (e.g. in graphene), semi-Dirac (e.g. in black phosphorus) and quadratic (e.g. in MoS₂). On the other hand, every crystal periodic in two (three) directions belongs to one of 80 layer- (230 space-) groups. Here we present deep connection between the crystal symmetry and the types of electronic dispersions present in the crystal. Our contribution is based on works published for two- [1-3] and three-dimensional [4-7] single crystals. We show that new and unexpected types of dispersions often appear as a consequence of crystal symmetry. This may be the clue for discovery of new materials with interesting physical properties.

References:

- [1] V. Damljanović, R. Gajić, Journal of Physics: Condensed Matter **28**, 085502 (2016).
- [2] V. Damljanović, R. Gajić, Journal of Physics: Condensed Matter **28**, 439401 (2016).
- [3] V. Damljanović, I. Popov, R. Gajić, Nanoscale **9**, 19337-19345 (2017).
- [4] J. L. Mañes, Physical Review B **85**, 155118 (2012).
- [5] B. J. Wieder, Y. Kim, A. M. Rappe, C. L. Kane, Physical Review Letters **116**, 186402 (2016).
- [6] B. Bradlyn et al., Science **353**, 10.1126/science.aaf5037 (2016).
- [7] B. J. Wieder et al., Science **361**, 246-251 (2018).

2020

NN20

17th International Conference on Nanosciences & Nanotechnologies
NN20 is part of NANOTECHNOLOGY 2020

Organized by



Supported by



Under the Auspices



www.nanotechnology.com

FUNDAMENTALS
and APPLICATIONS

LIGHT
MATTER
INTERACTIONS *for*

*biophysics
biomedicine
communications
sensors
devices*



WORKSHOP
PHOTONICS

Kopaonik, Serbia

8.3.-12.3.2020.

Organizers

Sponsors



Institute of Physics Belgrade
University of Belgrade
Kopaonik, March 08-12, 2020



Book of Abstracts
13th Photonics Workshop
(Conference)



13th Photonics Workshop

Kopaonik, 08.3-12.03.2020.

13th Photonics Workshop (2020)

Book of abstracts

Kopaonik, Serbia, March 08-12, 2020

Publisher, 2020:

Institute of Physics Belgrade

Pregrevica 118

11080 Belgrade, Serbia

Editors:

Dragan Lukić, Marina Lekić, Zoran Grujić

ISBN 978-86-82441-50-2

Printed by:

NEW IMAGE d.o.o.

Cara Dušana 212, Zemun, Belgrade

Number of copies: 60

CIP - Каталогизacija y publikaciji Narodna biblioteka Srbije, Beograd

535(048)

681.7(048)

66.017/.018(048)

PHOTONICS Workshop (13 ; 2020 ; Kopaonik)

Book of Abstracts / 13th Photonics Workshop, (Conference), Kopaonik, March 08-12, 2020 ; [editors Dragan Lukić, Marina Lekić, Zoran Grujić]. - Belgrade : Institute of Physics, 2020 (Belgrade : New image). - 58 str. : ilustr. ; 25 cm

Tiraž 60. - Registar.

ISBN 978-86-82441-50-2

a) Оптика -- Апстракти b) Оптиелектроника -- Апстракти v) Технички материјали
-- Апстракти

COBISS.SR-ID 283421708

Unusual electronic dispersions in non-magnetic, spin-orbit coupled, two-dimensional materials from double groups perspective

V. Damljanović¹

(1) *Institute of Physics Belgrade, University of Belgrade, Pregrevica 118, 11000 Belgrade, Serbia*

Contact: V. Damljanović (damlja@ipb.ac.rs)

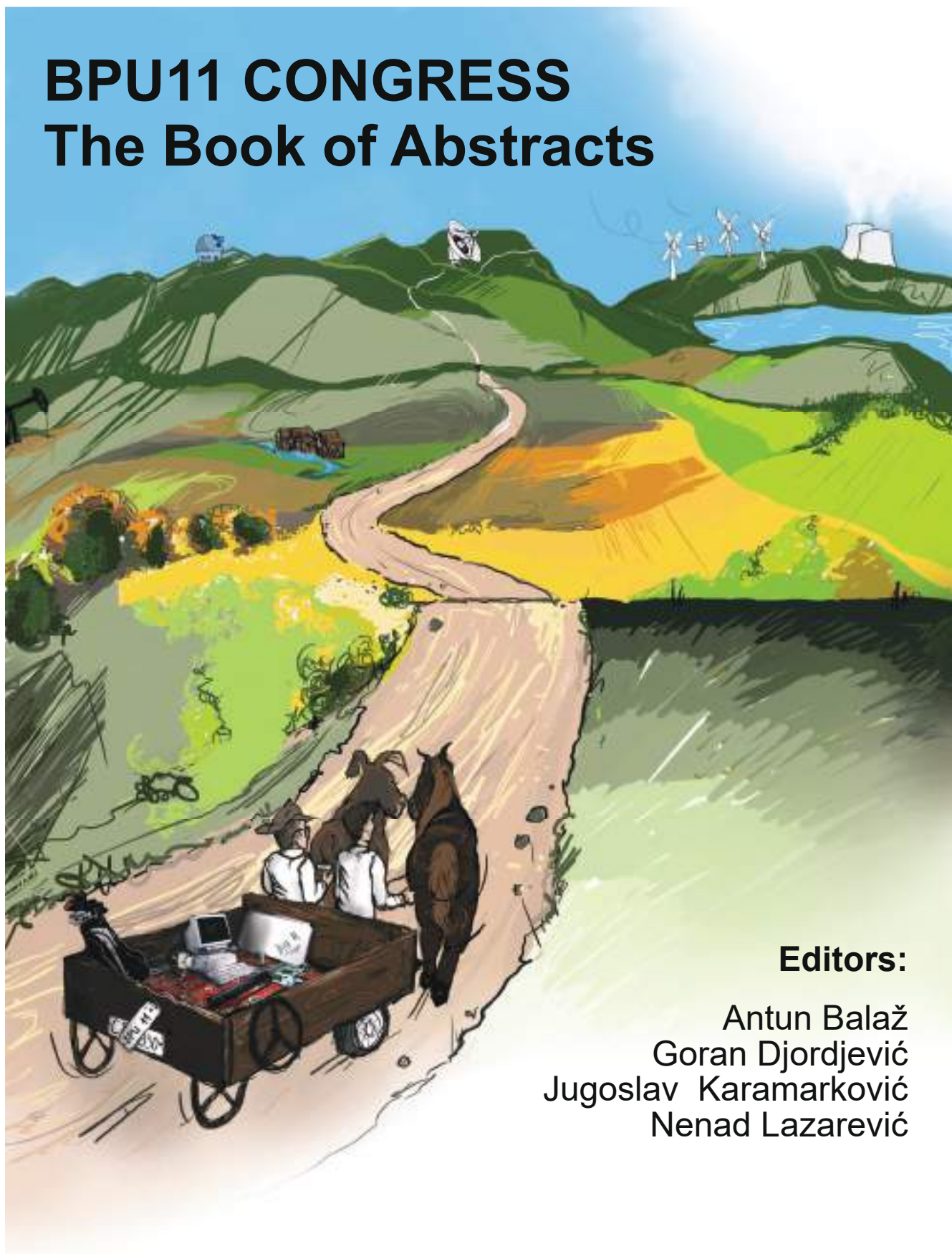
Abstract. When electron spin and orbital degrees of freedom are coupled, rotation in real space induces analogous transformation of two-component wave functions - Pauli spinors. Similarly, a symmetry group of an object in real space becomes a symmetry group in both real and spin space – so called double group [1]. In this contribution we used theory of layer double group representations to search for new electronic dispersions in non-magnetic, time-reversal symmetric two-dimensional materials with non negligible spin-orbit coupling [2]. Apart from known fortune-teller (FT) dispersion [3], we have found a new one: a generalization of both FT and Dirac dispersions. Our findings illustrate the fact that “to actually discover a feature in a band structure that provides the quasiparticle dispersion of a new and unexpected type is rare” [4] and that symmetry often provides such discovery.

REFERENCES

- [1] H. Bethe, *Ann. Phys. (Leipzig)* **3** (1929), 133–208.
- [2] V. Damljanović, N. Lazić, A. Šolajić, J. Pešić, B. Nikolić, M. Damjanović, *submitted* (2020).
- [3] V. Damljanović, I. Popov, R. Gajić, *Nanoscale* **9** (2017), 19337–19345.
- [4] S. Banerjee, W. E. Pickett, *Phys. Rev. B* **86** (2012), 075124.

BPU11 CONGRESS

The Book of Abstracts



Editors:

Antun Balaž
Goran Djordjević
Jugoslav Karamarković
Nenad Lazarević

Belgrade, 2022



BPU11 CONGRESS

28 August 2022 - 1 September 2022

Book of Abstracts

Editors: Antun Balaž, Goran Djordjević,
Jugoslav Karamarković, Nenad Lazarević

Belgrade, 2022

BPU11 CONGRESS

The 11th International Conference of the Balkan Physical Union

The Book of Abstracts

Editors:

Antun Balaž, Goran Djordjević,
Jugoslav Karamarković, Nenad Lazarević

Technical Editor: Milan Milošević

Cover Design: Elena Denda

Printed by: Planeta Print, Belgrade

ISBN: 978-86-7025-950-8

Print run: 350

Co-organizers

- Serbian Academy of Sciences and Arts (SASA)
- Faculty of Sciences and Mathematics, University of Niš
- Faculty of Physics, University of Belgrade
- Vinča Institute of Nuclear Sciences, University of Belgrade, National Institute of the Republic of Serbia
- Faculty of Mathematics, University of Belgrade
- Mathematical Institute of Serbian Academy of Sciences and Arts, National Institute of the Republic of Serbia
- Faculty of Science, University of Kragujevac
- Faculty of Sciences, University of Novi Sad
- Faculty of Sciences and Mathematics, University of Pristina in Kosovska Mitrovica
- SEENET-MTP Centre
- European Physical Society (EPS)
- Institute of Physics Belgrade, National Institute of the Republic of Serbia

Partners and Sponsors

- International Centre for Theoretical Physics (ICTP), Trieste
- Central European Initiative (CEI), Trieste
- Ministry of Education, Science, and Technological Development, Republic of Serbia
- Conseil Européen pour la Recherche Nucléaire (CERN), Geneva
- Provincial Secretariat for Higher Education and Scientific Research, Autonomous Province of Vojvodina, Republic of Serbia
- The European Physical Journal (EPJ)

¹ *Ovidius University of Constanta: Academy of Romanian Scientists*

Presenter: V. Ciupina (vciupina@yahoo.com)

Using TVA technology, multilayer and composite C-Ti layers were deposited on silicon substrates. The C-Ti multilayers were constructed from the silicon substrate as follows: 100nm of carbon, followed by alternant 17nm Ti and 40 nm C three times, covered by one last 17 nm Ti layer, resulting a seven multilayer structure. For the composite layer, after the pre 100nm carbon one, we varied quasi continuously the Ti:C atomic ratio, from 1:9 and reaching 9:1 at the top of the 119 nm. For both composite and multilayer structures, several batches were obtained for comparison. We varied the substrate temperatures during the deposition (R. T., 100, 200, 300 and 400oC) and one deposition batch was obtained at 300oC with a -700V polarisation voltage on the substrates, in order to increase the ions energy reaching the layer, during the coating process.

Characterization of structural properties of films was achieved by Electron Microscopy technique (TEM) and GIXRD techniques. The measurements show that increase of the substrate temperature reveal changes in Ti_xC_y lattice parameters. Thus, according to GIXRD analysis it was found out that the Ti:C atomic ratio changes with increase of synthesis temperature. Also, in the case of composite films an increase of amount and sizes of TiC nanocrystals with the increase of energy of Ti ions determined by increase of polarisation voltage was observed. The tribological measurements were performed using a ball-on-disk system with normal forces of 0.5, 1, 2, 3N respectively. Was found that the coefficient of friction depends on the synthesis temperature and on the polarisation voltage. It is also noted that the friction coefficient depends on the pure C content, Ti content and amount of TiC nanocrystallites. These results are due to atomic diffusion at Ti/C interfaces and also are associated with amount of TiC nanocrystallites. Using Bruker Hysitron TI980 Triboindenter System, global hardness of the coating, in depth hardness and SPM imaging analysis were performed. By Nanoscratch Analysis, global and depth Young modulus was measured. To characterize the electrical conductive properties, the electrical surface resistance versus temperature have been measured, and then the electrical conductivity is calculated. Using the Wiedemann-Frantz law was obtained the thermal conductivity.

S06-CMPSP-101 / Oral presentation

Linear dispersions in two-dimensional materials: a crystal with symmetry pbma1' as an example

Authors: Nataša Lazić¹; Vladimir Damljanović²

¹ *NanoLab, Faculty of Physics, University of Belgrade*

² *Institute of Physics Belgrade, University of Belgrade*

Presenter: V. Damljanović (damlja@ipb.ac.rs)

Symmetry determines forms of band structures in the vicinity of special points in the reciprocal space of one-, two- and three-dimensional materials. After short introduction to the complete classification of linear dispersions in 2D materials,¹ we will focus on a particular example. A tight binding model on a crystal with four sites per primitive cell that belongs to grey layer single group *pbma* (45.2.315 or *pbma1'* in the magnetic layer groups notation of Ref. [2]) is calculated. Fortune teller states are obtained in the Brillouin zone corners, as predicted^{3,1} by group theory for non-magnetic materials with negligible spin-orbit coupling. We will discuss possible realizations of this model in realistic and hypothetical materials.

References

1. N. Lazić, V. Damljanović and M. Damnjanović, *arXiv*: 2108.11733 (2021).
2. D. B. Litvin, *Acta Cryst. A* **61**, 382 (2005).
3. V. Damljanović, I. Popov and R. Gajić, *Nanoscale* **9**, 19337 (2017).

S06-CMPSP-102 / Oral presentation

Influence of the Size of Cation on the Structure and Tribological Properties of Ionic Liquids Studied with Molecular Dynamics

Authors: Igor Stanković¹; Miljan Dašić¹

¹ *Scientific Computing Laboratory, Center for the Study of Complex Systems, Institute of Physics Belgrade, University of Belgrade, Pregrevica 118, Belgrade, 11080, Serbia*

Presenter: M. Dašić (mdasic@ipb.ac.rs)

Ionic liquids (ILs) are two-component systems composed of large asymmetric and irregularly shaped organic cations and anions. Physical properties of ILs like negligible vapour pressure, high-temperature stability, high ionic conductivity and also a great variety of ILs and their mixtures highlight them as potentially relevant to lubrication [1, 2]. A large number of variations in IL composition is possible, estimated at the order of magnitude of 10^{18} different ILs. From their variety stems the possibility of tuning their physicochemical properties which can affect lubrication, such as viscosity, polarity, surface reactivity. Hence, it would be advantageous to figure out general relations between the molecular structure and tribological properties of ILs.

In this study, we investigate a generic tailed-model (TM) of ILs which includes: an asymmetric cation consisting of a positively charged head ($\sigma_C = 5\text{\AA}$) and a neutral tail of variable size ($\sigma_T = 3, 5, 9\text{\AA}$) and a large spherical negatively charged anion ($\sigma_A = 10\text{\AA}$). It represents a more realistic model compared to the simplest one, the so called Salt Model (SM) [3, 4]. We figured that, although simple, TM model results in striking differences in equilibrium bulk structure of IL governed by the tail size relative to cationic head: (i) simple cubic lattice for the small tail, (ii) liquid-like state for symmetric cation-tail dimer, and (iii) molecular layer structure for the

CIP - Каталогизација у публикацији
Народна библиотека Србије, Београд

53(048)

INTERNATIONAL Conference of the Balkan Physical Union (11 ; 2022 ; Belgrade)

Book of Abstracts / [The 11th International Conference of the Balkan Physical Union] [i. e] BPU 11 congress, 28 August 2022-1 September 2022 ; editors Antun Balaž ... [et al.]. - Belgrade : [САНУ] ; [Ниш] : [Природно-математички факултет Универзитета], 2022 (Belgrade : Planeta print). - 298 str. ; 25 cm

Tiraž 350. - Str. 1-2: Preface / Goran S. Djordjević. - Registar.

ISBN 978-86-7025-950-8 (SANU)

1. Balaž, Antun, 1973- [уредник]

а) Физика -- Апстракти

COBISS.SR-ID 72769545

Co-organizers



Partners and Sponsors



Hybrid

ISFOE22

**15th International
Symposium
on Flexible Organic
Electronics**

**BOOK OF
ABSTRACTS**

4-7 July 2022

Live in Thessaloniki, Greece

Virtual via Video Conferencing System

2022

ISFOE22 Committees

International Organizing Committee

- S. Logothetidis**, Department of Physics, Aristotle University of Thessaloniki, Greece (Chair)
Z. Cui, Printable Electronics Research Center, Suzhou Institute of Nanotech, Chinese Academy of Sciences, China (Co-chair)
G. Hadziioannou, LCPO, CNRS, University of Bordeaux, France (Co-chair)
J. Kallitsis, Department of Chemistry, University of Patras, FORTH-ICE-HT, Greece (Co-chair)
A. Laskarakis, Department of Physics, Aristotle University of Thessaloniki, Greece (Co-chair)
G. Malliaras, Department Of Engineering, University of Cambridge, UK (Co-chair)
R. P. Silva, Nano-Electronics Centre, Advanced Technology Institute, University of Surrey, UK (Co-chair)

Local Organizing Committee

- S. Logothetidis**, Department of Physics, Aristotle University of Thessaloniki, Greece
A. Laskarakis, Department of Physics, Aristotle University of Thessaloniki, Greece

International Scientific Committee

- T. Anthopoulos**, King Abdullah University of Science and Technology, Saudi Arabia
R. Baumann, Chemnitz University of Technology, Germany
F. Biscarini, University of Modena and Reggio Emilia, Italy
Y. Bonnassieux, LPICM, Ecole Polytechnique, CNRS, France
C. Brabec, Friedrich-Alexander-University of Erlangen-Nürnberg, Germany
D. Bradley, King Abdullah University of Science and Technology, Saudi Arabia
F. Castro, National Physical Laboratory (NPL), UK
A. Christou, Maryland NanoCenter, University of Maryland, USA
T. Claypole, Welsh Centre for Printing and Coating, Swansea University, UK
Z. Cui, Printable Electronics Research Center, Suzhou Institute of Nanotech, Chinese Academy of Sciences, China
M. Damnjanovic, Faculty of Physics, University of Belgrade, Serbia
G. Deligeorgis, FORTH IESL, Greece
B. Drevillon, CNRS, Ecole Polytechnique, France
V. Dyakonov, Julius-Maximilian University of Wuerzburg, Germany
D. Dykeman, ANSYS, Inc., UK
B. Fillon, CEA Liten, France
S. Forrest, University of Michigan, USA
M. Graetzel, LPI, ISIC, EPFL, Lausanne, Switzerland
G. Hadziioannou, LCPO, CNRS, University of Bordeaux, France
R. A. J. Janssen, Eindhoven University of Technology, The Netherlands
J. Kallitsis, Department of Chemistry, University of Patras, FORTH-ICE-HT, Greece
E. Kaxiras, Harvard University, Division of Engineering and applied Sciences, USA
J. Kido, Yamagata University, Japan
T. Kolbusch, COATEMA Coating Machinery GmbH, Germany
M. Krebs, Varta Microbattery GmbH, Germany
A. Laskarakis, Department of Physics, Aristotle University of Thessaloniki, Greece
K. Leo, Novaed & Dresden Technical University, Germany
N. Li Pira, Centro Ricerche Fiat, S.C.p.A, Italy
P. Lianos, General Department of Polytechnic School of Patras, Greece
L. Lidorikis, University of Ioannina, Greece
S. Logothetidis, Department of Physics, Aristotle University of Thessaloniki, Greece
G. Malliaras, Department Of Engineering, University of Cambridge, UK
M. McLachlan, Imperial College London, UK
N. Rikita, Mitsubishi Materials Corporation, Japan
M. Schrarber, Linz Institute for Organic Solar Cells, Austria
R. Silva, Nano-Electronics Centre, Advanced Technology Institute, University of Surrey, UK
F. Stelzer, Graz University of Technology, Graz, Austria
N. Stingelin, Georgia Institute of Technology, USA
D. Tsoukalas, National Technical University of Athens, Greece
J. Ulanski, Department of Molecular Physics, Technical University of Lodz, Poland
L. Van Langenhove, Department of Textiles, Ghent University, Belgium
A. Wedel, Fraunhofer Institute for Applied Polymer Research, Germany

Topological quantum chemistry for quasi-one-dimensional systems with either translational or helical periodicity

I. Milošević, S. Dmitrović, T. Vuković, M. Damnjanović

Faculty of Physics, University of Belgrade, Studentski trg 12, Belgrade, Serbia

Abstract:

By linking symmetry with combinatorial graph theory, topological quantum chemistry [1], in terms of elementary band representations (EBRs), gives universal description of electronic band structure topology of short-range entangled matter.

Here, derived are complete sets of nonequivalent (physical) EBRs, for symmetry groups of quasi-one-dimensional systems with either translational or helical periodicity. Apart from the system configuration symmetry described by line groups (LGs), considered also is the additional symmetry of time-reversal (grey-LGs) and the symmetry originating from spin degree of freedom (double-LGs and double-grey-LGs) [2,3]. The results obtained are complete and exhaustive, thus enabling thorough algorithmic search for topological compounds across the one-dimensional matter. As an illustration, a topological mirror chain model is considered.

[1] B. Bradlyn *et al.*, Nature 547 (2017) 298

[2] I. Milošević *et al.*, J. Phys. A 53 (2020) 455204

[3] S. Dmitrović *et al.*, J. Phys. A (2022)

Linear dispersions in low-dimensional structures: the role of crystalline symmetries, time reversal, and spin-orbit coupling

N. Lazić¹, V. Damljanović², M. Damnjanović³, ...

¹ NanoLab, Faculty of Physics, University of Belgrade, Studentski trg 12, 11001 Belgrade, Serbia

² Institute of Physics Belgrade, University of Belgrade, Pregrevica 118, 11080 Belgrade, Serbia

³ Serbian Academy of Sciences and Arts, Kneza Mihaila St. 35, 11000 Belgrade, Serbia

Abstract: Crystalline symmetry imposes requirements on the band structure of material, which have consequences in the band topology. Besides gapped topological insulators, lattice symmetries are also important in describing gapless semi-metallic phases. They are characterized by band crossings on the Fermi level, and particularly interesting are those with linear energy-momentum dependence. Here, we study symmetry-enforced semi-metallic layered materials with dispersions linear in all directions around crossings hosted by high-symmetry Brillouin zone points. In particular, single and double, ordinary and grey layer groups are used to achieve the complete systematization of such fully linear band crossings and corresponding effective Hamiltonians. The resulting dispersion shapes are: single cone (with double degenerate crossing point and non-degenerate branches, or 4-fold degenerate crossing point with double degenerate conical branches), poppy-flower (4-fold degenerate crossing point with two pairs of non-degenerate mutually rotated conical branches), and a fortune teller (with nodal lines). Inclusion of spin-orbit interaction is analysed through the transition from single to double group; this results in interesting patterns at high symmetry points such as: gap closing, gap opening, cone preserving, cone splitting etc. Similarly, the role of time reversal symmetry is clarified through the ordinary to grey group transit

2022

ISFOE22

15th International Symposium on Flexible Organic Electronics

ISFOE22 is part of NANOTECHNOLOGY 2022

Organized by



Supported by

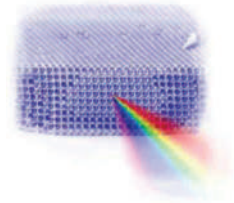


Under the Auspices of



www.nanotechnology.com

University of Belgrade
Institute of Physics Belgrade
Kopaonik, March 13-16, 2022



Book of Abstracts
15th Photonics Workshop
(Conference)



15th Photonics Workshop (2022)

Book of abstracts

Kopaonik, Serbia, March 13-16, 2022

Publisher, 2022:

Institute of Physics Belgrade

Pregrevica 118

11080 Belgrade, Serbia

Editors:

Dragan Lukić, Marina Lekić, Zoran Grujić

ISBN 978-86-82441-55-7

Printed by:

NEW IMAGE d.o.o.

Tošin Bunar 185, Belgrade

Number of copies: 55

CIP - Каталогизација у публикацији - Народна библиотека Србије, Београд

535(048)

681.7(048)

66.017/.018(048)

PHOTONICS Workshop (15; 2022; Kopaonik)

Book of Abstracts / 15th Photonics Workshop, (Conference), Kopaonik,
March 13-16, 2022; [editors Dragan Lukić, Marina Lekić, Zoran Grujić]. -

Belgrade: Institute of Physics, 2022 (Belgrade: New image). - 72 str. :

ilustr.; 25 cm

Tiraž 55. - Registar.

ISBN 978-86-82441-55-7

а) Оптика - Апстракти б) Оптиелектроника - Апстракти с) Технички
материјали - Апстракти

COBISS.SR-ID 60055049

Full classification of linear dispersions in two-dimensional materials

V. Damljanović¹, M. Damnjanović^{2,3}, N. Lazić²

(1) *Institute of Physics Belgrade, University of Belgrade, Pregrevica 118, 11080 Belgrade, Serbia*

(2) *NanoLab, Faculty of Physics, University of Belgrade, Studentski Trg12, 11001 Belgrade, Serbia*

(3) *Serbian Academy of Sciences and Arts, Kneza Mihaila St. 35, 11000 Belgrade, Serbia*

Contact: V. Damljanović (damlja@ipb.ac.rs)

Abstract. We present group-theoretical classification [1] of all possible dispersions, which are linear in all directions, in the vicinity of high-symmetry Brillouin zone points, in non-magnetic layered materials. Both spinless and spinfull cases in the presence and in the absence of time-reversal symmetry are covered. We found that only three types of such dispersions are possible: Dirac, fortune teller and poppy flower. Low energy effective Hamiltonians are also presented. Special attention will be given to some recently published results not supported by our theory [2-5].

REFERENCES

- [1] N. Lazić, V. Damljanović, M. Damnjanović, *arXiv*: 2108.11733 (2021).
- [2] B. J. Wieder, B. Bradlyn et al., *Science* **361** (2018), 246–251.
- [3] S. M. Young and C. L. Kane, *Phys. Rev. Lett.* **115** (2015), 126803.
- [4] P. J. Guo, Y. W. Wei et al., *Phys. Rev. Lett.* **127** (2021), 176401.
- [5] W. Luo, J. Ji et al., *Phys. Rev. B.* **101** (2020), 195111.

BOOK OF ABSTRACTS

**16th International
Conference
on Nanosciences
& Nanotechnologies**

NN 19



**2-5 July 2019,
Porto Palace Conference
Centre & Hotel
Thessaloniki, Greece**

2019

Wednesday 3rd July 2019

09:00-09:30 Keynote Talk (Crystal Hall)

09:00-09:30 KEYNOTE	Linear dispersions in Q1D and Q2D crystalline structures M.Damnjanović University of Belgrade, Studentski trg 12, 11001 Belgrade, Serbia
------------------------	--

Linear dispersions in Q1D and Q2D crystalline structures

M.Damnjanović¹, V. Damljanović²

¹NanoLab, Faculty of Physics, University of Belgrade, Studentski trg 12, 11001 Belgrade, Serbia

²Institute of Physics, University of Belgrade, Pregrevica 118, 11000 Belgrade, Serbia

Band structure with Dirac cone is origin of many amazing properties of graphene. Consequent Dirac equation of electron dynamics is one of the reasons for intensive research of this phenomenon during the past decade. In addition, topological band theory of insulators emphasized necessity of materials of this type as interphase for topologically different phases. In a search for other layers with similar band structure, several group theoretical conditions are singled out [1]. The conditions are applied to layer groups, and candidates for Dirac's points are singled out [2]. In fact, the band splitting occurs in a special point P in Brillouin zone; then an irreducible representation $D^{(P\alpha)}(\mathbf{G})$ of the layer symmetry group associated to this special point decomposes in several representations $D^{(P+k,\beta)}(\mathbf{G})$ associated to generic points $P+k$ in the vicinity of P . This gives compatibility relations which are strengthened by further restrictions providing linear dispersions of the split bands. Here, these group theoretical condition are revisited, and applied to line and layer ordinary and double groups, in order to find all Brillouin zone points with linear dispersions and the relevant irreducible representations (integer or half-integer). The results are discussed. For example, symmetries with linear crossing of bands only due to spin-orbit interaction are singled out.

[1] J. L. Manes, *Phys. Rev. B* **85**, 155118 (2012)

[2] V Damljanović and R Gajić, *J. Phys.: Condens. Matter* **28** (2016) 085502

**LIGHT
MATTER**
INTERACTIONS *for*

*biophotonics
biosensing
biomedicine
optical materials
photonic structures
ultrafast phenomena
nonlinear and
quantum optics*



WORKSHOP *on*
PHOTONICS

Kopaonik
10.3-14.3.2019.

Organizers

Sponsors



Копаоник, 10 – 14.03.2019.
УНИВЕРЗИТЕТ У БЕОГРАДУ
Институт за физику



Зборник апстраката

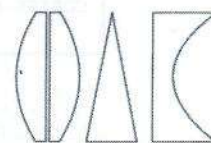
Дванаеста радионица фотонике (2019)

(Конференција)

Book of Abstracts

12th Photonics Workshop

(Conference)



Institute of Physics
University of Belgrade
Копаоник, March 10-14, 2019

Дванаеста радионица фотонике (2019)

ЗБОРНИК АПСТРАКАТА

Корпаоник 10-14.03.2019.

Издаје:

Институт за физику Београд

За издавача:

Др Александар Богојевић, директор

Уредници:

Др Драган Лукић, др Марина Лекић, др Зоран Грујић

Тираж: 70 примерака

ISBN 978-86-82441-49-6

Штампа:

NEW IMAGE d.o.o.

Цара Душана 212, Земун, Београд

CIP - Каталогизација у публикацији - Народна библиотека Србије, Београд
535(048)
681.7(048)
66.017/.018(048)
PHOTONICS Workshop (12 ; 2019 ; Корпаоник)
Book of Abstracts / 12th Photonics Workshop, (Conference), Корпаоник,
March 10-14, 2019. = Зборник апстраката / Дванаеста радионица фотонике
(2019), (Конференција) ; [urednici Dragan Lukić, Marina Lekić, Zoran
Grujić]. - Beograd : Institut za fiziku, 2019 (Beograd : New image). -
62
str. : ilustr. ; 25 cm
Tiraž 70. - Registar.
ISBN 978-86-82441-49-6
а) Оптика - Апстракти б) Оптиоелектроника - Апстракти с) Технички
материјали - Апстракти
COBISS.SR-ID 274585868

Effective masses, density of states and conductivities of various dispersions in 2D materials

Vladimir Damljanović¹

(1) Institute of Physics Belgrade, University of Belgrade, Pregrevica 118, 11000 Belgrade, Serbia

Contact: V. Damljanović (damlja@ipb.ac.rs)

Abstract. Within the most simple, Drude model, the electrical conductivity of a crystal is inversely proportional to the electron effective mass and directly proportional to the concentration of free charge carriers [1]. At zero temperature, this concentration is determined by integration of density of states over partially filled energy bands. Situation becomes particularly interesting when the electron effective mass is zero. Dirac, semi-Dirac and Fortune-teller dispersions in 2D materials, support zero electron effective mass along at least one direction in the Brillouin zone. The conductivities of Dirac [2] and semi-Dirac [3] materials are well studied, both experimentally (graphene) and theoretically. On the other hand, the conductivity of recently discovered Fortune teller dispersion [4] remains an open question. In this talk we present conductivity analysis in [2, 3] and speculate that conductivity of the Fortune teller dispersion might be similar, with differences in detail left for future work.

REFERENCES

- [1] N. W. Aschcroft and N. D. Mermin, *Solid State Physics*, Harcourt College, New York (1976).
- [2] Y. V. Bludov, A. Ferreira et al., *Int. J. Mod. Phys. B* **27** (2013), 1341001.
- [3] M. Sanderson, S. Huang et al., *J.Phys. D: Appl. Phys.* **51** (2018), 205302.
- [4] V. Damljanović, I. Popov et al., *Nanoscale* **9** (2017), 19337-19345.

Book of abstracts



PHOTONICA2017

The Sixth International School and Conference on Photonics

& COST actions: MP1406 and MP1402



&H2020-MSCA-RISE-2015 CARDIALLY workshop



28 August – 1 September 2017

Belgrade, Serbia

Editors

Marina Lekić and Aleksandar Krmpot

Institute of Physics Belgrade, Serbia

Belgrade, 2017

ABSTRACTS OF TUTORIAL, KEYNOTE, INVITED LECTURES,
PROGRESS REPORTS AND CONTRIBUTED PAPERS

of

The Sixth International School and Conference on Photonics
PHOTONICA2017

28 August – 1 September 2017
Belgrade Serbia

Editors

Marina Lekić and Aleksandar Krmpot

Technical assistance

Marko Nikolić and Danica Pavlović

Publisher

Institute of Physics Belgrade
Pregrevica 118
11080 Belgrade, Serbia

Printed by

Serbian Academy of Sciences and Arts

Number of copies

300

ISBN 978-86-82441-46-5

An example of two-dimensional crystal structure with semi-Dirac electronic dispersion

V. Damljanović¹ and R. Gajić²

¹*Institute of Physics Belgrade, University of Belgrade, Pregrevica 118, 11080 Belgrade, Serbia*

²*Graphene Laboratory (GLAB) of Center for Solid State Physics and New Materials, Institute of Physics, University of Belgrade, Pregrevica 118, Belgrade, 11080, Serbia*

e-mail: damlja@ipb.ac.rs

In nanophysics, notion “semi-Dirac dispersion” denotes an electronic dispersion which is Dirac-like along certain direction in two-dimensional Brillouin zone (BZ) and quadratic along the orthogonal direction. Semi-Dirac materials are in the focus of research lately due to their intriguing physical properties. These include anisotropic Klein tunneling, characteristic response to magnetic field and peculiar photoresponse to circularly polarized light. To help search for new materials with the semi-Dirac cones, we have recently formulated a set of group-theoretical conditions that allow such dispersion and have provided the list of symmetry groups satisfying them [1]. In present contribution we have considered a tight-binding model on a structure that belongs to diperiodic (layer) group $p11b$ (Dg5). This group belongs to our list [1] and should host the semi-Dirac cones in the vicinity of A and B points in the BZ. We have calculated electronic dispersion in the vicinity of these points. Obtained dispersion is of a semi-Dirac type thus confirming our theory. Here we also discuss other possible candidates for two-dimensional semi-Dirac materials by search Materials project database with particular attention to layered structures published in [2].

REFERENCES

- [1] V. Damljanović, R. Gajić, *J. Phys.: Condens. Matter* 29, 185503 (2017).
- [2] G. Cheon et al., *Nano Letters* 17, 1915 (2017).

Book of abstracts



PHOTONICA2017

The Sixth International School and Conference on Photonics

& COST actions: MP1406 and MP1402



&H2020-MSCA-RISE-2015 CARDIALLY workshop



28 August – 1 September 2017

Belgrade, Serbia

Editors

Marina Lekić and Aleksandar Krmpot

Institute of Physics Belgrade, Serbia

Belgrade, 2017

ABSTRACTS OF TUTORIAL, KEYNOTE, INVITED LECTURES,
PROGRESS REPORTS AND CONTRIBUTED PAPERS

of

The Sixth International School and Conference on Photonics
PHOTONICA2017

28 August – 1 September 2017
Belgrade Serbia

Editors

Marina Lekić and Aleksandar Krmpot

Technical assistance

Marko Nikolić and Danica Pavlović

Publisher

Institute of Physics Belgrade
Pregrevica 118
11080 Belgrade, Serbia

Printed by

Serbian Academy of Sciences and Arts

Number of copies

300

ISBN 978-86-82441-46-5

Bifurcation in reflection spectra of holographic pullulan diffraction grating

S. Savić-Šević, D. Pantelić, V. Damljanović and B. Jelenković

Institute of Physics, University of Belgrade, Pregrevica 118, 11080 Zemun, Belgrade, Serbia
e-mail:savic@ipb.ac.rs

Reflection volume hologram gratings, fabricated using a single-beam method, usually have only one Bragg peak in the spectrum. Z. Wang et al. [1] noted the appearance of multiple peaks in the spectrum of volume diffraction grating recorded in dichromated gelatin, phenomenon that looks like bifurcation within the Bragg plateau. We also observed bifurcation phenomenon in the spectrum of diffraction gratings recorded in dichromated pullulan (DCP), which is a polysaccharide doped with chromium. Compared to dichromated gelatin, the DCP material is simpler to prepare and process, it is insensitive to humidity, thus retaining high resolution and diffraction efficiency [2]. The typical number of appeared peaks in the spectrum is two, three, or four. It was found that a multi-peak phenomenon is accompanied by wider band gap.

In order to understand multi-peak structure of band gaps, experimental results were compared with theoretically predicted results. The theoretical model investigates effects of several important parameters: absorption of radiation within the photosensitive layer, non-uniform thickness of the layer, refractive index modulation and non-uniform spatial period of the grating. Numerical reflection spectra of volume Bragg gratings have been calculated by the method of characteristic matrix [3]. Our model suggests that multi peak structures are produced by uneven modulation of Bragg layers inside the volume hologram. The results of calculation are in agreement with experimental results.

REFERENCES

- [1] Z. Wang, D. Liu, J. Zhou, *Opt. Lett.* 31, 3270 (2006).
- [2] S. Savić-Šević, D. Pantelić, *Applied optics* 46, 287 (2007).
- [3] M. Born, E. Wolf, *Principles of Optics*, Pergamon (1980).

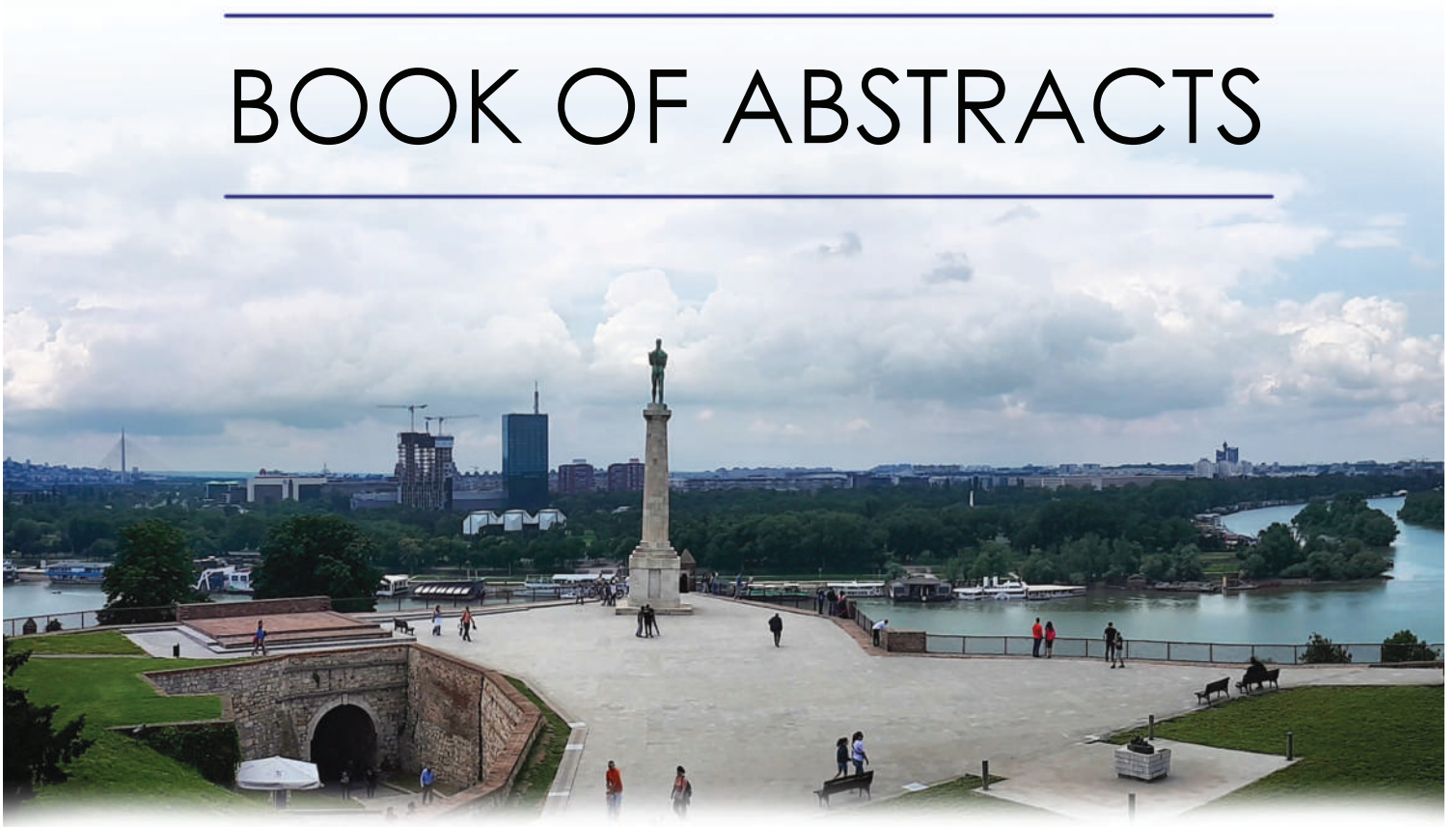
7-11th October 2019
Belgrade, Serbia



<http://www.sfkm.ac.rs/>

The 20th Symposium on Condensed Matter Physics

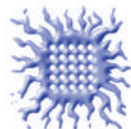
BOOK OF ABSTRACTS



University of Belgrade,
Faculty of Physics



Institute of Physics Belgrade



Vinca Institute
of Nuclear Sciences



Serbian Academy
of Sciences and Arts



Ministry of Education, Science and
Technological Development,
Republic of Serbia

Peculiar Electronic Dispersions in Two-Dimensional Materials Caused by Symmetry

Vladimir Damljanović^a

^a*Institute of Physics Belgrade, University of Belgrade, Pregrevica 118, 11080 Belgrade, Serbia*

Abstract. Two-dimensional materials are spatial atomic arrangements that are periodic in two directions, but are finite in the third, orthogonal direction. Most of their physical properties are determined by the functional dependence of the electronic energy near the Fermi level on the electron wave vector i.e. by the electronic dispersion. Until recently only three types of electronic dispersions were known in two-dimensional materials: Dirac (as in graphene), semi-Dirac (as in black Phosphorus) and quadratic (as in MoS₂). In this talk we show that certain symmetries of non magnetic, time-reversal symmetric, two-dimensional materials with no spin-orbit coupling (SOC) leads unavoidably to new, fourth type of electronic dispersion we called the Fortune teller (FT) dispersion [1]. Even more, inclusion of SOC leads to another type of peculiar electronic dispersion, which is generalization of both Dirac and FT dispersions. The physical properties of materials which these new dispersions induce are still to be investigated theoretically.

REFERENCES

1. Damljanović, V., Popov, I., and Gajić, R., *Nanoscale*. **9**, 19337-19345 (2017).

FUNDAMENTALS
and APPLICATIONS

LIGHT
MATTER
INTERACTIONS *for*

*biophysics
biomedicine
communications
sensors
devices*

WORKSHOP *on*
PHOTONICS

Kopaonik

11.3-14.3.2018.

Organizers

Sponsors



UNIVERZITET U BEOGRADU
Institut za fiziku



Konferencija
**Jedanaesta radionica fotonike
(2018)**

Zbornik apstrakata

Kopaonik, 11–14.3.2018.

Konferencija **Jedanaesta radionica fotonike (2018)**

ZBORNİK APSTRAKATA

Kopaonik 11-14.03.2018.

Izdaje

Institut za fiziku Beograd

Za izdavača

Dr Aleksandar Bogojević, direktor

Urednik

Dr Dragan Lukić

Tiraž

50 primeraka

ISBN 978-86-82441-47-2

Štampa

NEW IMAGE preduzeće d.o.o.

Cara Dušana 212, Zemun, Beograd

Symmetry induced electronic dispersions in two-dimensional materials

Vladimir Damljanović¹

(1) *Institute of Physics Belgrade, University of Belgrade, Pregrevica 118, 11080 Belgrade, Serbia*

Contact: V. Damljanović (damlja@ipb.ac.rs)


Abstract. Two-dimensional (2D) materials are arrangements of atomic ions which are periodic in two spatial directions but finite in the third, orthogonal direction. Recent examples of such materials include graphene, silicene, transition metal dichalcogenide monolayers etc. Any 2D material belongs to one of eighty, so-called layer (or diperiodic) symmetry groups. In this talk, a deep connection between various types of famous electronic dispersions (Dirac, semi-Dirac, quadratic etc.) in a certain 2D material and a layer group to which the material belongs, is presented. In addition, previously unknown type of electronic dispersion obtained by applying symmetry arguments is also presented. Our talk is based on recently published results [1-4] referring to non-magnetic 2D materials with negligible spin-orbit coupling.

REFERENCES

- [1] V. Damljanović, R. Gajić, *J. Phys.: Cond. Matt.* **28** (2016), 085502.
- [2] V. Damljanović, R. Gajić, *J. Phys.: Cond. Matt.* **28** (2016), 439401.
- [3] V. Damljanović, R. Gajić, *J. Phys.: Cond. Matt.* **29** (2017), 185503.
- [4] V. Damljanović, I. Popov, R. Gajić, *Nanoscale* **9** (2017), 19337-19345

Article

Ab Initio Study of the Electronic, Vibrational, and Mechanical Properties of the Magnesium Diboride Monolayer

Jelena Pešić^{1,*}, Igor Popov^{1,2}, Andrijana Šolajić¹, Vladimir Damljanović¹, Kurt Hingerl³, Milivoj Belić⁴ and Radoš Gajić¹

¹ Laboratory for graphene, other 2D materials and ordered nanostructures, Center for Solid State Physics and New Materials, Institute of Physics Belgrade, University of Belgrade, 11080 Belgrade, Serbia; popov@ipb.ac.rs (I.P.); solajic@ipb.ac.rs (A.Š.); damlja@ipb.ac.rs (V.D.); rgajic@ipb.ac.rs (R.G.)

² Institute for Multidisciplinary Research, University of Belgrade, Kneza Višeslava 1, 11030 Belgrade, Serbia

³ Center for Surface and Nanoanalytics, Johannes Kepler University, 4040 Linz, Austria; Kurt.Hingerl@jku.at

⁴ Science Program, Texas A&M University at Qatar, P.O. Box 23874, Doha, Qatar; milivoj.belic@qatar.tamu.edu

* Correspondence: yelena@ipb.ac.rs

Received: 15 March 2019; Accepted: 1 April 2019; Published: 2 April 2019



Abstract: Magnesium diboride gained significant interest in the materials science community after the discovery of its superconductivity, with an unusually high critical temperature of 39 K. Many aspects of the electronic properties and superconductivity of bulk MgB₂ and thin sheets of MgB₂ have been determined; however, a single layer of MgB₂ has not yet been fully theoretically investigated. Here, we present a detailed study of the structural, electronic, vibrational, and elastic properties of monolayer MgB₂, based on ab initio methods. First-principles calculations reveal the importance of reduction of dimensionality on the properties of MgB₂ and thoroughly describe the properties of this novel 2D material. The presence of a negative Poisson ratio, higher density of states at the Fermi level, and a good dynamic stability under strain make the MgB₂ monolayer a prominent material, both for fundamental research and application studies.

Keywords: magnesium diboride; 2D materials; density functional theory

PACS: 71.15.Mb; 74.70.Ad

1. INTRODUCTION

Magnesium diboride was first synthesized and had its structure confirmed in 1953 [1]. An interest in its properties has grown ever since 2001, when it was discovered that MgB₂ exhibits the highest superconducting transition temperature T_c of all metallic superconductors. It is an inter-metallic s-wave compound superconductor with a quasi-two dimensional character [2] and a critical temperature of superconductive transition at $T_c = 39$ K. The experimental confirmation of the isotope effect [3] in MgB₂ indicated that it is a phonon-mediated BCS superconductor. A better definition would describe MgB₂ as self-doped semimetal with a crucial σ -bonding band that is nearly filled [4]. The basic aspects of the electronic structure and pairing is in a rather strong coupling of high frequency boron–boron stretch modes to the bonding electronic boron–boron states at the Fermi surface. The phonon-mediated mechanism with different coupling strengths between a particular phonon mode and selected electronic bands, boron σ - and π -bands [5–13], results in the presence of two superconducting gaps at the Fermi level. MgB₂ has already been fabricated in bulk, as single crystals, and as a thin film, and shows potential for practical applications.

The discovery of graphene in 2004 [14] sparked an interest in 2D materials and their properties. A variety of new properties, which distinguished graphene from graphite [14–22], inspired a search for other low-dimensional limits of layered materials and possibilities they offered. Interest in a low-dimensional limit of MgB_2 has arisen in past years, showing that it is superconductive even in a monolayer [23,24].

MgB_2 has a distinct layer structure, where boron atoms form a honeycomb layer and magnesium atoms are located above the center of the hexagons, between every boron plane. The boron layers alternate with a triangular lattice of magnesium layers. There is a noticeable structural similarity of MgB_2 to graphite-intercalated compounds (GICs), some of which also exhibit superconductivity [25–29]. Both monolayer and two-layer graphene, decorated/intercalated with atoms of alkali and alkaline earth metals, exhibit superconductivity and have been thoroughly studied using ab initio methods and isotropic and anisotropic Eliashberg theory [30–32].

Furthermore, a similarity in the electronic structure between GICs and MgB_2 exists. The peculiar and unique property of MgB_2 is a consequence of the incomplete filling of two σ bands corresponding to strongly covalent sp^2 -hybrid bonding within the graphite-like boron layers [33].

Here, we present a comprehensive study of the electronic, vibrational, and mechanical properties of MgB_2 using ab initio methods, in order to provide its detail description.

2. Computational Details

MgB_2 has a hexagonal unit cell and consists of graphite-like B_2 layers stacked with the Mg atoms in between, as shown in Figure 1. The first-principles calculations were performed within the density functional theory (DFT) formalism, using a general gradient approximation (GGA) to calculate the electronic structure. For all electronic and phonon structure, the Quantum Espresso software package [34] was used with ultra-soft pseudopotentials and a plane-wave cutoff energy of 30 Ry. All calculated structures are relaxed to their minimum energy configuration, following the internal force on atoms and stress tensor of the unit cell. We used the Monkhorst-Pack $48 \times 48 \times 48$ and $40 \times 40 \times 1$ k-meshes, for the calculations of the electronic structure of the MgB_2 bulk and MgB_2 monolayer, respectively. The phonon frequencies are calculated using Density Functional Perturbation Theory (DFPT) on the $12 \times 12 \times 12$ and $20 \times 20 \times 1$ phonon wave vector mesh for the bulk and monolayer structures, respectively. In two-dimensional systems, the van der Waals (vdW) interaction was found to play an important role on the electronic structure [35]; however, as this is study on monolayer MgB_2 , we do not treat vdW interactions, especially since, in this case, the effects are minor and including them would add additional computational costs but would not yield more accurate results.

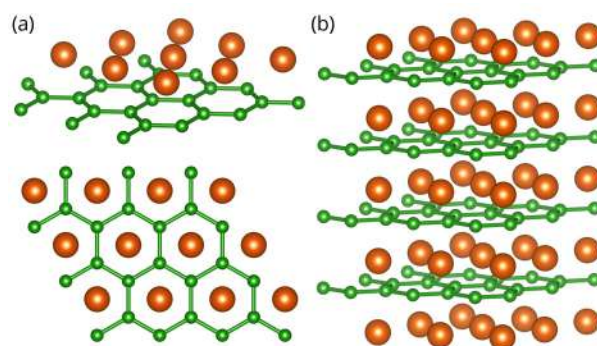


Figure 1. Crystal structure of the MgB_2 monolayer (a) and bulk MgB_2 (b), with a hexagonal unit cell. Green (orange) spheres represent Boron (Magnesium) atoms. Color online.

The crystal structure of MgB_2 and the MgB_2 monolayer are presented in Figure 1. The lattice parameters for the bulk MgB_2 are in agreement with the experimental results, $a = 3.083 \text{ \AA}$ and $c/a = 1.142$ [9]. In order to avoid an interlayer interaction due to the periodicity and to simulate a 2D

material, an artificial vacuum layer was set to be 25 Å. When the monolayer is modelled, the structure is geometrically optimized, allowing the atoms to reach a minimum potential energy state. The bond length between neighbouring atoms remained to be 1.78 Å, but the distance from the boron layer to the Mg atoms changed from $h = 1.76$ Å to $h = 1.60$ Å.

For the molecular dynamics (MD) study, the Siesta code was utilized [36]. The super-cell is built by repeating the unit cell three times in both in-plane directions, whereas the lattice vector in the perpendicular direction is 15 Å, providing a large enough vacuum space between the 2D material and its periodic replica in order to avoid their mutual interaction. The lattice parameters and the geometry of the unit cell are initially optimized using the conjugate gradient method. The Perdew-Burke-Ernzerhof form of the exchange-correlation functional [37], the double-zeta polarized basis set, and the Troulier-Martins pseudopotentials [38] were used in all MD calculations.

The second-order elastic constants were calculated using the ElaStic software package [39]. First, the direction is projected from the strain tensor and total energies for each deformation are calculated. Elastic constants are then calculated using the second derivatives of the energy curves, dependent on the parameter η . In our calculations, the maximum positive and negative amplitudes of 5% Lagrangian strain were applied, with a step of 0.1%.

For the 2D square, rectangular, or hexagonal lattices, the non-zero second-order elastic constants, in Voigt notation, are c_{11} , c_{22} , c_{12} , and c_{66} . Due to symmetry, in hexagonal structures $c_{11} = c_{22}$ and $c_{66} = \frac{1}{2}(c_{11} - c_{12})$; so, we have 2 independent elastic constants. The layer modulus, which represents the resistance of a 2D material to stretching, is given as

$$\gamma = \frac{1}{4}(c_{11} + c_{22} + 2c_{12}).$$

The 2D Young modulus Y for strains in the (10) and (01) directions, Poisson's ratio ν and the shear modulus G are obtained from the following relations,

$$Y = \frac{c_{11}^2 - c_{12}^2}{c_{11}}, \quad \nu = \frac{c_{12}}{c_{22}}, \quad G = c_{66}.$$

Units for elastic constants and those parameters are N/m.

3. Results and Discussion

In order to determine the stability of a single layer of MgB₂, we perform MD simulations based on DFT and the super-cell approach. Besides the system with optimized (pristine) lattice parameters, we also consider a biaxially stretched system (up to 3% of tensile strain) and biaxially compressed system (up to 5% of compressive strain). The MD simulations are conducted in the range of temperatures between 50–300 K, with a step of 50 K, using the Nosé–Hoover thermostat [40].

Figure 2a shows the average distance between Mg and B atomic layers, as evolved over a time of 1 ps. Throughout the simulation time, there is no further evolution of the z-coordinate and the Mg atom shows only oscillatory movement around the equilibrium positions (as is shown in Figure 2) Importantly, the separation indicates that the Mg atoms do not leave the surface of the MgB₂ crystal. The plane in which the Mg atoms reside shifts away from the plane of the B atoms on average by 0.09 Å in a compressed crystal, while the distance between the planes decreases on average by 0.42 Å in the stretched system. This (relatively larger) shift in the latter case can be understood by analysing the details of the MgB₂ atomic structure. When the crystal is biaxially stretched, its Mg–B bond lengths increase, which is partially compensated by the nesting of the Mg atoms in the hollow sites closer to the B sublattice. Despite these atomic shifts, the MD simulations show the structural stability of the system. The stability from the MD simulations can be further quantitatively derived from the global Lindemann index, the dependence of which on temperature is shown in Figure 2b. It is calculated

for the pristine crystal, with a compressive strain of 5% and a tensile strain of 3%, from the local Lindemann indices, given by the formula

$$q_i = \frac{1}{N-1} \sum_{j \neq i} \frac{\sqrt{\langle r_{ij}^2 \rangle - \langle r_{ij} \rangle^2}}{\langle r_{ij} \rangle},$$

by averaging over all atoms. Here q_i is the local Lindemann index of atom i , N is number of atoms, r_{ij} is a separation between atoms i and j , and the angle brackets denote averaging over time (i.e., MD steps) [41]. The linear behaviour of the Lindemann indices indicate that systems are stable, at least up to room temperature.

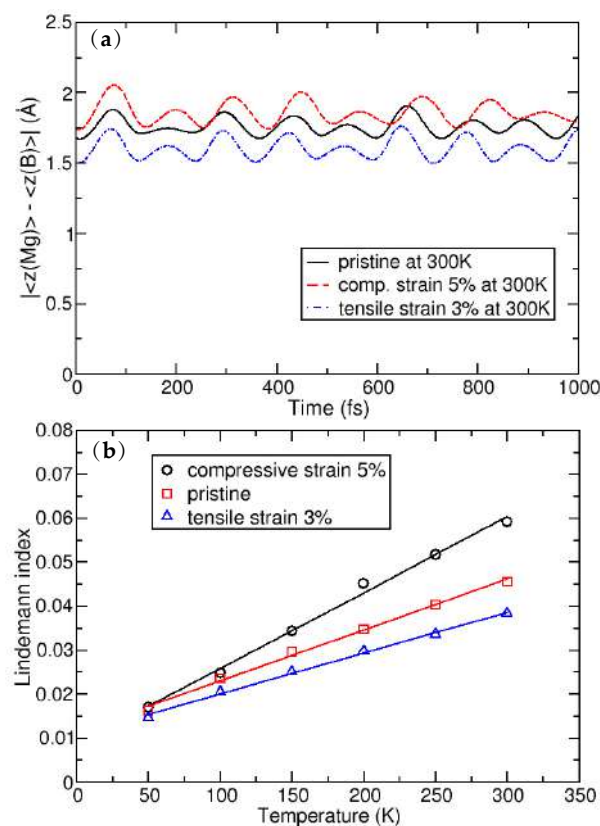


Figure 2. (a): Average distance between the Mg and B atomic layers; and (b): the dependence of the global Lindemann index as a function of temperature.

The calculated second-order elastic constants and other structural parameters for monolayer MgB_2 are given in Table 1. All elastic constants related to the bulk material (those that have 3, 4, or 5 in their subscripts), are calculated close to zero, as is expected for the monolayer. Compared to similar 2D materials, the layer modulus of MgB_2 of 30.18 N/m is relatively small (in the range of Silicene and Germanene), roughly five times smaller than that of graphene or h-BN, for example [42,43]. Similar results are obtained for the Young modulus. Compared to borophene (two-dimensional boron sheets with rectangular structures) [44], which is a hard and brittle 2D material that exhibits an extremely large Young’s modulus of 398 N/m along the a direction [45], the MgB_2 monolayer has a significantly smaller value of 63.29 N/m. The most interesting observation in the elastic properties of the MgB_2 monolayer is that the c_{12} constant is negative, which gives a negative Poisson ratio in the a and b directions, too—although, with a very small negative value of -0.05 . However, compared to 2D borophene, which has an out-of-plane negative Poisson’s ratio (that effectively holds the strong boron bonds lying along the a direction and makes the boron sheet show superior mechanical flexibility

along the b direction [46]), we obtain similar values [45]. For comparison, graphene has a Young modulus of 352.2 N/m and a Poisson ratio of 0.185 [42]. After confirming its stability and determining the elastic properties of the MgB_2 monolayer, we study its electronic properties. In Figure 3, the electronic structures of bulk MgB_2 and the MgB_2 monolayer are presented. The band structures for the bulk along the high-symmetry points Γ -K-M- Γ -A-L, and for the monolayer along Γ -K-M- Γ were calculated. The Fermi level is set to zero. The band structure of the bulk is in full agreement with previous studies [10,47–49]. The two bands crossing the Fermi level play a crucial role in the electronic properties of MgB_2 . The density of the states around E_f are predominantly related to the B atoms and their p -orbitals, whereas the Mg atom contribution is negligible in this region. Previous studies described Mg as fully ionized and showed that the electrons donated to the system are not localized on the anion but, rather, are distributed over the whole crystal [6]. A similarity to graphite can be observed, with three σ bands, corresponding to the in-plane sp_xp_y (sp^2) hybridization in the boron layer and two π -bands of boron p_z orbitals [33]. Boron $p_{x(y)}$ and p_z orbitals contribute as σ and π states. Analysing projected DOS, one concludes that the σ states are considerably involved in the total density of states at the Fermi level, while the π states have only a partial contribution. It is worth emphasizing that the bulk bands of this material at the K-point above the Fermi level present a formation similar to the Dirac cones in graphene.

In the monolayer, there is an increase in the total density of states at the Fermi level from $N(E_f)_{bulk} = 0.72$ states/eV to $N(E_f)_{mono} = 0.97$ states/eV. In the same manner as in the bulk, the monolayer Mg atoms negligibly contribute to the density of states at the Fermi level, and the main contribution comes from the B p -orbitals. The characteristic Dirac cone-like structure is still present and closer to the Fermi level. $Dg77$, as the symmetry group of the MgB_2 monolayer, hosts a Dirac-like dispersion in the vicinity of the K-point in the hexagonal Brillouin zone, if the orbital wave functions belong to the 2D representation E of the C_{3v} point group of the wave vector [50,51]. In the tight-binding case, the p_x and p_y orbitals of two boron ions give rise to one E-representation (and to two one-dimensional representations), while the s-orbitals form a basis for one E-representation and p_z -orbitals form a basis for one E-representation as well. This explains the presence of the Dirac cones at the K-point in the band structure of the MgB_2 monolayer (as shown in Figure 3b).

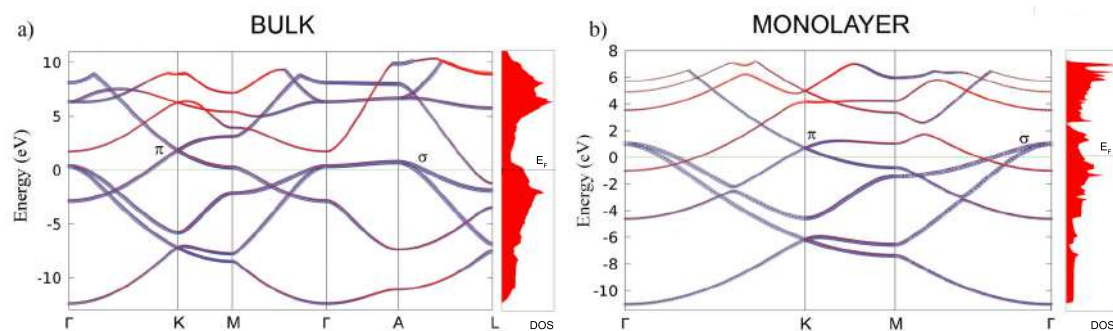


Figure 3. The electronic band structure and total density of states in bulk MgB_2 (a) and the MgB_2 monolayer (b). The blue and red colors represent the B and Mg atoms contributions to the electronic dispersion, respectively.

Table 1. The calculated elastic stiffness constants, layer modulus γ , Young’s modulus Y , Poisson’s ratio ν , and shear modulus G for the MgB_2 monolayer. All parameters are in units of N/m.

c_{11}	c_{12}	c_{66}	γ	Y	ν	G
63.4	−3.1	33.3	30.18	63.29	−0.05	33.3

Figure 4 shows the phonon dispersions for both the bulk and monolayer. For the bulk (in Figure 4a), there are four optical modes at the Γ point. Due to the light atomic mass of the B

atoms and the strong B–B coupling, the two high-frequency modes almost have a pure boron character. The in-plane stretching mode E_{2g} and the out-of-plane mode (where the atoms move in opposite directions B_{1g}) are the boron atom modes. E_{2g} is a doubly-degenerate Raman active mode and experimental studies [6,9] showed that this mode is very sensitive to structural changes and it has a strong electron-phonon coupling. The low-frequency modes (A_{2u}) and double degenerate (E_{1u}) are infrared active and they do not involve changes on in-plane bonds. In Figure 4b, the phonon dispersion of the MgB_2 monolayer is presented. In the phonon spectrum there are no imaginary frequencies, which confirms, once again, the dynamical stability of the system (also demonstrated earlier by the MD calculations).

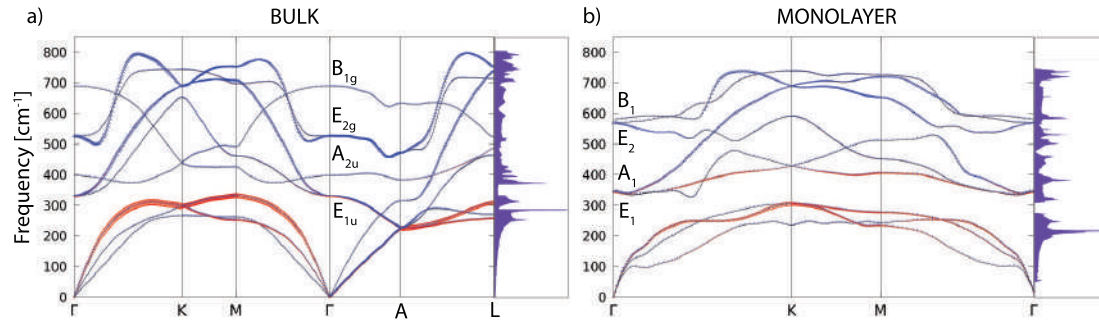


Figure 4. The phonon dispersion and the phonon density of states for the MgB_2 bulk (a) and monolayer (b). The blue and red colours represent the B and Mg atom contributions in the phonon dispersion, respectively.

At the Γ point, there are three acoustic and six optical modes (from which two pairs are doubly degenerate). The optical modes A_1 , B_1 , E_1 , and E_2 are related to the optical modes of the parent material. Two significant differences between the bulk and monolayer spectrum can be observed: The E_1 and A_1 mode become energy degenerate in the monolayer, resulting in either a slight softening (hardening) of the modes which leads to nearly equal frequencies, which opens a gap in the phonon density of states (DOS) between the acoustic and optical modes. A more significant effect concerns the softening of the B_1 mode and hardening of the E_2 mode. As in the bulk E_{2g} mode, the monolayer E_2 mode is strongly coupled to electrons, causing the superconductivity in the monolayer in a similar fashion as in the bulk. In Figure 5, the vibrational frequencies and normal coordinates for the MgB_2 monolayer are presented. The symmetry group is C_{6v} , and the acoustic modes are A_1 and E_1 . The optical modes at the Γ point are A_1 , B_1 , E_1 , and E_2 , where the infrared-active ones are A_1 and E_1 . The Raman-active modes are A_1 , E_1 , and E_2 , and B_1 is silent. In Table 2, the Raman tensor for the MgB_2 monolayer is presented [52]. Similar to graphene, the phonon eigenvectors and the normal coordinates at the Γ -point are determined by symmetry rules and, therefore, are a model independent.

Table 2. Raman tensor of the MgB_2 monolayer.

		Raman Tensors			
MgB₂-mono $Dg77 = TC_{6v}$ $O_z \parallel C_6$ $O_x \parallel \sigma_v$	A_1	E_1	E_2		
	$\begin{pmatrix} a & 0 & 0 \\ 0 & a & 0 \\ 0 & 0 & b \end{pmatrix}$	$\begin{pmatrix} 0 & 0 & c \\ 0 & 0 & 0 \\ c & 0 & 0 \end{pmatrix}$	$\begin{pmatrix} 0 & 0 & 0 \\ 0 & 0 & c \\ 0 & c & 0 \end{pmatrix}$	$\begin{pmatrix} d & 0 & 0 \\ 0 & -d & 0 \\ 0 & 0 & 0 \end{pmatrix}$	$\begin{pmatrix} 0 & -d & 0 \\ -d & 0 & 0 \\ 0 & 0 & 0 \end{pmatrix}$

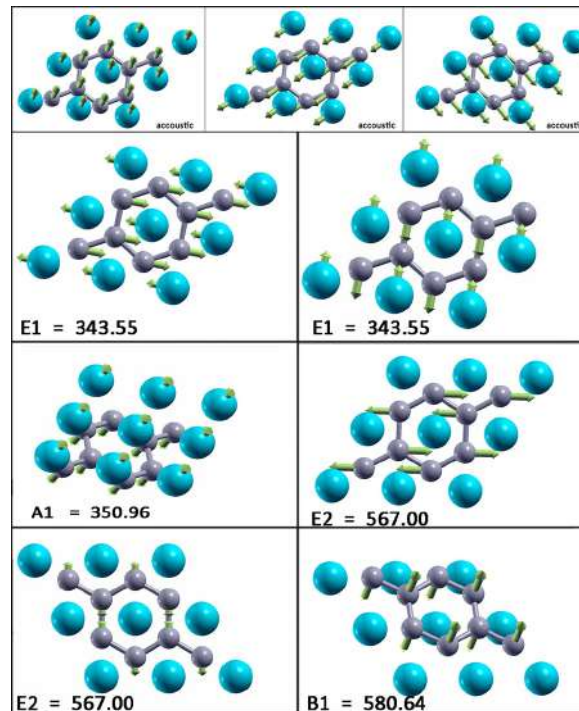


Figure 5. Vibrational frequencies (in wavenumbers) and the vibration normal coordinates at Γ for the MgB_2 monolayer.

4. Conclusions

The electronic band structure, density of states, phonon dispersion, and elastic constants have been calculated for the MgB_2 monolayer and compared to the bulk material, using first-principles calculations within the DFT framework. We demonstrated an increase of electronic density of states at the Fermi level in the monolayer (compared to the bulk) and determined its stability under various strains. These two features are crucial for the enhancement of electron–phonon coupling and they enable significant mechanical modification that increases the critical superconducting temperature. Establishing stability and offering insight into this novel 2D material, we focus on the effects of ultimate lowering of the dimensionality. The question of reduction of dimensionality to its limit, a truly atomic-scale 2D system, and the consequences of this [53–61] are highly relevant, not only to fundamental science but also to applications in nanotechnology.

Author Contributions: Conceptualization, J.P. and R.G.; Validation, K.H., M.B., R.G.; Investigation, J.P., I.P., A.Š. and V.D.; Writing—Original Draft Preparation, J.P., I.P., A.Š. and V.D.; Writing—Review & Editing, J.P.; Supervision, R.G.; Funding Acquisition, K.H., M.B. and R.G.

Funding: This research is supported by Serbian Ministry of Education, Science and Technological Development under projects OI 171005, III 45018, and III 45016 and by the Qatar National Research Fund, cycle 11, under grant number NPRP 11S-1126-170033. K. H. acknowledges the support of the European Commission under the H2020 grant TWINFUSYON.GA692034.

Acknowledgments: The DFT calculations were performed using the computational resources at Johannes Kepler University, Linz, Austria. This work was supported by the Serbian Ministry of Education, Science and Technological Development under projects OI 171005, III 45018, and III 45016.

Conflicts of Interest: The authors declare no conflict of interest.

References

1. Jones, M.E.; Marsh R.E. The preparation and structure of magnesium boride, MgB₂. *J. Am. Chem. Soc.* **1953**, *76*, 5.
2. Nagamatsu, J.; Nakagawa, N.; Muranaka, T.; Zenitani, Y.; Akimitsu, J. Superconductivity at 39 K in magnesium diboride. *Nature* **2001**, *410*, 63.
3. Bud'ko, S.L.; Lapertot, G.; Petrovic, C.; Cunningham, C.E.; Anderson, N.; Canfield, P.C. Boron Isotope Effect in Superconducting MgB₂. *Phys. Rev. Lett.* **2001**, *86*, 1877.
4. Pickett, W. Superconductivity: 2D Physics, Unknown Mechanisms, Current Puzzles. *Emerg. Phenom. Correl. Matter Lect. Notes Autumn School Corr. Electron.* **2013**, *2013*, 45.
5. Choi, H.J.; Roundy, D.; Sun, H.; Cohen, M.L.; Steven Louie, G. The origin of the anomalous superconducting properties of MgB₂. *Nature* **2002**, *418*, 758.
6. Kortus, J.; Mazin, I.I.; Belaichenko, K.D.; Antropov, V.P.; Boyer, L.L. Superconductivity of Metallic Boron in MgB₂. *Phys. Rev. Lett.* **2001**, *86*, 4656.
7. An, J.M.; Pickett, W.E. Superconductivity of MgB₂: Covalent Bonds Driven Metallic. *Phys. Rev. Lett.* **2001**, *86*, 4366.
8. Liu, A.Y.; Mazin, I.I.; Kortus, J. Beyond Eliashberg Superconductivity in MgB₂: Anharmonicity, Two-Phonon Scattering, and Multiple Gaps. *Phys. Rev. Lett.* **2001**, *87*, 087005.
9. Kong, Y.; Dolgov, O.V.; Jepsen, O.; Andersen, O.K. Electron-phonon interaction in the normal and superconducting states of MgB₂. *Phys. Rev. B* **2001**, *64*, 020501.
10. Bohnen, K.-P.; Heid, R.; Renker, B. Phonon Dispersion and Electron-Phonon Coupling in MgB₂ and AlB₂. *Phys. Rev. Lett.* **2001**, *86*, 5771.
11. Kunc, K.; Loa, I.; Syassen, K.; Kremer, R.K.; Ahn, K. MgB₂ under pressure: phonon calculations, Raman spectroscopy, and optical reflectance. *J. Phys. Condens. Matter* **2001**, *13*, 9945.
12. Choi, H.J.; Roundy, D.; Sun, H.; Cohen, M.L.; Louie, S.G. First-principles calculation of the superconducting transition in MgB₂ within the anisotropic Eliashberg formalism. *Phys. Rev. B* **2002**, *66*, 020513.
13. Canfield, P.C.; Crabtree, G.W. Magnesium Diboride: Better Late than Never. *Phys. Today* **2003**, *56*, 34.
14. Novoselov, K.S.; Geim, A.K.; Morozov, S.V.; Jiang, D.; Zhang, Y.; Dubonos, S.V.; Grigorieva, I.V.; Firsov, A.A. Electric Field Effect in Atomically Thin Carbon Films. *Science* **2004**, *306*, 666–669.
15. Katsnelson, M.I.; Novoselov, K.S.; Geim, A.K. Chiral tunnelling and the Klein paradox in graphene. *Nat. Phys.* **2006**, *2*, 620–625.
16. Katsnelson, M.I. Zitterbewegung, chirality, and minimal conductivity in graphene. *Eur. Phys. J. B* **2006**, *51*, 157–160.
17. Rusin, T.M.; Zawadzki, W. Zitterbewegung of electrons in graphene in a magnetic field. *Phys. Rev. B* **2008**, *78*, 125419.
18. Pisana, S.; Lazzeri, M.; Casiraghi, C.; Novoselov, K.S.; Geim, A.K.; Ferrari, A.C.; Mauri, F. Breakdown of the adiabatic Born-Oppenheimer approximation in graphene. *Nat. Mater.* **2007**, *6*, 198–201.
19. Piscanec, S.; Lazzeri, M.; Mauri, F.; Ferrari, A.C.; Robertson, J. Kohn Anomalies and Electron-Phonon Interactions in Graphite. *Phys. Rev. Lett.* **2004**, *93*, 85503.
20. Novoselov, K.S.; Jiang, Z.; Zhang, Y.; Morozov, S.V.; Stormer, H.L.; Zeitler, U.; Maan, J.C.; Boebinger, G.S.; Kim, P.; Geim, A.K. Room-temperature quantum Hall effect in graphene. *Science* **2007**, *315*, 1379.
21. Zhou, S.Y.; Gweon, G.-H.; Fedorov, A.V.; First, P.N.; de Heer, W.A.; Lee, D.-H.; Guinea, F.; Castro Neto, A.H.; Lanzara, A.; et al. Substrate-induced bandgap opening in epitaxial graphene. *Nat. Mater.* **2007**, *6*, 770–775.
22. Zhang, Y.; Tan, Y.; Stormer, H.L.; Kim, P. Experimental observation of the quantum Hall effect and Berry's phase in graphene. *Nature* **2005**, *438*, 201–204.
23. Bekaert, J.; Aperis, A.; Partoens, B. Oppeneer, P.M.; Milošević, M.V. Evolution of multigap superconductivity in the atomically thin limit: Strain-enhanced three-gap superconductivity in monolayer MgB₂. *Phys. Rev. B* **2017**, *96*, 094510.
24. Morshedloo, T.; Roknabadi, M.R.; Behdani, M. First-principles study of the superconductivity in MgB₂ bulk and in its bilayer thin film based on electron-phonon coupling. *Physica C* **2015**, *509*, doi:10.1016/j.physc.2014.11.006.
25. Calandra, M.; Profeta, G.; Mauri, F. Superconductivity in metal-coated graphene. *Phys. Status Solidi (b)* **2012**, *249*, 2544.

26. Ludbrook, B.M.; Levy, G.; Nigge, P.; Zonno, M.; Schneider, M.; Dvorak, D.J.; Veenstra, C.N.; Zhdanovich, S.; Wong, D.; Dosanjh, P.; et al. Evidence for superconductivity in Li-decorated monolayer graphene. *Proc. Natl. Acad. Sci. USA* **2015**, *112*, 11795.
27. Profeta, G.; Calandra, M.; Mauri, F. Phonon-mediated superconductivity in graphene by lithium deposition. *Nat. Phys.* **2012**, *8*, 131–134.
28. Pešić, J.; Gajić, R.; Hingerl, K.; Belić, M. Strain-enhanced superconductivity in Li-doped graphene. *Europhys. Lett.* **2014**, *108*, 67005.
29. Szczesniak, D.; Durajski, A.P.; Szczesniak, R. Influence of lithium doping on the thermodynamic properties of graphene based superconductors. *J. Phys-Condens. Mat.* **2014**, *26*, 255701.
30. Durajski, A.; Skoczylas, K.; Szczesniak, R. Superconductivity in bilayer graphene intercalated with alkali and alkaline earth metals. *Phys. Chem. Chem. Phys.* **2019**, *21*, 5925.
31. Zheng, J.-J.; Margine, E.R. First-principles calculations of the superconducting properties in Li-decorated monolayer graphene within the anisotropic Migdal-Eliashberg formalism. *Phys. Rev. B* **2016**, *94*, 064509.
32. Margine, E.R.; Lambert, H.; Giustino, F. Electron-phonon interaction and pairing mechanism in superconducting Ca-intercalated bilayer graphene. *Sci. Rep.* **2016**, *6*, 21414.
33. Mazin, I.I.; Antropov, V.P. Electronic structure, electron–phonon coupling, and multiband effects in MgB₂. *Phys. C Supercond.* **2003**, *385*, 49–65.
34. Giannozzi, P.; Andreussi, O.; Brumme, T.; Bunau, O.; Buongiorno, N.M.; Calandra, M.; Car, R.; Cavazzoni, C.; Ceresoli, D.; Cococcioni, M. et al. Quantum espresso: A modular and open-source software project for quantum simulations of materials. *J. Phys. Condensed Matter* **2009**, *21*, 395502.
35. Lu, N.; Guo, H.; Zhuo, Z.; Wang, L.; Wu, X.; Zeng, X.C. Twisted MX₂/MoS₂ heterobilayers: effect of van der Waals interaction on the electronic structure. *Nanoscale* **2017**, *9*, 19131–19138.
36. Soler, J.M.; Artacho, E.; Gale, J.D.; García, A.; Junquera, J.; Ordejón, P.; Sánchez-Portal, D. The SIESTA method for ab initio order-N materials simulation. *J. Phys. Condens. Matter.* **2002**, *14*, 2745.
37. Perdew, J.P.; Burke, K.; Ernzerhof, M. Generalized Gradient Approximation Made Simple. *Phys. Rev. Lett.* **1996**, *77*, 3865–3868.
38. N. Troullier; Martins, J.L. Efficient pseudopotentials for plane-wave calculations. *Phys. Rev. B* **1991**, *43*, 1993–2006, doi:10.1103/PhysRevB.43.1993.
39. Golezorkhtabar, R.; Pavone, P.; Spitaler, J.; Puschnig, P.; Draxl, C. ElaStic: A tool for calculating second-order elastic constants from first principles. *Comput. Phys. Commun.* **2013**, *184*, 1861–1873.
40. Nosé, S. A unified formulation of the constant temperature molecular dynamics methods. *J. Chem. Phys.* **1984**, *81*, 511.
41. Lindemann, F.A. The calculation of molecular vibration frequencies. *Phys. Z.* **1910**, *11*, 609.
42. Andrew, R.C.; Mapasha, R.E.; Ukpong, A.M.; Chetty, N. Mechanical properties of graphene and boronitrene. *Phys. Rev. B* **2012**, *85*, 125428.
43. Zhang, Z.; Yang, Y.; Penev, E.S.; Yakobson, B.I. Elasticity, Flexibility, and Ideal Strength of Borophenes. *Adv. Func. Mater.* **2017**, *27*, 1605059.
44. Zhong, H.; Huang, K.; Yu, G.; Yuan, S. Electronic and mechanical properties of few-layer borophene. *Phys. Rev. B* **2018**, *98*, 054104.
45. Mannix, A.J.; Zhou, X.F.; Kiraly, B.; Wood, J.D.; Alducin, D.; Myers, B.D.; Liu, X.; Fisher, B.L.; Santiago, U.; Guest, J.R.; et al. Synthesis of borophenes: Anisotropic, two-dimensional boron polymorphs. *Science* **2015**, *350*, 1513–1516.
46. Wang, H.; Li, Q.; Gao, Y.; Miao, F.; Zhou, X.-F.; Wan, X.G. Strain effects on borophene: ideal strength, negative Poisson's ratio and phonon instability. *New J. Phys.* **2016**, *18*, 073016.
47. De la Pena-Seaman, O.; de Cross, R.; Heid, R.; Bohnen, K.-P. Effects of Al and C doping on the electronic structure and phonon renormalization in MgB₂. *Phys. Rev. B* **2009**, *79*, 134523.
48. Ponce, S.; Margine, E.R.; Verdi, C.; Giustino, F. EPW: Electron-phonon coupling, transport and superconducting properties using maximally localized Wannier functions. *Comp. Phys. Commun.* **2016**, *209*, 116–133.
49. Margine, E.R.; Giustino, F. Anisotropic Migdal-Eliashberg theory using Wannier functions. *Phys. Rev. B* **2013**, *87*, 024505.
50. Damljanovic, V.; Gajic, R. Existence of Dirac cones in the Brillouin zone of diperiodic atomic crystals according to group theory. *J. Phys. Condens. Matter* **2016**, *28*, 085502.

51. Damljanovic, V.; Gajic, R. Addendum to 'Existence of Dirac cones in the Brillouin zone of diperiodic atomic crystals according to group theory'. *J. Phys. Condens. Matter* **2016**, *28*, 439401.
52. Poulet, H.; Mathieu, J.P. *Vibration Spectra and Symmetry of Crystals*; Gordon and Breach: New York, NY, USA, 1976.
53. Szalowski, K. Critical temperature of MgB₂ ultrathin superconducting films: BCS model calculations in the tight-binding approximation. *Phys. Rev. B* **2006**, *74*, 094501.
54. Zhang, C.; Wang, Y.; Wang, D.; Zhang, Y.; Liu, Z.-H.; Feng, Q.-R.; Gan, Z.-Z. Suppression of superconductivity in epitaxial MgB₂ ultrathin films. *J. Appl. Phys.* **2013**, *114*, 023903.
55. Ao, B.; Zhang, Z.; Tang, T.; Zhao, Y. Potential enhancement of superconductivity in MgB₂ nanosheets: First-principles calculations. *Chem. Phys. Lett.* **2014**, *591*, 185–188.
56. Romero-Bermudez, A.; Garcia-Garcia, A.M. Shape resonances and shell effects in thin-film multiband superconductors. *Phys. Rev. B* **2014**, *89*, 024510.
57. Romero-Bermudez, A.; Garcia-Garcia, A.M. Size effects in superconducting thin films coupled to a substrate. *Phys. Rev. B* **2014**, *89*, 064508.
58. Acharya, N.; Wolak, M.A.; Cunnane, D.P.; Karasik, B.S.; Xi, X.X. MgB₂ ultrathin films fabricated by hybrid physical chemical vapor deposition and ion milling. *APL Mater.* **2016**, *4*, 086114.
59. Valentinis, D.; van der Marel, D.; Berthod, C. Rise and fall of shape resonances in thin films of BCS superconductors. *Phys. Rev. B* **2016**, *94*, 054516.
60. Narlikar, A.V. Small Superconductors: Introduction. In *The Oxford Handbook of Small Superconductors*, 1st ed., Narlikar, A.V., Ed.; Oxford University Press: Oxford, UK, 2017.
61. Gariglio, S.; Scheurer, M.; Schmalian, J.; Monteiro, A.M.R.V.L.; Goswami, S.; Caviglia, A. Surface and Interface Superconductivity. In *The Oxford Handbook of Small Superconductors*, 1st ed.; Narlikar, A.V., Ed.; Oxford University Press: Oxford, UK, 2017.



© 2019 by the authors. Licensee MDPI, Basel, Switzerland. This article is an open access article distributed under the terms and conditions of the Creative Commons Attribution (CC BY) license (<http://creativecommons.org/licenses/by/4.0/>).